Magnetohydrodynamic Phenomena in the Solar Atmosphere

A Thesis
submitted for the degree of
DOCTOR OF PHILOSOPHY

In
The Faculty of Science
Bangalore University

By
DIPANKAR BANERJEE

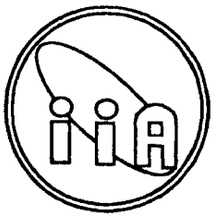

Indian Institute of Astrophysics
Bangalore 560 034, India

December 1996

Declaration

I hereby declare that the work reported in this thesis is entirely original. It was carried out by me in the Indian Institute of Astrophysics, Bangalore, under the supervision of Professor S. S. Hasan. I further declare that it has not formed the basis of any degree, diploma, membership, associateship or similar title of any university or institution.

Prof. S. S. Hasan
(Thesis Supervisor)

Dipankar Banerjee
(Ph. D. Candidate)

Indian Institute of Astrophysics
Bangalore 560 034

December 24, 1996

To my parents

Acknowledgments

During the course of this work I have come across many remarkable people to whom I am indebted in various ways. Due to constraints of space and time it is not possible to mention all of them, but a few prominent ones come readily to the mind. I would like to thank my thesis supervisor, Prof. Siraj Hasan for his guidance and support throughout my association with him. He strongly encouraged me to think independently, and was always willing to share his time and knowledge with me.

I am grateful to Prof. Joergen Christensen-Dalsgaard for his interest, guidance and participation in my work, which proved to be vital through all these years. Our collaboration on magnetoatmospheric waves was both pleasurable as well as instructive experience for me. Discussions with him were instrumental in generating my interest in this field.

At the beginning of my research career I made the acquiantance of Dr. Arnab Rai Choudhuri who has been a continuous source of interesting MHD problems. He is a warmhearted gentleman who guided me through the scientific world, and has been a great host ever since.

During the work on my thesis I had the invaluable chance to travel, and meet many interesting people in the solar physics community. I am grateful to the Director of Indian Institute of Astrophysics, Prof. R. Cowsik, who made this possible by granting me the travel expences. I also thank him for providing all the facilities in the Institute for the benefit of his students. Prof. M. H. Gokhale has also been enormously kind and generous whenever approached.

I wish to express my thanks to all the staff of the Institute. The Library staff and the computer personnel at IIA have also been very helpful. I am indebted to Mr. Prabhakara, Mr. Venkatesh, Mr. Kanakaraj, Mr. Muthukrishnan, Mr. Mohan Kumar, Mr. Nagaraj and Mr. Iyengar for their help whenever I needed.

I would also like to express my gratitude to the Chairman of the Physics Department, Bangalore University, for the cooperation in clearing all administrative formalities.

This work was partially supported by the Danish National Research Foundation, through the establishment of the Theoretical Astrophysics Center. I gratefully acknowledge the financial support rendered by Smithsonian Institution under grant No: 9411FR00007.

All my friends at IIA have made working here an enjoyable experience. I would especially like to thank my 'batchmates', Sujan, Reddy, Uma, Annapurni and Prabhu. The friendship of Dilip, Pandey, Arun, Sivarani, Swara, Sonjoy, Pavan, Rajesh and Srikant was invaluable. I thank all of them for relieving the tedium of work and keeping my enthusiasm alive. I have learnt much from discussions with Jana, Sankar, Krishna and Rajguru.

During the past few years I have come across many friends whose love, affection and company, made my stay at Bangalore memorable. Sujan, Sukanya, Joy, Manjula, Rudra, Pali, Som, Bindu, Jyoti, Ujjwal, Photon, Phutki, Ananya, Anirban, Sumit and Mampu; all of us have had great times together. I would like to reserve special thanks for Sujan, for his critical reading of the draft of this thesis, and providing his own brand of wisdom. The apple of our eyes little Riju, injected freshness and buoyancy in our lives for the past year.

This acknowledgement would remain imperfect if I do not mention all my friends related to the IISc gymkahna and the sporting activities therein. Those who really know me and my love for sports, would appreciate their contributions in keeping my spirits animated through difficult and strained times.

Most of all, I would like to express my gratitude to my parents and in-laws for their encouragement, understanding and support. My brother Subha and brother in-law Kaushik has given me good company over the years. Last but not the least, I thank my best friend and wife, Tisha for getting me this far. Everything would have been otherwise, if not for her.

Preface

The solar atmosphere admits a rich variety of phenomena, which are mainly associated with the interaction of an ionized plasma with a magnetic field. To describe the field structure and its evolution one usually employs the Magnetohydrodynamic (MHD) approximation, which assumes that the plasma can be described by one-fluid theory, and that the spatial and temporal scales of interest are "large". These approximations leads to the usual MHD equations discussed in detail in Alfvén (1950), Cowling (1957) and Priest (1982).

Study of wave motions on the Sun began in the late 1940's. Theorists started to realize that waves could carry energy from the convection zone up to the chromosphere and corona. Dissipation of these waves could then explain the observed increase in temperature of the outer layers of the Sun. Typically, the temperature of the corona is some million degrees, whereas that of the photosphere is only a few thousand degrees. In spite of about half a century of study, it is still not fully understood how the million degree temperature of the corona is maintained against losses due to electron heat conduction, radiation and energy outflow into the solar wind. Propagating waves which are believed to be responsible for this heating are difficult to observe, largely because they are transient and are of small spatial scales. Presence of these waves are inferred from observations of nonthermal broadening of solar spectral lines.

Earliest theories of heating was based on acoustic waves. According to these theories, the sound waves generated in the convection zone travel upwards and form shocks at higher atmosphere (due to increase of amplitudes) and dissipate their energy in these layers. However, after the Skylab observations of the early 1970's, it became apparent that the upper chromosphere and corona do not derive their high temperature from acoustic waves. So pure acoustic wave theories are inadequate for explaining coronal

heating. Modern theories involve magnetic fields in some way or the other.

It is now generally accepted on the basis of observations (Stenflo, 1989) that the solar magnetic field is highly structured, with most of the magnetic flux in the photosphere being clumped into small intense flux tubes, with diameters of the order 200 - 300 km. The high resolution imaging observations (Berger and Title, 1996) suggest that the strong component of the magnetic field outside sunspots and pores is concentrated in isolated flux tubes of about 200 km in diameter with kilogauss field strength. Diameters of tubes, corresponding to a sunspot is of the order of several thousand kilometers. There are also tubes with intermediate sizes, such as pores and faculae. There is further evidence of weak field component at the center of supergranular cells (Zirin, 1987). Estimate of the strength of this field component vary from 100-500 G (Keller *et al.* 1994). Thus the waves carrying energy from the photosphere to the corona can be modelled as waves propagating along magnetic flux tubes.

Unfortunately, the construction of an equilibrium solution for a stratified flux tube is extremely complicated, let alone the question of wave propagation. Most of the analyses of waves in flux tubes have either neglected the gravity or used the thin flux tube approximation (Defouw 1976, see reviews by Thomas 1990, Hollweg 1990 for further references). The neglect of stratification is inappropriate for photospheric flux tubes. On the other hand, the thin flux tube approximation is more reasonable for treating wave propagation in intense flux tubes, where the tube radius is typically smaller than the pressure scale height in the vertical direction. If thin flux tube equations are used to study the wave propagation along flux tubes, then one obtains two kinds of solutions corresponding to the "sausage" and "kink" modes.

The present thesis is roughly divided into two parts. Part I (Chapter 1) treats the problem of energy transport to the solar corona by magnetic kink waves in the thin flux tube approximation and part II (Chapters 2, 3 and 4) pertains to homogeneous fields and not to flux tubes. In this part of the investigation we assume that the flux tubes in question are sufficiently thick, so that the field can be regarded to have infinite horizontal extent.

In the past twenty five years, observations of oscillations with fairly broad range of frequencies have been reported in magnetic elements of solar atmosphere (Bhatnagar *et*

al. 1972, Lites and Thomas 1984, 1985, Giovanelli 1975, Moore and Rabin 1985, Lites 1992). The umbral oscillations with periods in the 2-3 min band and the penumbral waves are perhaps the best reported oscillations in flux tubes on the Sun. In addition, oscillations have also been observed in intense flux tubes, though not as extensively as in sunspots, because intense tubes are hard to resolve from ground-based instruments. Thus, waves provide a powerful diagnostic for probing physical conditions within flux tubes, particularly in deeper layers, normally inaccessible to observations. In part II of this thesis we shall examine some of the properties of such oscillations.

Outline of the thesis

In *Chapter* 1 we show that the magnetic kink waves generated by the motions of photospheric footpoints of the coronal flux tubes can supply adequate energy for heating the quiet corona. We model the solar corona as a two layer isothermal atmosphere, with the lower layer having chromospheric thickness and temperature, and the upper layer having coronal temperature. Even in the presence of such a temperature jump, we find that the rapid footpoint motions (observed by Muller *et al.* 1994) are efficient enough to carry enough energy to the corona and the estimated energy flux is sufficient for quiet coronal heating. In addition to presenting results for the solar corona, we discuss the general problem of the propagation of kink pulses in two-layer atmosphere for different possible values of the basic parameters. We find a fairly complicated behavior which could not be anticipated from the analysis of a pure Fourier mode. For pulses generated by rapid footpoint motions, the energy flux decreases due to reflection at the transition layer. For pulses generated by slow footpoint motions, however, the behavior of the system is governed by modes, which are evanescent in the lower layer, but can tunnel through it. The energy flux carried by such pulses can actually increase when there is a temperature jump in the atmosphere.

In *Chapter* 2 we develop a theory for magnetoatmospheric oscillations. Qualitatively, the waves that we are dealing with are called magneto-acoustic-gravity (MAG for short), denoting the three distinct forces that are present, *viz.*, magnetic, pressure and gravity. Without gravity, the theoretical analysis is straightforward. However when stratification due to gravity is taken into account, the mathematical analysis becomes

more complicated. Therefore, what is required is a theory of wave propagation in a stratified atmosphere with a vertical magnetic field. The theoretical understanding of the nature of wave modes in such a medium is currently far from complete. In this investigation, we attempt to analyze the physical nature of MAG oscillations, by examining how the normal modes of an unmagnetized stratified atmosphere are modified by the introduction of a small vertical magnetic field. We employ a set of boundary conditions, which may not be directly applicable to a realistic solar situation; nevertheless, the results provide some insight into the general properties of oscillations in a stratified atmosphere with a vertical magnetic field. The general solutions of the wave equation for an isothermal magnetized medium are first given. We present asymptotic expansions of these solutions in the weak-field limit. An analytical expression for the dispersion relation is derived, which allows the effect of a weak magnetic field on the modes to be studied. We explicitly demonstrate how the choice of boundary conditions affect the various elementary wave modes present in the atmosphere.

Detailed results are presented in the form of diagnostic diagrams, showing the variation of frequency with horizontal wave number. The solutions clearly reveal the presence of *avoided crossings*, which occur at the otherwise degenerate frequencies. Our results, though somewhat idealized, find application in the analysis of waves in sunspots.

Oscillations in a realistic stellar atmosphere are affected by radiative dissipation and energy loss at the boundaries. Thus the modes are damped, with complex frequencies. In *Chapter* 3 we concentrate on the behavior of the modes near the avoided crossings in the the $k-\omega$ diagram for zero-gradient boundary conditions. We find that in such regions the frequencies of the modes become complex, whereas away from the avoided crossings the frequencies are real (in the adiabatic case) for these boundary conditions. The effects on the topology of the $K-\Omega_r$ diagram (Ω_r being the real part of the frequency) in the vicinity of an avoided crossing depend on the relative magnitude of the damping rates of the two modes involved and the minimum separation in the (undamped) avoided crossing. If the minimum separation exceeds the difference in damping rates between the modes, Ω_r undergoes an avoided crossing, while the damping rates cross. Our results clearly demonstrate that for certain boundary conditions, the frequencies can become complex in an adiabatic system, where no explicit energy

loss mechanism is taken into account. It appears that the boundary conditions permit the phase relationship between the modes to be changed in a manner so as to allow the wave to leak out from the boundary, thereby leading to a loss of energy from the cavity. This behavior occurs only when there is a strong mode coupling for certain combination of frequencies and wave numbers. We study the behavior of the eigenfunctions near the avoided crossing regions, calculate the net upward energy flux going out of this cavity and examine the height variation of various components of the energy density.

In *Chapter* 4 we examine non-adiabatic effects on the modes of an isothermal stratified magnetic atmosphere. The innlusion of radiative dissipation in magnetoatmospheric wave problems is often necessary, since thermal cooling effects can be important. As a first step, we modify the adiabatic treatment by allowing for radiative losses approximated by Newton's law of cooling. Using this cooling law, an analytic expression for the dispersion relation is derived in the weak field case, which allows us to study the effect of the magnetic field on the modes. We show how the effects of radiative damping can be incorporated in magnetoatmospheric problems be letting the ratio of specific heats, γ, become a complex frequency dependent quantity. We examine the nature of the eigenfrequency curves in the diagnostic diagram and find that, similar to the previous analysis, the modes undergo avoided crossings. We find that radiative heat exchange leads to a damping of the modes. This damping is particularly effective at the avoided crossings. Thus strong mode coupling in the avoided crossing regions permits energy leakage. We address the implication of our results to waves in solar flux-tubes.

Finally, in *Chapter* 5 the results of the investigation described in the thesis are summarized with specific conclusions. A brief discussion on the further scope on this study is also presented.

Contents

Chapter 1

Energy Transport by Magnetic Kink Waves

1.1 Introduction

Two mechanisms have been suggested for heating the solar corona - direct dissipation of magnetic topologies and dissipation of waves (Parker 1986; Hollweg 1990a; Ulmschneider *et al.* 1991; Narain and Ulmschneider 1991,1996). Though it is conceivable that both these mechanisms are operative in the closed active region loops, the heating of the quiet corona with open magnetic field lines can only be due to the dissipation of hydromagnetic waves which are produced by photospheric disturbances and then propagate along magnetic field lines. The magnetic flux at the photospheric level exists as isolated flux tubes, which fan out upwards and eventually merge with each other above the chromosphere. Hence the waves carrying energy from the photosphere to the corona can be modelled, at least in the layers just above the photosphere, as waves propagating along magnetic flux tubes. Until recently there was no direct observational evidence as to the nature of the footpoint motions. Since footpoints are presumably shuffled by the granular convection, theorists working on the coronal heating problem assumed that the typical length, time and velocity scales for the footpoint motions are comparable to those for the granules. Although supergranular scales can also be of some importance in the topological dissipation models, they are unlikely to be of any relevance for the wave heating theories. A question of crucial importance is: what is the nature of these waves? If thin flux tube equations are used to study the wave propagation along flux tubes, then one obtains two kinds of solutions correspond-

ing to the sausage and kink modes (Spruit 1981; Roberts 1985). Each mode has its own characteristic cutoff period and propagates upward only if its period is below the cutoff period. For the solar atmosphere just above the photosphere, the cutoff periods for the sausage and kink modes are, respectively estimated to be about 200 s and 700 s. For photospheric disturbances with the typical granular time scales (about 500 s), the sausage mode would not propagate, whereas the kink mode barely propagates. When the footpoints moves rapidly for a short time, we find that much of the energy is fed into the kink mode at frequencies well above the cutoff frequency and hence can propagate upward. Though there exists some studies of the propagation of sausage modes along flux tubes in the solar atmosphere (Rae and Roberts 1982; Hollweg 1982), to the best of our knowledge detailed studies of the propagation of kink modes have not been carried out earlier.

By using the full MHD equations, one can show the existence of a third kind of mode - the shear Alfvén mode (also called torsional Alfvén mode) - which cannot be handled by thin flux tube equations (Hollweg 1990a). Most probably the movements of flux tube footpoints give rise to a mixture of all these modes (see discussion and figures in §2 of Hollweg [1981]).

Some recent observations suggest that the flux tube footpoints occasionally undergo rapid motions for short durations (Muller *et al.* 1994). The theoretical implications of these rapid intermittent motions have been studied by Choudhuri, Auffret and Priest (1993; hereafter CAP). The bright points seen in high-resolution photographs of the photosphere are usually identified as intense flux tubes which are presumably the footpoints of the magnetic fields that thread the corona (Muller *et al.* 1994). Berger and Title (1996) has reported the dynamics of the small scale solar magnetic field, based on high resolution images of the solar photosphere obtained at the Swedish vacuum tower telescope. The bright points move in the intergranular lanes and are primarily driven by the evolution of the local granular convection flow field. It has also been observed at Pic-du-midi (Muller *et al.* 1994.) that these bright points occasionally undergo rapid motions with velocities of the order of 3 km/s typically lasting for 3 minutes. It was pointed out by CAP that such jerky motions of footpoints would give rise to kink modes in the flux tubes above, and the properties of these kink modes were studied by con-

sidering an isothermal atmosphere of photospheric temperature above the photosphere. It was found that these occasional jerky motions were much more efficient for sending energy to the corona compared to the slow Brownian motions of footpoints that must be taking place most of the time. A calculation of the energy flux using the isothermal atmosphere model incorporating these rapid footpoint motions suggested a value of energy flux well above what is needed for heating the quiet corona. In the actual solar atmosphere, however, one may expect the flux to be reduced due to reflections from the transition layer where the temperature jumps sharply from chromospheric to coronal values. The aim of the present study is to extend the calculations of CAP for a two-layer atmosphere, which illustrates how the energy transport to the corona is influenced by the temperature jump in the transition layer.

The reflection of the shear Alfvén mode (*i.e.*, torsional Alfvén mode) at the transition layer has been studied by several authors (Hollweg 1981, 1984; Zhugzhda and Locans 1982). One may at first expect that the reflection of kink modes will be of very similar nature. A qualitative difference between the two situations, however, arises from the fact that the kink modes propagating along flux tubes in a gravitationally stratified atmosphere have a cutoff frequency below which they do not propagate, whereas there is no such lower cutoff for the shear Alfvén mode. Most wave modes in gravitationally stratified atmospheres - starting from the simplest acoustic mode (Lamb 1932) - have cutoff frequencies. The shear Alfvén mode is one very special mode which does not couple to gravity, at least in the linear theory with purely horizontal displacements, and hence does not have a cutoff frequency. We show that the reflections of kink modes with frequencies close to the gravitational cutoff frequency is a much more subtle and richer phenomena than reflections of the shear Alfvén mode without a cutoff.

1.1.1 Two-layer atmosphere

Let us consider a vertical thin flux tube embedded in a two-layer atmosphere, the lower layer of height h at a temperature T_1 and the upper one at temperature T_2, with $T_2 > T_1$. Such a two-layer model is quite appropriate for the solar atmosphere (see Fontenla, Avrett and Loeser 1990) and has been used by many authors. The cutoff frequency ω_{c_2} of hot upper layer will be less than that of the lower layer (*i.e.*,

$\omega_{c_2} < \omega_{c_1}$). For frequencies larger than ω_{c_1}, the modes will propagate in both the layers. On the other hand, modes with frequencies less than ω_{c_2} will be evanescent in both the layers. But for the intermediate frequencies between ω_{c_2} and ω_{c_1}, the modes will be evanescent in the lower layer and propagating in the upper layer. If the lower layer extended over many scale heights, then these intermediate modes would not be able to take away any energy flux. On the other hand, if the lower layer were sufficiently thin, then these modes could "tunnel" through it and then propagate in the upper layer. Hence, under certain circumstances, the asymptotic energy flux, instead of becoming less than what it would have been in an isothermal atmosphere with temperature T_1, actually becomes more if there is a temperature jump from T_1 to T_2 with a hotter layer above! Something like this is never possible for a mode like the shear Alfvén mode without a cutoff, for which, if there is a jump to higher temperature in the overlying atmosphere, the flux is always reduced due to reflection compared to the flux in the isothermal atmosphere. Most previous studies of this mode involved the study of a particular Fourier component, and this was sufficient to understand the behavior of the mode. However, for kink modes behaving very differently in different frequency ranges, it is not sufficient to look at individual Fourier components in order to understand the basic physics. Hence we study the propagation in this two-layer atmosphere of kink pulses having wide ranges of frequencies in their spectral resolution.

A previous study of kink propagation along flux tubes in the solar atmosphere was reported by Spruit (1984), where he incorporated the merging of flux tubes above a certain height. Since our analytical expressions for pulse propagation become quite formidable even without the merger of flux tubes, we have not incorporated it in this study, though we wish to look at the effects of merger in future. The emphasis in this study has been to understand the basic physics of pulse propagation along isolated flux tubes in the presence of a temperature jump without putting other additional complications.

Much of the Chapter is devoted to studying the basic physics of the problem. We present a fairly exhaustive parameter space study to illustrate the nature of kink wave propagation in a two-layer atmosphere for different possible combinations of the basic parameters. Finally at the end, we apply our general results to the solar atmosphere. We

reinforce the main conclusion of CAP that the rapid footpoint motions are much more efficient for transporting energy to the corona. Even in the presence of the temperature jump at the transition layer, the rapid footpoint motions are able to transmit sufficient energy to heat the quiet corona, though the energy flux is somewhat reduced due to reflection from the transition layer. For the slow footpoint motions, on the other hand, the energy flux may increase slightly due to the "tunnelling" effect described above.

The basic magnetohydrodynamic equations for a thin flux tube is presented in §1.2. The next Section studies the nature of a Fourier component of the kink mode in a two-layer atmosphere. Subsequently § 1.4 discusses how the Fourier modes can be superposed to provide a kink pulse. The parameter space study is presented in § 1.5. We apply our results to the solar atmosphere in § 1.6. Finally the last Section summarizes our conclusions.

1.2 MHD Equations for a thin tube

1.2.1 Equation of motion

Throughout this Chapter we will assume that viscosity and resistive diffusion are negligible. The equation of motion for a fluid with an arbitrary field configuration is given by

$$\rho\frac{\mathrm{d}\mathbf{v}}{\mathrm{d}t} = -\nabla(p+\frac{B^2}{8\pi}) + \frac{1}{4\pi}(\mathbf{B}\cdot\nabla)\mathbf{B} + \rho\mathbf{g} \ , \tag{1.1}$$

where ρ is the density, p is the pressure, $\mathbf{B}$ is the magnetic field and $\mathbf{g}$ is the acceleration due to gravity. We want to apply this to the case of an isolated flux tube. The tube is assumed to be thin compared to the scale height H $(= p/\rho g)$ of the atmosphere. The cross section of the tube could in principle have any arbitrary shape, but we neglect the details of the shape here and assume that it is circular at all times. Secondly, we assume that the tube is *untwisted*. This is an essential simplification which ignores process like kink instability or the propagation of twist along the tube by shear Alfvén wave.

1.2.2 Continuity and Induction

For a fluid with zero resistivity the equation of continuity and induction can be combined into one equation (Roberts 1985)

$$\frac{\mathrm{d}}{\mathrm{d}t}\frac{\mathbf{B}}{\rho} = (\frac{\mathbf{B}}{\rho}\cdot\nabla)\mathbf{v}\,. \tag{1.2}$$

This equation expresses the conservation of mass, in terms of the mass per unit length of the tube (ρ/B).

1.2.3 Transverse oscillations of a vertical tube

Now we consider a vertical flux tube, initially at rest in a hydrostatically stratified atmosphere. Suppose the tube is shaken sideways, for example by convective motions with a frequency ω at some point in the atmosphere. For a flux tube which is in temperature equilibrium with its surroundings, the equation for propagation of transversal oscillations of a vertical flux tube is given by (Spruit 1981)

$$(2\beta+1)\partial_{tt}\xi = g\partial_z\xi + \beta v_A^2\partial_{zz}\xi. \tag{1.3}$$

For an isothermal atmosphere H is constant. The solutions of equation (1.3) are of the form

$$\xi = \exp(\mathrm{i}\omega t + \mathrm{i}kz + \frac{z}{4H}) \tag{1.4}$$

such that

$$k = \pm\frac{1}{4H}(\frac{\omega^2}{\omega_c^2}-1)^{1/2}\quad , \tag{1.5}$$

where ω_c is the cutoff frequency given by

$$\omega_c^2 = \frac{g}{8H}\frac{1}{2\beta+1}\quad . \tag{1.6}$$

For ω less that the cutoff frequency ω_c, the solution is evanescent, and for $\omega > \omega_c$, the solution is an up or downward propagating wave whose amplitude increases exponentially with height (*cf.* Eq. [1.4]). Formally, the solution is completely analogous to that for a vertically propagating acoustic wave in an isothermal atmosphere. For the acoustic wave the factors 1/4 in equations (1.4) and (1.5) are replaced by 1/2, and ω_c by the acoustic cutoff frequency $\omega_a = c/2H$. In the case of sound waves, it is observed (in the

5 min oscillations) that almost all power lies just below the acoustic cutoff frequency, *i.e.*they do not propagate into the chromosphere. Hence, sound waves are not believed to cause chromospheric or coronal heating any more.

1.3 The nature of a Fourier mode

We consider the propagation of a kink mode of frequency ω along a vertical flux tube in a two-layer atmosphere. The lower layer with temperature T_1 is taken to extend from $z = 0$ to $z = h$, and the upper layer with temperature T_2 starts from $z = h$. The pressure scale heights in the two layers are proportional to the temperatures We list the two assumptions used throughout this Chapter.

- The flux tube along which the kink propagates is considered isolated, *i.e.*, we do not take into account the merging of neighboring flux tubes above the photospheric level.
- We neglect nonlinear effects so that any kink disturbance can be represented by a linear superposition of individual Fourier modes.

The kink mode coming from below reaches the interface $z = h$, where a part of the wave gets reflected downwards into the first layer and the rest transmits into the second layer. Using the solution for a kink mode in an isothermal atmosphere (Eqs. [1.4]-[1.6]) we write the velocity in the first layer as the linear combination of an upward propagating wave and a downward propagating reflected wave, whereas the velocity in the second layer consists of only the upward propagating transmitted wave:

$$v_1(z,t) = [\hat{v}_u(\omega)\exp\{i\omega t - ik_1(\omega)z\} + \hat{v}_d(\omega)\exp\{i\omega t + ik_1(\omega)z\}]\exp(z/4H_1) \quad , \quad (1.7)$$

$$v_2(z,t) = \hat{v}_t(\omega)\exp\{i\omega t - ik_2(\omega)z\}\exp(z/4H_2) \quad , \quad (1.8)$$

where $\hat{v}_u(\omega)$, $\hat{v}_d(\omega)$, $\hat{v}_t(\omega)$ represent the amplitudes of the original wave, reflected wave and transmitted wave respectively, whereas H_1 and H_2 are the pressure scale heights. The wavenumbers $k_1(\omega)$ and $k_2(\omega)$ are related to ω as follows (see Eq.[1.5])

$$k_1(\omega) = \pm\frac{1}{4H_1}\left(\frac{\omega^2}{\omega_{c_1}^2} - 1\right)^{1/2} \quad , \quad (1.9)$$

$$k_2(\omega) = \pm\frac{1}{4H_2}(\frac{\omega^2}{\omega_{c_2}^2} - 1)^{1/2} \quad , \tag{1.10}$$

where ω_{c_1} and ω_{c_2}, the cutoff frequencies of the first and second layers, are given by

$$\omega_{c_1}^2 = \frac{g}{8H_1}\frac{1}{2\beta+1} \quad , \tag{1.11}$$

and

$$\omega_{c_2}^2 = \frac{g}{8H_2}\frac{1}{2\beta+1} \tag{1.12}$$

If we assume the flux tubes to be in thermal equilibrium with the surroundings, it can be easily shown that $\beta = 8\pi p/B^2$ has to be a constant inside a particular layer. The continuity of pressure and magnetic field across the interface further ensures that β is continuous across the interface, *i.e.*, it is constant everywhere. We now relate $\hat{v}_u(\omega)$, $\hat{v}_d(\omega)$ and $\hat{v}_t(\omega)$ by using the boundary conditions to be satisfied across the interface $z = h$. Firstly, the displacements on the two sides have to be matched. From equations (1.7) and (1.8) the corresponding displacements in the two layers can be written as

$$\xi_1(z,t) = \frac{1}{\mathrm{i}\omega}[\hat{v}_u(\omega)\exp\{\mathrm{i}\omega t - \mathrm{i}k_1(\omega)z\} + \hat{v}_d(\omega)\exp\{\mathrm{i}\omega t + \mathrm{i}k_1(\omega)z\}]\exp(z/4H_1), \tag{1.13}$$

$$\xi_2(z,t) = \frac{1}{\mathrm{i}\omega}[\hat{v}_t(\omega)exp\{\mathrm{i}\omega t - \mathrm{i}k_2(\omega)z\}]\exp(z/4H_2). \tag{1.14}$$

By matching these expressions of displacements at the interface at $z = h$, we have

$$\hat{v}_u(\omega)\exp\{\mathrm{i}k_1(\omega)h + \frac{h}{4H_1}\} + \hat{v}_d(\omega)\exp\{\mathrm{i}k_1(\omega)h + \frac{h}{4H_1}\} =$$
$$\hat{v}_t(\omega)\exp\{-\mathrm{i}k_2(\omega)h + \frac{h}{4H_2}\}. \tag{1.15}$$

The second boundary condition can be obtained from the basic equation of kink mode propagation (Eq. [1.3]). By integrating this equation from $z = h - \epsilon$ to $z = h + \epsilon$ (ϵ being a very small quantity), it is easily seen that

$$\partial_z\xi\,|_{h-\epsilon} = \partial_z\xi|_{h+\epsilon}\,, \tag{1.16}$$

i.e.$\partial_z\xi$ is continuous across $z = h$.

Applying equation (1.16), we have

$$\left[-\mathrm{i}k_1(\omega) + \frac{1}{4H_1}\right]\hat{v}_u(\omega)\exp\left[-\mathrm{i}k_1(\omega)h + \frac{h}{4H_1}\right] + \left[\mathrm{i}k_1(\omega) + \frac{1}{4H_1}\right]\hat{v}_d(\omega)$$
$$\exp\left[\mathrm{i}k_1(\omega)h + \frac{h}{4H_1}\right] = \left[-\mathrm{i}k_2(\omega) + \frac{1}{4H_2}\right]\hat{v}_t(\omega)\exp\left[-\mathrm{i}k_2(\omega)h + \frac{h}{4H_2}\right] \tag{1.17}$$

From equations (1.15) and (1.17),

$$\hat{v}_d(\omega) = \frac{[\mathrm{i}\{k_1(\omega) - k_2(\omega)\} - (\frac{1}{4H_1} - \frac{1}{4H_2})]\exp\{-2\mathrm{i}k_1(\omega)h\}}{[\mathrm{i}\{k_1(\omega) + k_2(\omega)\} + (\frac{1}{4H_1} - \frac{1}{4H_2})]}\hat{v}_u(\omega), \tag{1.18}$$

$$\hat{v}_t(\omega) = \frac{2\mathrm{i}k_1(\omega)\exp\{-\mathrm{i}(k_1(\omega) - k_2(\omega))h + h(\frac{1}{4H_1} - \frac{1}{4H_2})\}}{[\mathrm{i}\{k_1(\omega) + k_2(\omega)\} + (\frac{1}{4H_1} - \frac{1}{4H_2})]}\hat{v}_u(\omega). \tag{1.19}$$

Thus the amplitudes of reflected and transmitted waves are expressed in terms of the incident upward wave so that the amplitude of the incident wave, which is a measure of the overall amplitude, remains the only free parameter.

In order to study the transmission of energy towards the corona in this two-layer model, we define the transmission coefficient $\mathcal{T}$ as the ratio of the energy density due to the transmitted wave at the bottom of the second layer to the energy density due to the original wave at the footpoint:

$$\mathcal{T} = \frac{\rho_2(h)A_2(h)v_2^2(h)}{\rho_{1,0}A_{1,0}v_u^2(0)} \quad , \tag{1.20}$$

ρ's and A's being the densities and cross-sectional areas of the flux tube in the two layers given by

$$\rho_1(z) = \rho_{1,0}\exp(-z/H_1) \quad , \tag{1.21}$$

$$\rho_2(z) = \rho_{2,0}\exp(-z/H_2) \quad , \tag{1.22}$$

$$A_1(z) = A_{1,0}\exp(z/2H_1) \quad , \tag{1.23}$$

$$A_2(z) = A_{2,0}\exp(z/2H_2) \quad , \tag{1.24}$$

and v_u is the part of v_1 as given in equation (1.7) which corresponds to the upward wave. The quantities $\rho_{1,0}$, $\rho_{2,0}$, $A_{1,0}$, $A_{2,0}$ are related to one another in the following manner: Since the pressure is continuous across $z = h$,

$$\rho_1(h)T_1 = \rho_2(h)T_2 \quad , \tag{1.25}$$

or

$$\rho_{2,0} = \frac{T_1}{T_2}\rho_{1,0}\exp(-\frac{h}{H_1} + \frac{h}{H_2}). \tag{1.26}$$

Again, since the flux tube must be continuous at $z = h$,

$$A_1(h) = A_2(h), \tag{1.27}$$

or

$$A_{2,0} = A_{1,0} \exp(\frac{h}{2H_1} - \frac{h}{2H_2}). \tag{1.28}$$

Using equations (1.7) - (1.8), (1.19) - (1.24), (1.26) and (1.28), we can rewrite the expression (1.20) as

$$\mathcal{T} = \frac{T_1}{T_2} \left| \frac{2ik_1(\omega) \exp(-ik_1(\omega)h)}{i\{k_1(\omega) + k_2(\omega)\} + (\frac{1}{4H_1} - \frac{1}{4H_2})} \right|^2. \tag{1.29}$$

It is to be noted that we are defining the transmission coefficient $\mathcal{T}$ as a ratio of energy densities, whereas the more usual practice is to define it as a ratio of energy fluxes. Our motivation behind using densities rather than fluxes is to develop a uniform approach which would be applicable even in the cases where the wave in the lower layer is evanescent and there is no flux in that layer. We can express $\mathcal{T}$ as a function of frequencies by using the dispersion relations for the two layers given in equations (1.9) and (1.10). From equations (1.11) and (1.12) it can easily be seen that the cutoff frequency ω_{c_1} of the first layer is higher than the cutoff frequency ω_{c_2} of the hotter second layer and

$$\omega_{c_2}/\omega_{c_1} = \sqrt{T_1/T_2}. \tag{1.30}$$

Choosing the signs of $k_1(\omega)$ and $k_2(\omega)$ in such a way that the propagating waves propagate upwards and the evanescent waves die away with height, we have the following five combinations of $k_1(\omega)$ and $k_2(\omega)$ for different ranges of ω.

$$\text{For} -\infty < \omega < -\omega_{c_1}, \begin{cases} k_1(\omega) &= -\frac{1}{4H_1}(\frac{\omega^2}{\omega_{c_1}^2} - 1)^{1/2}, \\ k_2(\omega) &= -\frac{1}{4H_2}(\frac{\omega^2}{\omega_{c_2}^2} - 1)^{1/2}, \end{cases} \tag{1.31}$$

$$\text{for} -\omega_{c_1} < \omega < -\omega_{c_2}, \begin{cases} k_1(\omega) &= -\frac{i}{4H_1}(1 - \frac{\omega^2}{\omega_{c_1}^2})^{1/2}, \\ k_2(\omega) &= -\frac{1}{4H_2}(\frac{\omega^2}{\omega_{c_2}^2} - 1)^{1/2}, \end{cases} \tag{1.32}$$

$$\text{for} -\omega_{c_2} < \omega < \omega_{c_2}, \begin{cases} k_1(\omega) &= -\frac{i}{4H_1}(1 - \frac{\omega^2}{\omega_{c_1}^2})^{1/2}, \\ k_2(\omega) &= -\frac{i}{4H_2}(1 - \frac{\omega^2}{\omega_{c_2}^2})^{1/2}, \end{cases} \tag{1.33}$$

$$\text{for } \omega_{c_2} < \omega < \omega_{c_1}, \begin{cases} k_1(\omega) &= -\frac{i}{4H_1}(1 - \frac{\omega^2}{\omega_{c_1}^2})^{1/2}, \\ k_2(\omega) &= -\frac{1}{4H_2}(\frac{\omega^2}{\omega_{c_2}^2} - 1)^{1/2}, \end{cases} \tag{1.34}$$

$$\text{for } \omega_{c_1} < \omega < \infty, \begin{cases} k_1(\omega) &= \frac{1}{4H_1}(\frac{\omega^2}{\omega_{c_1}^2} - 1)^{1/2}, \\ k_2(\omega) &= \frac{1}{4H_2}(\frac{\omega^2}{\omega_{c_2}^2} - 1)^{1/2}. \end{cases} \tag{1.35}$$

The transmission coefficient $\mathcal{T}$ for any frequency can now be found out by substituting the appropriate combination for $k_1(\omega)$ and $k_2(\omega)$ in equation (1.29).

At this point, it is useful to introduce a set of dimensionless variables, some of which have already been introduced in CAP. Here we shall make the variables dimensionless with respect to the constants of the first layer.

$$u = \frac{\omega}{\omega_{c_1}}, \tag{1.36}$$

$$\tau = \omega_{c_1} t, \tag{1.37}$$

$$s = \frac{z}{4H_1}, \tag{1.38}$$

$$\alpha = \frac{h}{4H_1}, \tag{1.39}$$

$$r^2 = \frac{T_1}{T_2}, \tag{1.40}$$

so that

$$\omega_{c_2}/\omega_{c_1} = r. \tag{1.41}$$

Here u, τ and s are dimensionless frequency, time and height respectively. The other two variables α and r are the two basic parameters for the two-layer atmosphere. They are respectively the measures of the thickness of the lower layer and the temperature contrast between the two layers.

It is easy to see from equation (1.29) that $\mathcal{T}$ is symmetric in positive and negative frequencies. Hence we write down the expressions of $\mathcal{T}$ for different ranges of positive frequencies only. Choosing the proper expressions from equations (1.31) to (1.35), for $u < r$, *i.e.*, when the waves are evanescent in both the layers, we have

$$\mathcal{T} = \frac{4r^2(1-u^2)\exp(-2\alpha\sqrt{1-u^2})}{\{\sqrt{1-u^2} + r\sqrt{r^2-u^2} + (1-r^2)\}^2}. \tag{1.42}$$

For $r < u < 1$, *i.e.*, when the waves are evanescent in the first layer but propagating in the second layer,

$$\mathcal{T} = \frac{4r^2(1-u^2)\exp(-2\alpha\sqrt{1-u^2})}{r^2(u^2-r^2) + \{\sqrt{1-u^2} + (1-r^2)\}^2}. \tag{1.43}$$

For $u > 1$, *i.e.*, when the waves are propagating in both the layers,

$$\mathcal{T} = \frac{4r^2(u^2-1)}{\{\sqrt{u^2-1}+r\sqrt{u^2-r^2}\}^2+(r^2-1)^2}. \tag{1.44}$$

By varying the values of r and α, we can study how the transmission of energy changes when the temperature ratio of the two layers is changed or the height of the interface is altered. In Figure 1.1, $\mathcal{T}$ has been plotted against frequency u. Figure 1.1*a* shows

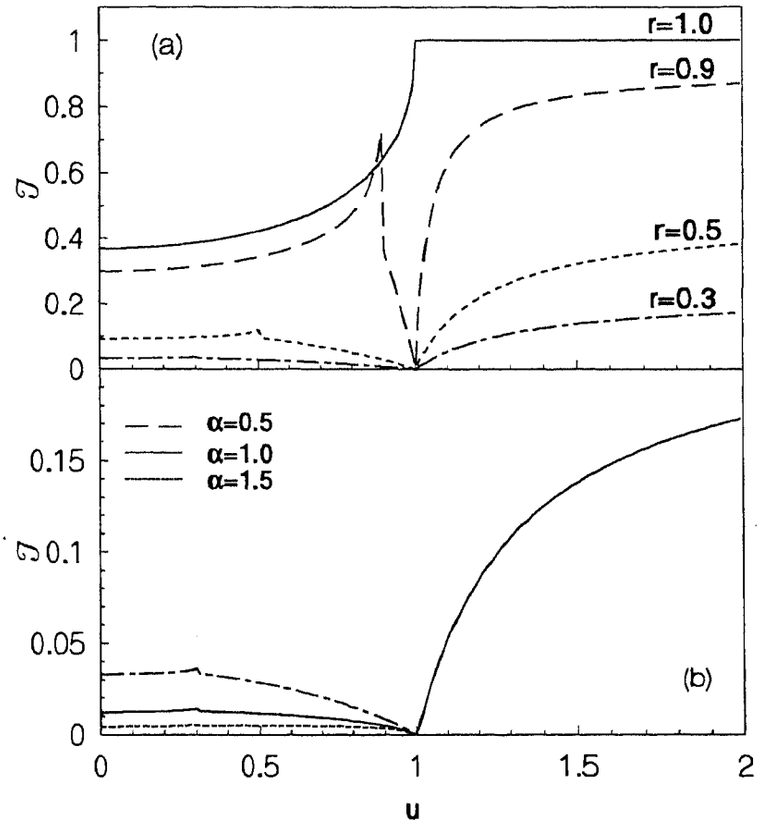

Figure 1.1: Transmission coefficient $\mathcal{T}$ as a function of frequency ($u = \omega/\omega_{c_1}$) for (*a*) different temperature contrasts r and a fixed thickness $\alpha = 0.5$ of the first layer, (*b*) for different α (thickness of the first layer) and a particular temperature contrast $r = 0.3$.

the transmission for different values of r, smaller r corresponding to larger temperature contrast between the layers. For $u > 1$, the mode is propagating in both the layers and we expect the transmission of energy to decrease as the temperature jump increases to produce larger reflection. We see in Figure 1.1 that $\mathcal{T}$ is reduced for smaller r not only

when $u > 1$ but also when $u < 1$. If we have the frequency in the range $r > u > 1$, then the mode can propagate in the upper layer after tunnelling through the lower. With larger temperature jump (*i.e.*, smaller r), the range of tunnelling becomes larger. Hence, though the value of $\mathcal{T}$ is smaller for smaller r, the overall energy transport may enhance with smaller r because of this increase in the range of tunnelling. We shall show in the next Section that the transmission of a low-frequency pulse can become more efficient in a two-layer atmosphere if the upper layer is made hotter, thereby making r smaller and increasing the range of tunnelling. Figure 1.1*b* shows how $\mathcal{T}$ changes on changing α for a particular r. When the mode is propagating in both the layers (*i.e.*, $u > 1$), $\mathcal{T}$ is independent of α as can be seen in equation (1.44). Only when the mode is evanescent in the lower layer, $\mathcal{T}$ decreases with increasing α (which is a measure of the thickness of the lower layer).

1.4 Pulse propagation.

After considering a Fourier component of the kink mode in the last Section, we now study the propagation of a pulse along the flux tube which can be represented as a superposition of the Fourier components. We consider a pulse generated by a footpoint motion having a Gaussian profile of velocity as a function of time:

$$v_x(z=0,t) = v_0 \mathrm{e}^{-bt^2} \tag{1.45}$$

The total displacement due to this motion is finite and is given by

$$L = \sqrt{\frac{\pi}{b}} v_0 \tag{1.46}$$

Though the velocity is mathematically non-zero at all times, it is appreciable only from time $-1/\sqrt{b}$ to time $+1/\sqrt{b}$. Hence a finite motion of the footpoint in finite time can roughly be modelled with such a Gaussian profile. The advantage of taking a Gaussian velocity profile is that the calculations can be carried out analytically. To find the response of the flux tube to such a motion, we superpose the Fourier modes as given in equations (1.7) and (1.8) *i.e.*,

$$v_1(z,t) = \int_{-\infty}^{+\infty} [\hat{v}_u(\omega) \exp(\mathrm{i}\omega t - \mathrm{i}k_1(\omega)z) + \hat{v}_d(\omega) \exp\{\mathrm{i}\omega t + \mathrm{i}k_1(\omega)z\}] \exp(\frac{z}{4H_1}) d\omega, \tag{1.47}$$

$$v_2(z,t) = \int_{-\infty}^{+\infty} \hat{v}_t(\omega) \exp(\mathrm{i}\omega t - \mathrm{i}k_2(\omega)z) \exp(\frac{z}{4H_2}) d\omega. \tag{1.48}$$

The corresponding displacements of the flux tubes in the two layers are

$$\xi_1(z,t) = \int_{-\infty}^{+\infty} \frac{d\omega}{\mathrm{i}\omega} \left[\hat{v}_u(\omega) \exp\{\mathrm{i}\omega t - \mathrm{i}k_1(\omega)z\} + \hat{v}_d(\omega) \exp\{\mathrm{i}\omega t + \mathrm{i}k_1(\omega)z\}\right] \exp(\frac{z}{4H_1}), \tag{1.49}$$

$$\xi_2(z,t) = \int_{-\infty}^{+\infty} \frac{d\omega}{\mathrm{i}\omega} \left[\hat{v}_t(\omega) \exp\{\mathrm{i}\omega t - \mathrm{i}k_2(\omega)z+\}\right] \exp(\frac{z}{4H_2}). \tag{1.50}$$

Since we have already related $\hat{v}_d(\omega)$ and $\hat{v}_t(\omega)$ to $\hat{v}_u(\omega)$ in equations (1.18) and (1.19), we just have to find out $\hat{v}_u(\omega)$ from the footpoint motion equation (1.45). Using equations (1.18), (1.45) and (1.47), we have

$$\hat{v}_u(\omega) = \frac{\left\{\mathrm{i}(k_1+k_2) + (\frac{1}{4H_1} - \frac{1}{4H_2})\right\} \mathrm{e}^{\mathrm{i}k_1 h}}{\mathrm{i}k_1(\mathrm{e}^{\mathrm{i}k_1 h} + \mathrm{e}^{-\mathrm{i}k_1 h}) + \mathrm{i}k_2(\mathrm{e}^{\mathrm{i}k_1 h} - \mathrm{e}^{-\mathrm{i}k_1 h}) + (\frac{1}{4H_1} - \frac{1}{4H_2})(\mathrm{e}^{\mathrm{i}k_1 h} - \mathrm{e}^{\mathrm{i}k_1 h})} \frac{v_o}{2\sqrt{\pi b}} \mathrm{e}^{-\frac{\omega^2}{4b}}. \tag{1.51}$$

We now introduce one more dimensionless variable in addition to the ones introduced earlier

$$\lambda = \frac{v_0}{\omega_{c_1} L} \quad , \tag{1.52}$$

where λ is a parameter which gives the strength of the jerking at the footpoint. Using the dimensionless variables we write down the expressions of displacements (given in Appendix A). To calculate the displacements, we evaluate the integrals numerically. For $\alpha = 0.5$ and $r = 0.3$, the displacements have been plotted versus altitude for different times in Figures 1.2*a,b*. As in CAP, here also we find that for slow footpoint motion (*i.e.*, $\lambda = 0.2$), the flux tubes always remain close to vertical while being shifted. For stronger footpoint motion (*i.e.*, $\lambda = 1.0$), the disturbance is found to propagate as a kink pulse and the flux tube oscillates for some time before relaxing. Whenever a pulse propagates through a stratified medium, it is known to leave a wake behind it oscillating with the cutoff frequency of the atmosphere (Lamb 1932; Rae and Roberts 1982). For a single layer solar atmosphere model, CAP clearly shows the evidence of a wake oscillating with the cutoff frequency. In our two-layer model, however, the situation is somewhat more complicated, since each layer has its own characteristic cutoff frequency. Figures 1.3*a-c* show wakes for three different combinations of α and λ. From Figure 1.3*a*, we find that

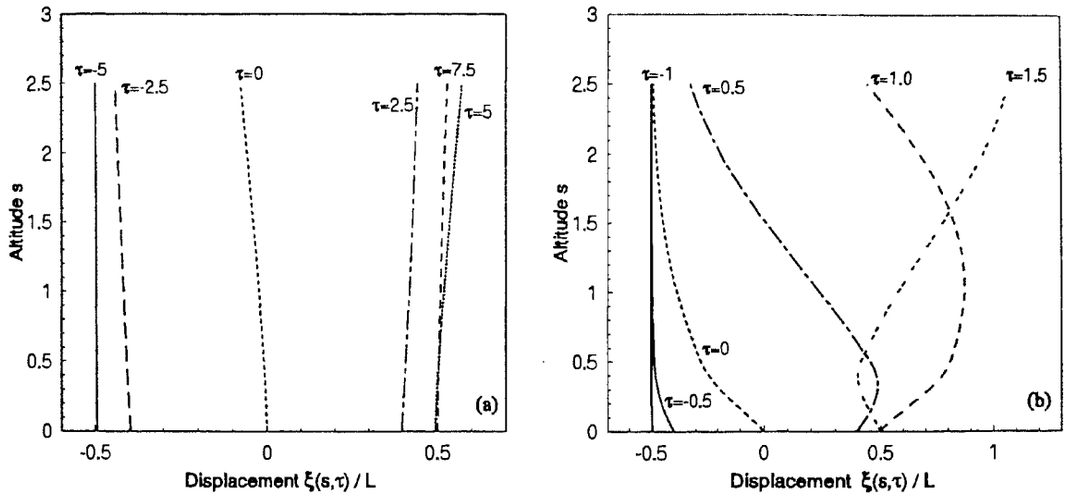

Figure 1.2: Displacement ξ (in units of the total displacement L) of the magnetic flux tube as a function of altitude $s(= z/4H_1)$ at various instants $\tau(= \omega_{c_1} t)$ for (a) $\lambda = 0.2$ and (b) $\lambda = 1.0$.

for not too large λ and α, the wake mainly oscillates with the cutoff frequency of the upper layer, which corresponds for $r = 0.3$ to a period of 6π in our dimensionless units. A careful look at Figure 1.3*a*, however, reveals the existence of another frequency with a very low amplitude. The amplitude of this frequency grows with increasing λ (*i.e.*, stronger footpoint motion) as in Figure 1.3*c* or with increasing α (*i.e.*, thicker lower layer) as in Figure 1.3*b*. This new frequency is neither the cutoff of the lower layer nor that of the upper layer. It has a value somewhat, though not very, close to $\omega_{c_1} + \omega_{c_2}$, which corresponds to a period $1.54\,\pi$. Presumably this frequency is due to the coupling between the two layers and becomes more prominent as the effect of the lower layer becomes more dominant. We now discuss how to find out the energy transmitted to the corona. The expression for energy per unit length of the flux tube at a particular altitude at an instant of time (using dimensionless units) is

$$\mathcal{E}(s,\tau) = \frac{1}{2}\rho_1(s)A_1(s)\dot{\xi}_1^2(s,\tau)\omega_{c_1}^2 \quad \text{for} \quad s \leq \alpha \quad , \tag{1.53}$$

$$= \frac{1}{2}\rho_2(s)A_2(s)\dot{\xi}_2^2(s,\tau)\omega_{c_1}^2 \quad \text{for} \quad s > \alpha \quad , \tag{1.54}$$

where the dot represents differentiation with respect to $\tau = \omega_{c_1} t$. We can easily find $\dot{\xi}_1(s,\tau)$ and $\dot{\xi}_2(s,\tau)$ by differentiating the expressions (A1) and (A2). The expressions for $\rho_1(s)$, $\rho_2(s)$, $A_1(s)$, $A_2(s)$ are obtained from equations (1.21) - (1.22) , on substituting

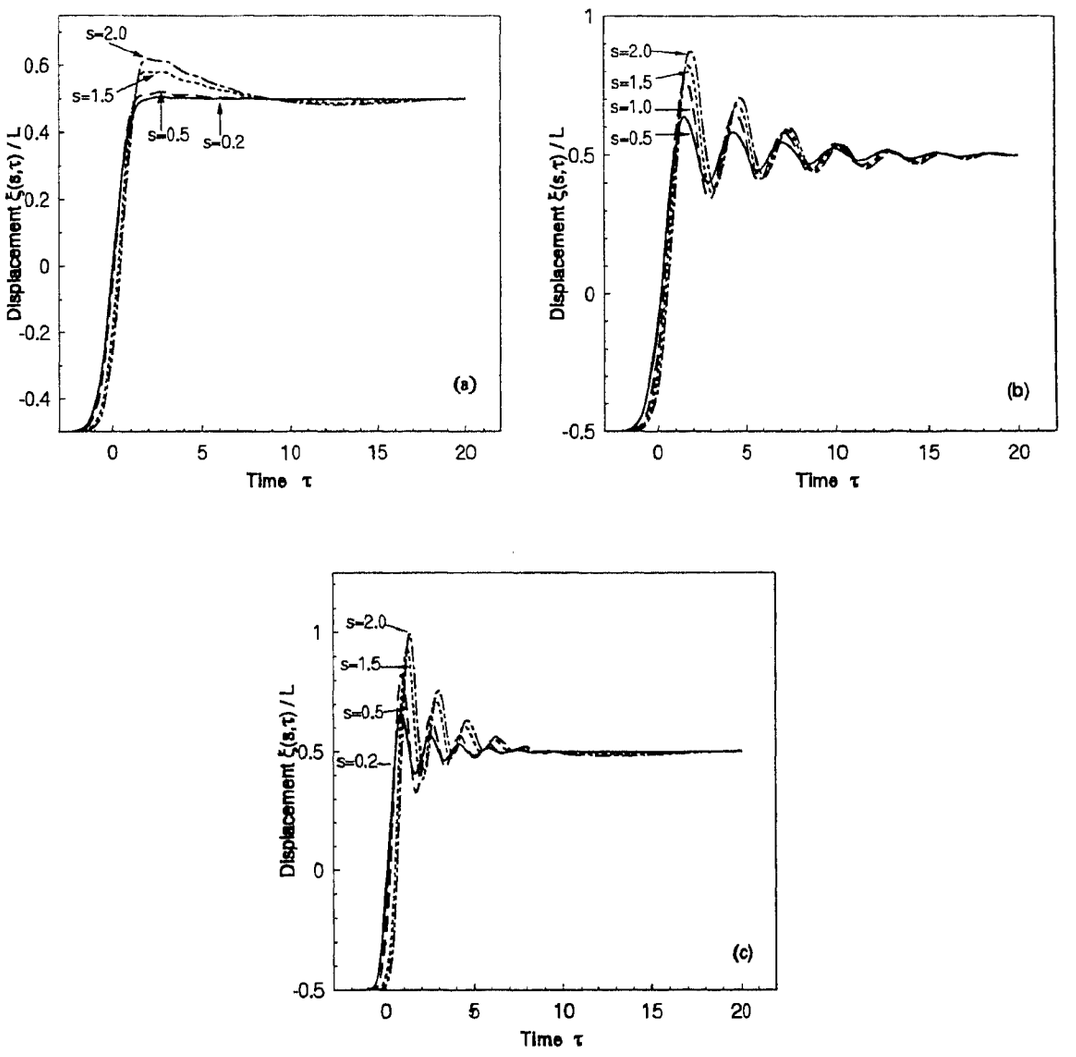

Figure 1.3: Displacement ξ of the magnetic flux tube as a function of time τ at various altitudes s for (a) $\lambda = 0.5$, $\alpha = 0.5$, $r = 0.3$, (b) $\lambda = 0.5$, $\alpha = 1.0$, $r = 0.3$, (c) $\lambda = 1.0$, $\alpha = 0.5$, $r = 0.3$.

$4H_1 s$ for z. We evaluate $\mathcal{E}(s,\tau)$ numerically and plot it against the altitude s for three values of τ in Figure 1.4 (taking $r = 0.3, \alpha = 1.0, \lambda = 1.0$). When τ is small, the energy has not propagated much and we find the maximum of it is residing in the first layer. But after a while, when it reaches the second layer, suddenly its speed of propagation increases as a result of the larger group velocity $\frac{d\omega}{dk}$ in the upper layer, whereas its amplitude falls due to the jump to lower density. Hence we find that the amplitude of the energy density suddenly drops in the upper layer, though the energy propagates more quickly to the higher altitudes so that the energy conservation is not violated. To

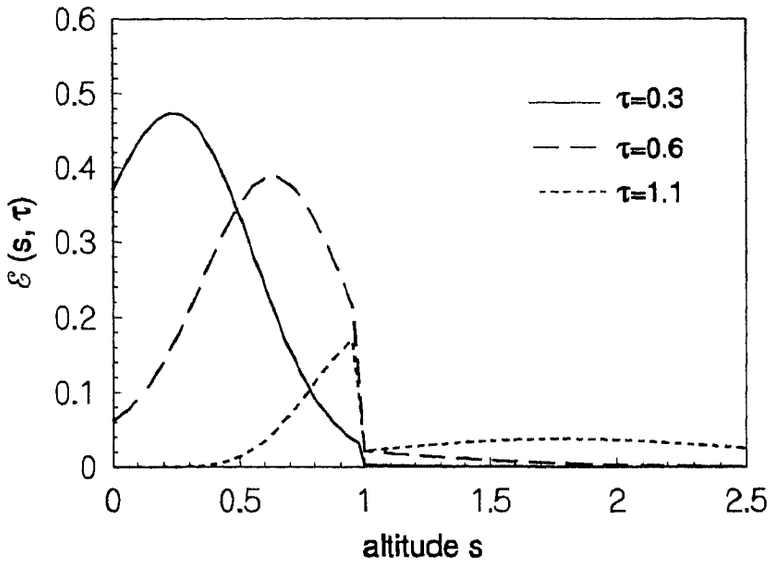

Figure 1.4: Energy density $\mathcal{E}(s,\tau)$ per unit length of the flux tube as a function of altitude s at various instants τ for $\alpha = 1.0$, $\lambda = 1.0$, $r = 0.3$

find out the total kinetic energy $\mathcal{E}_{tot}(\tau)$ residing in the whole flux tube, we integrate $\mathcal{E}(s,\tau)$ from $s = 0$ to $s = \infty$, which gives

$$\mathcal{E}_{tot}(\tau) = \frac{4\rho_{1,0}A_{1,0}v_{1,0}^2 H_1}{\lambda^2} F(\lambda, \alpha, r, \tau), \tag{1.55}$$

where $F(\lambda, \alpha, r, \tau)$,is given in Appendix A. The total energy can be obtained by multiplying $\mathcal{E}_{tot}(\tau)$ with (Spruit 1981).

$$C = 3 + \frac{\rho_e}{\rho} + \frac{1}{\beta}. \tag{1.56}$$

Though $F(\lambda, \alpha, r, \tau)$ is more complicated than the function $F(\lambda, \tau)$ introduced by

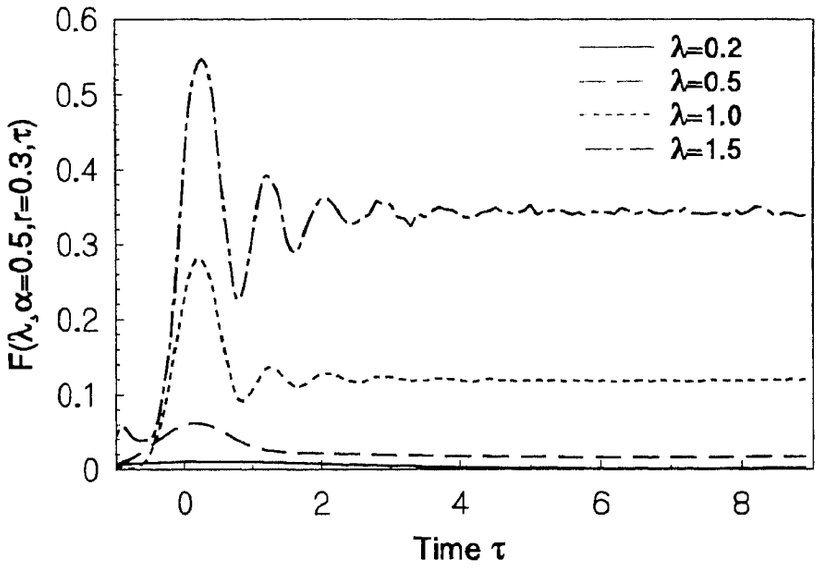

Figure 1.5: Total kinetic energy $F(\lambda, \alpha, r, \tau)$ as a function of time τ for several values of λ for fixed $\alpha = 0.5$ and $r = 0.3$.

CAP, there are some resemblances. This is made clear in Figure 1.5, which plots $F(\lambda, \alpha = 0.5, r = 0.3, \tau)$ as a function of τ for different values of λ. This figure is strikingly similar to Figure 4 in CAP. We again see that $F(\lambda, \alpha, r, \tau)$, which is a measure of the flux tube energy, oscillates for some time depending on whether the footpoint motion works on the flux tube or the flux tube returns the energy due to the evanescent modes to the footpoints. Eventually when the footpoint stops, $F(\lambda, \alpha, r, \tau)$ reaches a steady asymptotic value $F_{\text{asy}}(\lambda, \alpha, r)$ for large τ. The energy transmitted to the corona is given by

$$\mathcal{E}_{\text{corona}} = \frac{4C\rho_{1,0}A_{1,0}v_0^2 F_{\text{asy}}(\lambda, \alpha, r)}{\lambda^2}. \tag{1.57}$$

1.5 Parameter space study

We have already seen in CAP that the nature of magnetic kink pulse propagation in an isothermal atmosphere depends on the value of only one dimensionless parameter λ, which is a measure of the rapidity of the footpoint motion with respect to the cutoff frequency of the atmosphere. For the two-layer atmosphere, however, the problem becomes much richer with the introduction of two additional dimensionless parameters r and α, which are respectively the measures of the temperature contrast between the two layers and the thickness of the lower layer. Before choosing the values of these parameters appropriate for the solar atmosphere (done in the next Section), we first study the basic physics of pulse propagation in the two-layer atmosphere by allowing the parameters to have different possible values. We, however, restrict ourselves to the study of situations in which the upper atmosphere is hotter (which implies $0 < r < 1$), since the mathematical expressions derived in the last Section are valid only for this case. The temperature jump disappears for $r = 1$ and becomes more prominent for smaller r. The other parameter α can lie in the range $0 < \alpha < \infty$, the limiting values 0 and ∞ corresponding to isothermal atmospheres with temperatures T_2 and T_1 respectively. As seen in equation (A9), the energy transmitted to the corona depends on all these three parameters.

Though a pulse involves the superposition of many Fourier modes, a value of λ much less than unity indicates the presence of mainly evanescent modes in the lower layer. In §1.2, we have discussed the possibility of tunnelling of energy to the hotter upper atmosphere even for modes evanescent in the lower layer (provided the lower layer is not too thick, *i.e.*, α is not too large). We expect such tunnelling to be noticeable mainly when λ is small. On the other hand, a larger λ implies the presence of propagating modes. For such modes, energy is reduced due to reflection and this is expected to be more important when λ is larger. Hence we may use the following rule of thumb: energy transmission at low λ is dominated by tunnelling (provided α is small), whereas energy transmission at higher λ is dominated by reflection. This rule of thumb will help us a lot to make sense of the rich data we are presenting below. For a given set of values of the three parameters λ, α, r, we numerically evaluate $F_{asy}(\lambda, \alpha, r)/\lambda^2$ by using equation (A9). The energy transmitted to the corona can then be subsequently

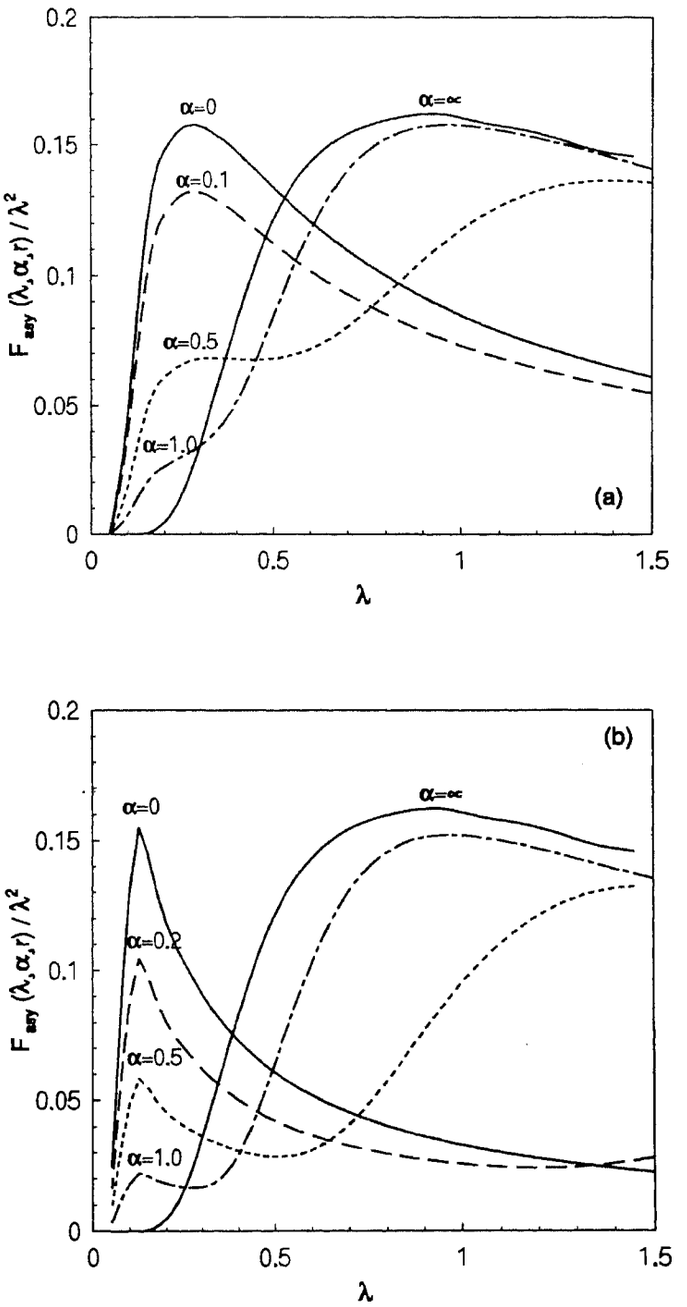

Figure 1.6: Plot of $F_{asy}(\lambda, \alpha, r)/\lambda^2$ (which is energy transmitted to the corona divided by $4C\rho_{1,0}A_{1,0}v_0^2$) as a function of λ for different α's for (a) $r = 0.3$, (b) $r = 0.1$.

calculated by multiplying this with $4C\rho_{1,0}A_{1,0}v_0^2H_1$, as seen in equation (1.57). In Figures 1.6*a,b*, we plot $F_{\rm asy}(\lambda,\alpha,r)/\lambda^2$ against λ for two definite values of r ($r = 0.3$ for Figure 1.6*a* and $r = 0.1$ for Figure 1.6*b*). In each of the Figures 1.6*a* and 1.6*b*, we plot several curves corresponding to different values of α. As we have already mentioned, $\alpha = \infty$ corresponds to an isothermal atmosphere with temperature T_1. As the interface between the two layers is lowered by reducing α, the reflection becomes more important and the energy flux is initially reduced, except for very low values of λ where the tunnelling becomes dominant as pointed out in our rule of thumb. This is clearly seen in Figures 1.6*a,b*, where we find that the energy transmission at sufficiently low λ is always enhanced by reducing α to make tunnelling more efficient. When α is sufficiently small, the tunnelling becomes so important that it can overcome the reflection and the flux may increase with decreasing α even for high values of λ. Finally when $\alpha = 0$, the curve corresponds to an isothermal atmosphere with temperature T_2. This curve has the same maximum value as the curve for $\alpha = \infty$ corresponding to the isothermal atmosphere with temperature T_1. In fact, it appears that one just has to shrink the curve for $\alpha = \infty$ in the horizontal direction in order to get the curve for $\alpha = 0$. We show below that this is indeed true and one can get one curve from the other by a simple scaling.

From CAP, one can easily see that the energy transmitted to an isothermal atmosphere divided by $4C\rho_0A_0v_0^2H$ is a function of $\lambda(= v_0/\omega_cL)$ alone, *i.e.*

$$\frac{\mathcal{E}_{\rm corona}(\lambda,\alpha=\infty,r)}{4C\rho_{1,0}A_{1,0}v_0^2H_1} = G(\lambda). \tag{1.58}$$

Here we have taken $\lambda = v_0/\omega_{c_1}L$. Since $\alpha = 0$ also corresponds to another isothermal atmosphere where the cutoff frequency is $\omega_{c_2} = r\omega_{c_1}$, the quantity $\mathcal{E}_{\rm corona}(\lambda,\alpha = 0,r)/4\rho_{2,0}A_{2,0}v_0^2H_2$ has to have similar functional dependence on $\lambda' = v_0/\omega_{c_2}L = \lambda/r$. Therefore

$$\frac{\mathcal{E}_{\rm corona}(\lambda,\alpha=0,r)}{4C\rho_{2,0}A_{2,0}v_0^2H_2} = G(\frac{\lambda}{r}) = \frac{\mathcal{E}_{\rm corona}(\frac{\lambda}{r},\alpha=\infty,r)}{4C\rho_{1,0}A_{1,0}v_0^2H_1}. \tag{1.59}$$

From equations (1.26), (1.28), and the fact that scale heights are proportional to temperature, it is easy to show that $\rho_{2,0}A_{2,0}H_2 = \rho_{1,0}A_{1,0}H_1$. Hence it follows from equations (1.57) and (1.59) that

$$\frac{F_{\rm asy}(\lambda,\alpha=0,r)}{\lambda^2} = \frac{F_{\rm asy}(\lambda/r,\alpha=\infty,r)}{(\lambda/r)^2}. \tag{1.60}$$

The equation(1.60) clearly explains why the curve corresponding to one isothermal atmosphere is shrunk r times (as one finds in the Figures 1.6*a,b*) to produce the curve corresponding to another isothermal atmosphere which is $1/r^2$ times hotter. It is seen in both Figures 1.6*a* and 1.6*b* that the curves corresponding to $\alpha = \infty$ (*i.e.*, for isothermal atmosphere with temperature T_1) have maxima at about $\lambda = 0.9$. It is clear from the scaling equation (1.60) that the curves for $\alpha = 0$ (*i.e.*, for isothermal atmosphere with temperature T_2) will have maxima at $\lambda/r = 0.9$, the peak value at the maxima being the same as the peak value for the $\alpha = \infty$ curve. This is clearly borne out in Figures 1.6*a,b*. In fact, it will help us to understand some of the results presented below if we remember the fact that $F_{asy}(\lambda, \alpha, r)/\lambda^2$ for small values of α becomes largest when λ/r is close to 0.9. How the reflection and the tunnelling depends on the temperature contrast

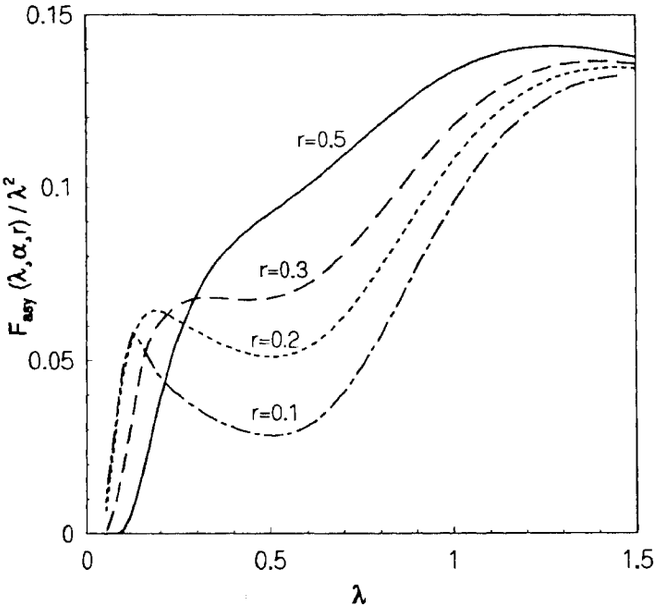

Figure 1.7: Plot of $F_{asy}(\lambda, \alpha, r)/\lambda^2$ as a function of λ for several values of temperature contrast r for a particular $\alpha = 0.5$.

between the two layers becomes clear in Figure 1.7, in which we plot $F_{asy}(\lambda, \alpha, r)/\lambda^2$ against λ for several values of the temperature contrast (smaller r implying larger contrast), while the thickness of the lower layer is held constant ($\alpha = 0.5$). For larger λ, the effect of reflection is more dominant and the flux decreases on increasing the

temperature contrast (*i.e.*, decreasing r). For very small values of λ, on the other hand, the tunnelling is more important and the flux increases as the upper layer is made hotter (by decreasing r). Thus we clearly establish the fact that the energy flux is not always diminished by reflection in the presence of a temperature jump, but the flux can actually be enhanced under certain circumstances due to the increased tunnelling. This is an interesting new result which would not become apparent in a Fourier mode analysis and requires the study of a pulse propagation for its derivation.

Figures 1.8*a,b,c*, which plot $F_{\rm asy}(\lambda,\alpha,r)/\lambda^2$ against r for three different values of λ, bring out more clearly the dependence on the temperature contrast. In Figure 1.8*a* with $\lambda = 1.0$, the reflection is more important and the flux decreases with larger temperature contrast (smaller r) for any value of α. On the other hand, for Figure 1.8*c* with $\lambda = 0.2$, we expect the tunnelling to be dominant and the flux to increase with smaller r. This is seen on right side of the figure. However, all the curves have maxima close to $\lambda/r = 0.9$ for reasons explained above. In Figure 1.8*a*, the flux is enhanced on increasing the height of the lower layer (*i.e.*, increasing α), which makes reflection less efficient. In Figure 1.8*c*, however, the flux is enhanced on decreasing α, since tunnelling is more important in this case. Figure 1.8*b* presents curves for an intermediate value of λ, for which the results are more complicated. Finally Figures 1.9*a,b* show how the energy flux varies with the thickness of the lower layer. These figures present $F_{\rm asy}(\lambda,\alpha,r)/\lambda^2$ plotted against α for two different values of λ. Figure 1.9*a* is for $\lambda = 1$, which makes reflection important. Unless α is very small to make tunnelling important, the flux increases with height, since there is less reduction of flux due to reflection as the interface between the layers is moved higher up. The curves for higher temperature contrast (lower r) lie lower, because there is more reflection when the contrast is more. When α is sufficiently large so that hotter upper layer is far away from the footpoint, the flux becomes independent of the temperature of the upper layer and curves for different values of r coalesce. Figure 1.9*b* is for $\lambda = 0.2$ so that the tunnelling is dominant and we find more energy to tunnel through when the height is less. The tunnelling is expected to be more efficient when the upper layer is hotter (*i.e.*, when r is smaller). Hence we may expect the curves for lower r to lie higher, which is true for $r = 0.1$ and $r = 0.5$. For $r = 0.2$ and $r = 0.3$, however, we have λ/r sufficiently

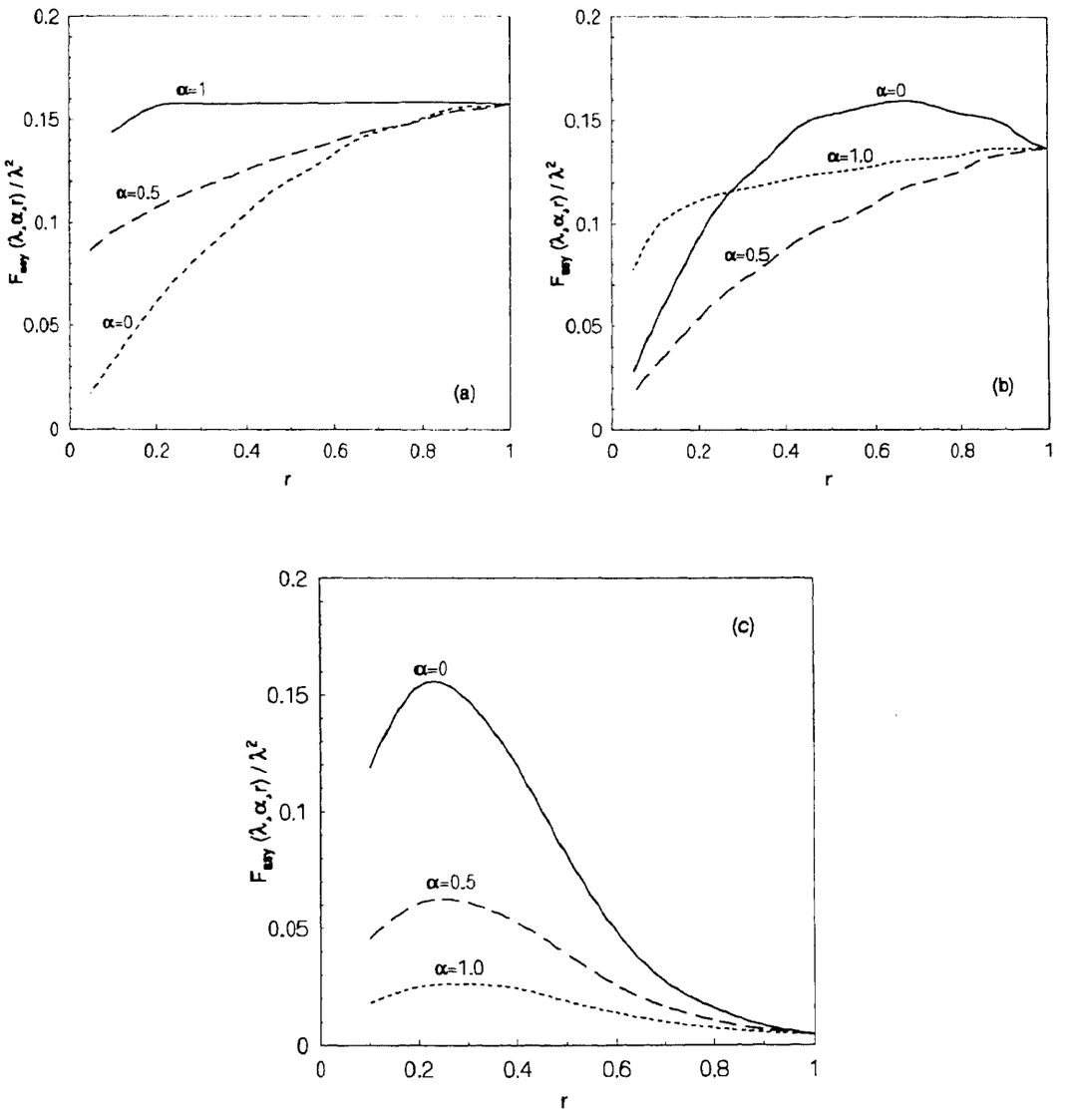

Figure 1.8: Plot of $F_{asy}(\lambda, \alpha, r)/\lambda^2$ as a function of temperature contrast r for different α (i.e thickness of the first layer) : (a) $\lambda = 1.0$, (b) $\lambda = 0.6$, (c) $\lambda = 0.2$.

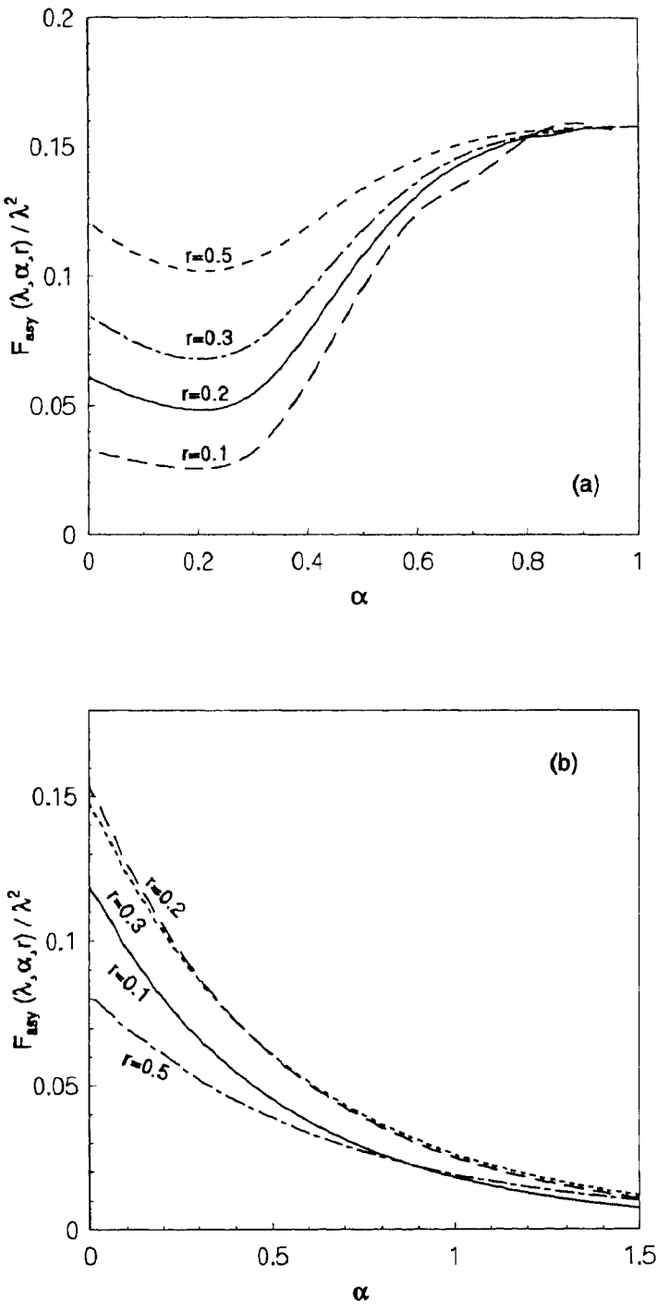

Figure 1.9: Plot of $F_{asy}(\lambda, \alpha, r)/\lambda^2$ as a function of α (*i.e.*thickness of the first layer) for several values of temperature contrast r : $(a)\lambda = 1.0$, (b) $\lambda = 0.2$.

close to 0.9, which makes the energy flux for these cases larger.

1.6 Application to the Solar atmosphere

Our task now is to calculate the energy transmitted to the corona and compare with the results of CAP for isothermal atmosphere. The isothermal atmosphere of 6000 K temperature extending above the photosphere, which was used in CAP, will be referred to as Model I. If one looks at the temperature-altitude curve of a standard solar atmosphere model above the photosphere (Figure 1.2 in Priest 1982), one finds that there is a temperature jump to about 50000 K around a height of 1500 km above the temperature minimum, and then there is another jump to temperatures of about 5×10^5 K around a height of 2000 km at the base of the low corona. The temperature plateau region between the two jumps was introduced in the earlier semi-empirical models in order to account for the emission measure of the Lyman line observations (Vernazza, Avrett and Loeser 1981). A more recent study by Fontenla, Avrett and Loeser (1990), however, suggests that the temperature plateau is no longer needed if one includes ambipolar diffusion and hence a two-layer model is a good representation of the solar atmosphere. If we want to fit a two-layer model, perhaps the best option is to consider a hundred-fold temperature jump at 2000 km height. This is achieved by taking $r = 1/10$, $\alpha = 2.0$ (using the fact that the scale height near the temperature minimum is about 250 km). We refer to this as Model II. In order to see the effect of the lower edge of the temperature plateau, if it exists, we also consider a Model III with $r = 1/3$, $\alpha = 1.5$, which corresponds to a nine-fold temperature increase at a height of 1500 km.

Before presenting the results, we use equation (1.57) to write the expression for the asymptotic energy in a convenient form as in CAP:

$$\mathcal{E}_{\rm corona} = 10^{26} C \left\{ \frac{\rho_{1,0}}{10^{-7}{\rm gmcm}^{-3}} \right\} \left\{ \frac{A_{1,0}}{10^5{\rm km}^2} \right\} \left\{ \frac{v_0}{1{\rm kms}^{-1}} \right\}^2 \left\{ \frac{H_1}{250{\rm km}} \right\} \frac{F_{\rm asy}(\lambda, \alpha, r)}{\lambda^2} \quad {\rm erg.} \tag{1.61}$$

It has been estimated in CAP that fast footpoint motions correspond to $\lambda = 0.44$, $v_0 = 3$ km/s, whereas slow footpoint motions correspond to $\lambda = 0.22$, $v_0 = 1$ km/s. Figure 1.10 shows a set of plots of $F_{\rm asy}(\lambda, \alpha, r)/\lambda^2$ for the three models described above. One can now read off the value of $F_{\rm asy}(\lambda, \alpha, r)/\lambda^2$ for a particular λ from Figure 1.10

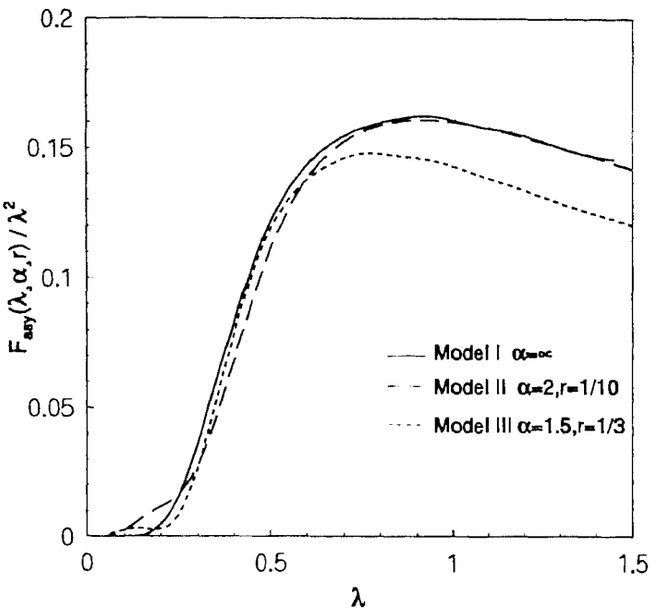

Figure 1.10: Plot of $F_{asy}(\lambda, \alpha, r)/\lambda^2$ against λ for the three models appropriate to the solar case.

and then the energy can be calculated by using equation (1.61). We take the density at the photospheric level $\rho_{1,0} = 3 \times 10^{-7}\text{gmcm}^{-3}$, the cross-sectional area of the flux-tube $A_{1,0} = 0.5 \times 10^5\text{km}^2$ and the scale height $H_1 = 250$ km. We follow Spruit (1981) to take the constant C (defined in eq. [38]) to have a value 6.5. The values of $\mathcal{E}_{\text{corona}}$ for all the three models are given in Table 1.1. for both fast and slow footpoint motions.

One can finally estimate the energy flux by multiplying $\mathcal{E}_{\text{corona}}$ by the number density of footpoints and the frequency of motions. Assuming that there are about 10 footpoints in an area of 10^4 km $\times$ 10^4 km, we get a number density of 10^{-17}cm^{-2}. Since slow footpoint motions have granular time scales, we take the frequency to be about 1 in 500 s. The fast footpoint motions are less frequent and so far we do not have very reliable data on their frequency (Muller *et al.* 1994). For the purpose of rough estimate, let us take the frequency of fast motions to be once in 5000 s, *i.e.*, 10 times infrequent compared to the slow footpoint motions. Hence the energy flux due to fast footpoint motions alone and slow footpoint motions alone can be obtained by multiplying $\mathcal{E}_{\text{corona}}$ by respectively $2 \times 10^{-21}\text{cm}^{-2}\text{s}^{-1}$ and 2×10^{-20}. The values of energy flux for the three

	Fast motions ($\lambda = 0.44$, v_0=3 km s^{-1})		Slow motions ($\lambda = 0.22$,v_0=1 km s^{-1})	
	$\mathcal{E}_{\rm corona}$ (ergs)	Net flux (ergs cm^{-2} s^{-1})	$\mathcal{E}_{\rm corona}$ (ergs)	Net flux (ergs cm^{-2} s^{-1})
Model I ($\alpha = \infty$)	8.75×10^{26}	1.75×10^{6}	9.50×10^{24}	1.90×10^{5}
Model II ($\alpha = 2.0, r = 1/10$)	8.35×10^{26}	1.67×10^{6}	6.00×10^{24}	1.20×10^{5}
Model III ($\alpha = 1.5, r = 1/3$)	7.90×10^{26}	1.58×10^{6}	1.45×10^{25}	2.90×10^{5}

Table 1.1: Energy flux for different cases.

models are also presented in Table 1.1. The reader is reminded that the energy flux to heat the quiet corona is estimated to be about 3×10^5erg cm^{-2}s^{-1} (Hollweg 1990a).

There are several things to be noted in Figure 1.10 and Table 1.1. Firstly, the curve for Model I in Figure 1.10 is not very different from the other two curves. Given the other uncertainties in the model, one concludes that an isothermal atmosphere is not a bad model for the solar atmosphere as far as the propagation of magnetic kink modes are concerned. Secondly, the two-layer calculations reinforce the main conclusion of CAP that the fast footpoint motions are much more important for transporting energy to the corona compared to the slow motions, even though the fast motions may be much less frequent. This is because the individual fast motions cause a much larger $\mathcal{E}_{\rm corona}$ than the individual slow motions – both due to a larger v_0 and a larger $F_{\rm asy}(\lambda, \alpha, r)/\lambda^2$. Hence, the contribution made by fast motions, though infrequent, is more substantial. In fact, as seen in Table 1.1, the energy flux due to slow footpoint motions alone for all the models falls slightly short of the requirement for heating the quiet corona. On the other hand, the rapid footpoint motions alone can provide the necessary energy flux. It is to be noted from Figure 1.10 that energy flux for rapid footpoint motions is slightly reduced in going from the isothermal model to the two-layer model, which is obviously due to reflection. But the energy flux for slow footpoint motions may get somewhat enhanced due to tunnelling as we go to the two-layer model.

In summary, we identify the rapid footpoint motions as the potential source for supplying energy in the form of magnetic kink waves for heating the quiet corona. The slow

motions alone would not have provided adequate energy.

1.7 Discussion

There are two aspects of the coronal heating problem. Firstly, we have to understand how energy is transported to the corona. Secondly, we have to show that the energy can be dissipated at the correct altitude. Here we are concerned only with first question of the energy transport. We point out that horizontal motions of photospheric footpoints of flux tubes would give rise to kink waves. Though footpoint motions having granular time and velocity scales may not be sufficient for providing adequate energy, we identify the occasional rapid footpoint motions as the potential source of energy for coronal heating. The slower motions dump energy mainly around the cutoff frequency, whereas the rapid footpoint motions put a substantial part of the energy above the cutoff so that the energy transport is much more efficient. Since we do not yet have sufficient data to do a proper statistical study of the rapid footpoint motions (Muller *et al.* 1994), it is difficult to make a very accurate estimate of the energy flux. A rough estimate clearly shows that the energy flux should be more than enough. Because of the importance of the rapid footpoint motions for coronal heating, more extensive observational data on such motions are urgently needed. One would also like to know how these rapid motions are produced - whether by exploding granules or by other means. We hope that future observations will clarify many of these issues.

The main thrust of this work as compared to CAP was to study how the propagation of the kink waves is affected by the temperature jump at the chromosphere-corona transition layer. Previous studies of wave propagation in the presence of temperature jump were done most extensively for the shear Alfvén mode (Hollweg 1981, 1984; Zhugzhda and Locans 1982), and it was found out that the reflection at the transition layer can reduce the energy flux substantially. These studies led to the suspicion that energy flux due to all other wave modes also may similarly be drastically reduced by reflection and not enough energy may reach the corona (Hollweg 1990a). We point out that the shear Alfvén mode is somewhat special in the sense of not having a cutoff frequency and show that the propagation of kink modes having a cutoff is a very different and a richer problem. Only in the high frequency limit (*i.e.*, when the frequency is much

larger than the cutoff frequency), the kink mode behaves similar to the shear Alfvén mode. In the solar atmosphere, however, we are in the opposite limit of the frequencies being comparable to the cutoff frequency. In this limit, the study of a pure Fourier mode does not provide adequate insight into how a pulse may propagate. Hence we have carried out calculations for pulses made up of frequencies in the different ranges. Most of the studies of the shear Alfvén mode treated only pure Fourier modes, which are good proxies for Alfvenic pulses. We have actually demonstrated some cases where the energy flux is enhanced due to the presence of a temperature jump and dispelled the worry that the energy flux would always be reduced by a temperature gradient.

We have concluded that the isothermal atmosphere model used in CAP is a fairly good model for propagation of kink pulses in the solar atmosphere. This is because of the fact that the temperature jump takes place several scale heights above the photosphere and the energy transport is not much affected by what is happening several scale heights above the footpoints, which act as drivers of the kink pulses. This is clearly seen in Figures 1.6*a,b*, which show that the curves for $\alpha = 1.0$ are not very different from the curves for $\alpha = \infty$. One assumption in our calculations was to neglect the merger of neighboring flux tubes above the chromosphere (Spruit 1984). However, since this merger takes place several scale heights above the photosphere, we feel that the merger also will not change the energy transport substantially, though this has to be proved by detailed calculations. We wish to look at this aspect in near future. Another assumption was to neglect the nonlinearities which must become important in the higher regions where the amplitudes are large. Nonlinear calculations for the sausage mode by Hollweg (1982) showed results very similar to the linear results of Rae and Roberts (1982), and we expect this to be true for kink modes also. We hope that more detailed simulations of kink pulse propagation in the solar atmosphere will be carried out in future by incorporating nonlinearities and by going beyond the thin flux tube approximation.

Similar work has been reported by Huang *et al.* (1995), who numerically investigated the nonlinear time-dependent response to purely transverse shaking of a thin exponentially spreading vertical magnetic flux tube embedded in a solar convection zone and atmosphere model.

Though our calculations were done specifically for the kink mode, we believe that

some of the general features we obtained will be true for the propagation in a two-layer atmosphere of other kinds of modes with different cutoffs in the two layers. Purely acoustic waves and sausage waves on flux tubes are expected to behave very similarly. This gives us the hope that our results with some modifications might be useful in other situations also, especially to the problem of wave propagation in stellar and planetary atmospheres of other types.

Chapter 2

The Influence of a Vertical Magnetic Field on Oscillations

2.1 Introduction

In the past twentyfive years, observations of oscillations with periods in a fairly broad range of frequencies have been reported in magnetic elements of the solar atmosphere (e.g., Beckers and Schultz 1972; Giovanelli, Harvey and Livingston 1978; Moore and Robin 1985). A study of wave motions can reveal useful information about the nature of magnetic structures. The aim of the present study is to contribute towards developing a theory for such wave motions, also known as magnetoatmospheric oscillations.

The first theoretical study of magnetoatmospheric waves was initiated by Ferraro and Plumpton (1958; hereafter FP), where solutions for a stratified isothermal atmosphere with a vertical magnetic field were obtained. This analysis was carried further by Zhugzhda and Dzhalilov (1979, 1982, 1984a,1984b), in which exact solutions were obtained in terms of Meijer functions. Any theory has to take into account the variable structure of the atmosphere in the vertical direction. Local dispersion relations based on a WKB approach had earlier been used (McLellan and Winterberg 1968; Nagakawa, Priest and Walleck 1973) to study wave modes in a magnetized stratified atmosphere. However, in order to determine accurately the frequency spectrum, global dispersion relations are needed. These are usually difficult to obtain in terms of analytic expressions, apart from certain limits. The frequency spectrum in the strong-field limit was calculated analytically in the quasi-Alfvénic approximation by Uchida and Sakurai (1975) and numerically by Scheuer and Thomas (1981), Hasan and Abdelatif (1990), Abdelatif

(1990), Wood (1990). Hasan and Christensen-Dalsgaard (1992; hereafter HC) extended this analysis to the weak-field limit, and obtained an analytic dispersion relation for the wave modes. Despite the mathematical progress, the physical properties of the solutions have not been fully explored. The stratification allows mutual transformation of waves, so that in general the problem can not be examined in terms of the elementary modes of a nonstratified magnetized atmosphere. HC has examined the effect of a weak field on the normal modes of a stratified isothermal atmosphere and demonstrated that the normal modes of a magnetized atmosphere can be analyzed to lowest order in terms of elementary wave modes of an unmagnetized atmosphere along with purely magnetic modes. Mode coupling was also studied and it was shown that this coupling becomes particularly important at the locations in the diagnostic diagram where the frequencies of different elementary modes coincide.

In the present work we extend the previous analysis, for different sets of boundary conditions. We attempt to analyze the physical nature of magneto-acoustic-gravity (or MAG) oscillations and also to understand the cause for the existence of different types of elementary wave modes in a magnetic isothermal atmosphere subject to different sets of boundary conditions. We examine how the normal modes of an unmagnetized stratified atmosphere are modified by the introduction of a small vertical magnetic field. The results are compared with those for the non-magnetic case, and the nature of coupling between the elementary wave modes and their properties in the different regions of the diagnostic diagram is analyzed. In the present study, we shall be concerned primarily with nonradial modes (*i.e.*, modes with finite horizontal wave number).

For vertical fields, the effect on $p-$mode frequencies due to scattering off flux tubes has been addressed by Zweibel and Bogdan (1986), Bogdan and Zweibel (1985), and Bogdan and Cattaneo (1989), but the stratification was neglected in these studies. Mode coupling in a stratified atmosphere with a strong magnetic field has been studied by Hasan and Abdelatif (1990) and Abdelatif (1990), and in a general field by Spruit and Bogdan (1992). Abdelatif (1990) elucidated the frequency behavior in the $K - \Omega$ diagram in the strong-field case. showing that it could be understood, for small horizontal wave numbers, in terms of the interaction between fast and slow modes. The present study considers both the strong- and weak-field solutions of the wave equation,

with the main emphasis on the latter. In the strong-field limit, our results complement those of Abdelatif (1990) by using the small and large horizontal wave number limits to classify the modes. Our investigation differs from that of Spruit and Bogdan (1992) in two important respects: in the assumed temperature stratification of the atmosphere, and, more importantly, in the methods employed in the analysis of the problem. The primary concern of Spruit and Bogdan was to find a mechanism for converting $p-$modes into downward propagating slow waves, in order to explain $p-$mode absorption in a sunspot. In contrast, we concentrate on examining the normal modes of the system, by combining a semi-analytic approach based on asymptotic dispersion relations with numerical solutions; in this way, it is possible to examine the nature of modes and gain an understanding of their mutual interaction in a vertical magnetic field.

Strictly speaking, the present analysis pertains to homogeneous fields and not to flux tubes. Unfortunately, even the construction of an equilibrium solution for a stratified flux tube is extremely complicated, let alone the question of wave propagation. Most of the analyses of waves in flux tubes have either neglected gravity or used the thin flux tube approximation (see Hollweg 1990b; Roberts 1990; and Thomas 1990 for recent reviews on flux tube waves). The former approach, which neglects the stratification, is inappropriate for application to photospheric flux tubes. The thin flux tube approximation, on the other hand, provides a more reasonable framework for treating wave propagation in intense flux tubes, where the tube radius is typically smaller than the pressure scale height in the vertical direction. However, in addition to its somewhat restrictive scope, this approximation has the limitation that it effectively eliminates the fast mode from the analysis. In the present investigation, it is assumed that the flux tubes in question are sufficiently thick, so that the field can be regarded to have infinite horizontal extent.

The plan of the Chapter is as follows: in §2.2 the basic MHD equations are presented. In §2.3 the coupled wave equation for MAG waves is presented for an isothermal stratified atmosphere in a vertical magnetic field. In §2.4 we present the dispersion relation for a weak field subject to different sets of boundary conditions. We examine the behavior of the solution, when different elementary wave mode frequencies come closer. In §§2.5 and 2.6 numerical results are presented showing the variation of ei-

genfrequencies with horizontal wave numbers for the case of a weak field. In §2.7 we treat the strong-field case and examine the $K - \Omega$ diagram. Finally, a discussion of the results and a comparison with previous studies are taken up in §2.8.

2.2 Ideal magnetohydrodynamic equations

We consider an isothermal plane stratified atmosphere, embedded in a uniform vertical magnetic field B, which is unbounded in the horizontal direction. Using a fluid description and assuming an ideal plasma (*i.e.*, inviscid and with infinite conductivity), the ideal magnetohydrodynamic (MHD) equations are

$$\frac{\partial \rho}{\partial t} + \nabla.(\rho \mathbf{v}) = 0 \ , \tag{2.1}$$

$$\rho \frac{\mathrm{d}\mathbf{v}}{\mathrm{d}t} = \rho g - \nabla p - \frac{1}{4\pi} \nabla \times \mathbf{B} \times \mathbf{B} \ , \tag{2.2}$$

$$\frac{\mathrm{d}}{\mathrm{d}t}\left(\frac{p}{\rho^{\gamma}}\right) = 0 \ , \tag{2.3}$$

$$\nabla.\mathbf{B} = 0 \ , \tag{2.4}$$

$$\nabla \times \mathbf{E} = -\frac{1}{c}\frac{\partial \mathbf{B}}{\partial t} \ , \tag{2.5}$$

$$\mathbf{E} + \frac{1}{c}(\mathbf{v} \times \mathbf{B}) = 0 \ , \tag{2.6}$$

where ρ is the mass density of the fluid, $\mathbf{v}$ is the velocity, p is the pressure, $\mathbf{B}$ is the magnetic field strength and $\mathbf{E}$ is the electric field. The constants g, c, and γ refers to acceleration due to gravity, the speed of light and the ratio of specific heats respectively. Equation (2.1) express continuity of mass, equation (2.2) is the equation of motion, equation (2.3) corresponds to the assumption of an adiabatic fluid (*i.e.*, we ignore the loss of heat by conduction and radiation), equations (2.4) - (2.5) are Maxwell's equations and equation (2.6) is Ohm's law for an infinitely conducting plasma.

2.2.1 Equilibrium

At $t = 0$ (*i.e.*, the unperturbed state) let us assume that the fluid is in hydrostatic equilibrium and that all physical quantities have only z dependence, apart from the magnetic field, which we take to be constant. The equilibrium state can be determined by solving equations (2.1) - (2.6), without the time derivative. Let us also assume that

the velocity is zero in the unperturbed atmosphere. Thus, in equilibrium we have,

$$\frac{\mathrm{d}p}{\mathrm{d}z} = \rho g \tag{2.7}$$

We assume a cartesian geometry where z, the vertical co-ordinate, is measured positive upwards, the gravity acts in the z direction, which is chosen to point away from the Sun. For simplicity, let us assume that the equilibrium atmosphere is isothermal *i.e.*, the temperature is constant with height. This implies that the sound speed is constant with z and is defined as

$$c_S = \sqrt{\frac{\gamma p}{\rho}}\,, \tag{2.8}$$

where the density varies with height according to the law

$$\rho = \rho_0 \mathrm{e}^{-z/H}\,, \tag{2.9}$$

where $H = p/\rho g$ is the scale height of the atmosphere, which is constant for an isothermal medium and ρ_0 is the mass density at $z = 0$.

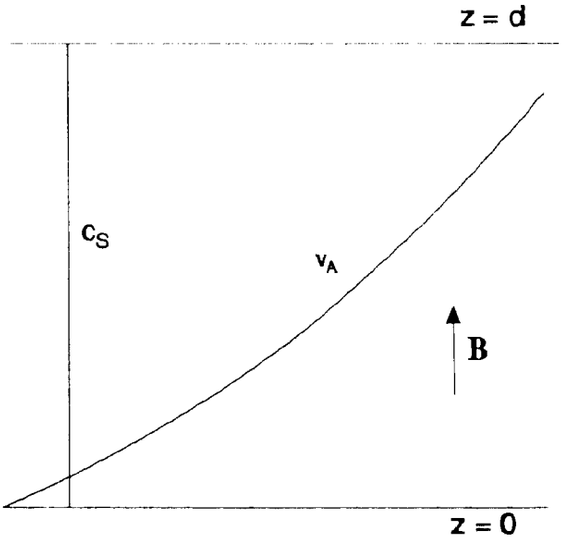

Figure 2.1: The basic geometry of the problem. The region in consideration is isothermal and plane stratified. It has a uniform magnetic field **B** in the vertical direction. The sound speed c_S is constant, but the Alfvén speed is exponentially increasing.

2.2.2 Wave equations in a uniform vertical field

We now consider wave propagation in an ideal stratified atmosphere. This is accomplished by considering small perturbations about the equilibrium. Let ξ denote a Lagrangian displacement of a fluid element from its equilibrium position. This displacement is related to the velocity through the equation

$$\mathbf{v} = \frac{\partial \xi}{\partial t} . \tag{2.10}$$

Expressing all physical variables in equations (2.1) - (2.6) as the sum of an unperturbed part and a small perturbation and retaining only the first order terms in perturbations, we arrive at the following differential equation

$$\rho \frac{\partial^2 \xi}{\partial t^2} = -F(\xi) , \tag{2.11}$$

where

$$F(\xi) = -\nabla \delta p - g\delta\rho - \frac{1}{4\pi}(\nabla \times \delta \mathbf{B} \times \mathbf{B}) , \tag{2.12}$$

$$\delta p = -\gamma p \nabla . \xi - \xi \cdot \nabla p , \tag{2.13}$$

$$\delta \rho = -\rho \nabla . \xi - \xi \cdot \nabla \rho , \tag{2.14}$$

$$\delta \mathbf{B} = \nabla \times (\xi \times \mathbf{B}) , \tag{2.15}$$

where δp ,$\delta\rho$, δB denote Eulerian perturbations in density, pressure and magnetic field respectively.

In cartesian geometry, the linearized equations for MAG waves can be written in terms of the Lagrangian displacement $\xi \sim e^{i(\omega t - kx)}$ as (Ferraro and Plumpton, 1958),

$$[v_A^2 \frac{d^2}{dz^2} - (c_S^2 + v_A^2)k^2 + \omega^2]\xi_x - ik(c_S^2 \frac{d}{dz} - g)\xi_z = 0, \tag{2.16}$$

$$[c_S^2 \frac{d^2}{dz^2} - \gamma g \frac{d}{dz} + \omega^2]\xi_z - ik[c_S^2 \frac{d}{dz} - (\gamma - 1)g\ ]\xi_x = 0, \tag{2.17}$$

$$(\omega^2 + v_A^2 \frac{d^2}{dz^2})\xi_y = 0, \tag{2.18}$$

where k is the horizontal wave number, ω is the frequency and v_A is the Alfvén speed defined as

$$v_A = \frac{B}{\sqrt{4\pi\rho}} , \tag{2.19}$$

Equations (2.16) and (2.17) governs the propagation of MAG waves in a stratified atmosphere. Equation (2.18), which, incidentally, is decoupled from the other equations and describes the purely transverse Alfvén waves, will not be considered in the present investigation. Detailed solutions for Alfvén waves in an isothermal plasma can be found in the paper by FP. We have implicitly assumed that the propagation and motions of the MAG modes are confined to the $x - z$ plane. This involves no loss of generality.

In order to obtain a dimensionless wave equation we introduce three dimensionless parameters

$$K = kH \ , \tag{2.20}$$

$$\Omega = \frac{\omega H}{c_S} \ , \tag{2.21}$$

and the dimensionless vertical coordinate

$$\theta = \frac{\omega H}{v_A} = \frac{c_S}{v_{A,0}} \Omega \, \mathrm{e}^{-z/(2H)} \ , \tag{2.22}$$

where $v_{A,0}$ is the Alfvén speed at $z = 0$. In terms of the variables defined by equations (2.20) - (2.22), equations (2.16) - (2.17) can be combined into the following fourth-order differential equation, which govern the propagation of MAG waves in a stratified atmosphere (Zhugzhda 1979, see also HC) and is given by,

$$\begin{aligned} \Big\{\theta^4 \frac{\mathrm{d}^4}{\mathrm{d}\theta^4} + 4\theta^3 \frac{\mathrm{d}^3}{\mathrm{d}\theta^3} \ &+ \ [1 + 4(\Omega^2 - K^2) + 4\theta^2]\theta^2 \frac{\mathrm{d}^2}{\mathrm{d}\theta^2} - [1 - 4(\Omega^2 + K^2) - 12\theta^2]\theta \frac{\mathrm{d}}{\mathrm{d}\theta} \\ &+ \ 16[(\Omega^2 + K^2(\frac{\Omega_{\mathrm{BV}}^2}{\Omega^2} - 1))\theta^2 - \Omega^2 K^2]\Big\}\xi_x = 0 \ , \end{aligned} \tag{2.23}$$

where $\Omega_{\mathrm{BV}}^2 = (\gamma - 1)/\gamma^2$ is the squared Brunt-Väisälä frequency (in dimensionless units). The general solution of equation (2.23), which can be expressed in terms of Meijer functions (ZD) is given in Appendix B, along with the asymptotic expansions in the weak-field limit.

2.3 Asymptotic properties of normal modes in the weak-field limit

We now examine the asymptotic properties of waves and normal modes of a stratified atmosphere with a weak magnetic field (corresponding to the limit of small ϵ, where $\epsilon = v_{A,0}/c_S$), in order to delineate the influence of the field on the oscillation spectrum.

The analysis is based on the asymptotic solution developed in HC (see Appendix B); here, however, we consider various different boundary conditions. The analytical results are used in the interpretation of the numerical solutions presented in § 2.4. In order to get a physical picture of the solution, we consider the upward propagation of a wave, excited from below at z=0, in an isothermal atmosphere. It is well known that acoustic modes are easily reflected if the temperature of the medium changes with height (for a good discussion see Leibacher and Stein 1981). The slow mode can be reflected due to the increasing Alfvén speed with height from layers where $v_A \sim c_S$, through conversion into a fast mode (*e.g.* Zhugzhda 1984). We implicitly assume that the properties of the atmosphere change abruptly at the top boundary, resulting in downward reflection of the waves. The lower boundary condition is chosen to simulate a forcing layer. This permits standing wave solutions. It should, however, be kept in mind that an isothermal atmosphere by itself does not trap modes, rather we use this assumption to understand the physical properties of the modes in a stratified atmosphere with a vertical field. Let us now derive approximate dispersion relations for various boundary conditions.

2.3.1 Rigid boundaries

We first consider the case of rigid boundary conditions

$$\xi_x = \xi_z = 0 \quad \text{at} \quad z = 0 \quad \text{and} \quad z = d, \tag{2.24}$$

here d is the height of the top boundary boundary, and $D = d/H$ is the dimensionless height.

The asymptotic form of the general solution in the limit of a weak field is presented in Appendix B. Substituting equations (2.24) into equations (B16) and (B27) yields the following dispersion relation (for details of the derivation see Appendix B & HC)

$$(\Omega^2 - K^2)\sin\tilde{\theta}\sin(K_z D) = 2\frac{\epsilon}{\Omega}e^{D/4}\Big\{K_z K^2[\cosh(D/4)\cos\tilde{\theta}\cos(K_z D) - 1]$$
$$+ \sinh(D/4)\cos\tilde{\theta}\sin(K_z D)[M(\Omega^2 - K^2) - K^2(\frac{1}{\gamma} - \frac{1}{2})]\Big\} + O(\frac{\epsilon^2}{\Omega^2}), \tag{2.25}$$

where K_z^2 is given by

$$K_z^2 = \Omega^2 - K^2(1 - \frac{\Omega_{\rm BV}^2}{\Omega^2}) - \frac{1}{4}\,; \tag{2.26}$$

furthermore

$$M = K^2 \frac{\Omega_{\rm BV}^2}{\Omega^2} - \frac{1}{16} , \tag{2.27}$$

$$\theta_0 = \theta(0) , \quad \theta_D = \theta(D) , \qquad \tilde{\theta} = 2(\theta_0 - \theta_D) . \tag{2.28}$$

The solutions of this dispersion relation has been discussed in detail in HC. Next we will use another set of boundary conditions.

2.3.2 Zero-gradient boundary conditions

We now consider the case of zero-gradient boundary conditions at the top and bottom of the layer,

$$\frac{{\rm d}\xi_x}{{\rm d}z} = \frac{{\rm d}\xi_z}{{\rm d}z} = 0 \quad \text{at} \quad z = 0 \quad \text{and} \quad z = d . \tag{2.29}$$

Substituting equations (B44) and (B45) into equation (2.29) yields the following dispersion relation (for details of the derivation see Appendix B and HC)

$$\begin{aligned}
&(K_z^2 + \frac{1}{4})(\Omega^2 - K^2) \sin\tilde{\theta} \sin(K_z D) = \\
&\quad 2(K_z^2 + \frac{1}{4}) \frac{\epsilon}{\Omega} {\rm e}^{D/4} \Big\{ K_z K^3 [\cosh(D/4) \cos\tilde{\theta} \cos(K_z D) - \cosh(D/2)] \\
&\quad + \sinh(D/4) \cos\tilde{\theta} \sin(K_z D) [(M + \frac{1}{4})(\Omega^2 - K^2) - K^3 (\frac{1}{\gamma} - \frac{1}{2})] \Big\} \\
&\quad + \; O(\frac{\epsilon^2}{\Omega^2}),
\end{aligned} \tag{2.30}$$

In Appendix B, the coefficient of the second-order term is also provided.

2.3.2.1 The separate solutions

For $\epsilon \ll \Omega$, the dispersion relation, to lowest order in ϵ/Ω, becomes

$$(K_z^2 + \frac{1}{4})(\Omega^2 - K^2) \sin\tilde{\theta} \sin(K_z D) = 0 . \tag{2.31}$$

Equation (2.31) leads to the following separate dispersion relations:

$$\sin(K_z D) = 0 , \tag{2.32}$$

$$\Omega = K , \tag{2.33}$$

$$\sin\tilde{\theta} = 0 , \tag{2.34}$$

$$K_z^2 + \frac{1}{4} = 0 . \tag{2.35}$$

We first consider the solution given by equation (2.32) which implies that $K_z D = n\pi$, where n is an integer and denotes the order of the mode. Using equation (2.26) yields the usual relation for $p-$ and $g-$modes:

$$\Omega_i^4 - \Omega_i^2(K_t^2 + \frac{1}{4}) + K^2\Omega_{BV}^2 = 0 \qquad (i = p, g), \tag{2.36}$$

where $K_t^2 = K_x^2 + K^2$.

The solution corresponding to equation (2.33) can easily be recognized as the Lamb wave in an unmagnetized atmosphere (Lamb 1932). We denote its frequency by Ω_L. This is simply a horizontally-propagating sound wave, which is evanescent in the vertical direction. Strictly speaking, the Lamb solution is not a normal mode of the atmosphere in the absence of a magnetic field, since it does not satisfy the boundary conditions (2.29). However, in the presence of a weak field, this can be achieved through a slight coupling with the magnetic modes.

The solution given by equations (2.34), represent the modes, which arise solely due to the presence of the magnetic field. The magnetic modes, hereafter referred to as $m-$modes, have frequencies

$$\Omega_m = \frac{\epsilon l \pi}{2s}, \qquad (l = 1, 2, \ldots)\,, \tag{2.37}$$

where $s = (1 - \mathrm{e}^{-D/2})$. These modes are approximately transverse, since it can be shown from equations (B16) and (B27) that

$$\frac{\xi_x^{(1,2)}}{\xi_z^{(1,2)}} \sim O(\theta)\,. \tag{2.38}$$

Physically, these modes can be interpreted as gravity-modified slow modes in a weak magnetic field.

Now we turn our attention to the solution of equation (2.35) which is a new feature of the present analysis. Using equations (2.26) and (2.35) we get

$$\Omega^4 - \Omega^2 K^2 + K^2\Omega_{\mathrm{BV}}^2 = 0\,. \tag{2.39}$$

This equation has the solution

$$\Omega^2 = \frac{1}{2}K^2\left[1 \pm \left(1 - 4\frac{\Omega_{\mathrm{BV}}^2}{K^2}\right)^{1/2}\right]\,; \tag{2.40}$$

thus a real frequency is found only for $K \geq 2\Omega_{\rm BV}$. The solution resembles a gravity mode on the lower branch and a Lamb mode on the upper branch. In order to see this, consider the limit $K \to \infty$. The smaller solution in equation (2.40) has the limit $\Omega \simeq \Omega_{\rm BV}$, which is the dispersion relation for a $g-$mode for large K; the larger solution has the limit $\Omega \simeq K$ for large K, which shows that the mode behaves like a pure Lamb wave. Therefore the mode will henceforth be referred to as a *gravity-Lamb* (or $gL-$) mode. More details about the properties of this mode and its interaction with other modes in the $K - \Omega$ diagram will be considered in §2.5. This mode was not found in HC, where rigid boundary conditions were used. It exists even in a non-magnetic atmosphere, as can easily be seen by looking at the solution for the vertical displacement, which is

$$\xi_z = {\rm e}^{z/2H}[A\sin(K_z Z) + B\cos(K_z Z)] \,, \tag{2.41}$$

where A and B are constants. If we apply the boundary conditions (2.29) we get the exact dispersion relation

$$(K_z^2 + \frac{1}{4})\sin(K_z D) = 0 \,, \tag{2.42}$$

yielding again equation (2.35). From equation (A15), we find that in the presence of a weak magnetic field the dispersion relation for this mode is not modified, at least to $O(\epsilon^2)$. In fact, as we shall see in §2.6, this mode is present even when there is a strong magnetic field, though with a modified dispersion relation.

The frequencies of the magnetic $m-$modes (eq. [2.37]) are independent of K, whereas the frequencies of the Lamb mode increase linearly with K. The $p-$ and $g-$mode frequencies, as determined by equations (2.32) and (2.34), also increase with K; thus it is evident that for some value of K the $p-$, $g-$ and Lamb mode frequencies will cross the pure $m-$mode frequencies. However, in the vicinity of such a crossing point the right-hand side of equation (2.30) can no longer be neglected. It has the effect of turning the crossing of the frequencies into *avoided crossings*, as was also discussed in HC. In the following sections we consider the behavior in the vicinity of such avoided crossings.

2.3.2.2 Avoided crossings between the Lamb mode and the m–modes

We first consider crossings between the Lamb mode and the magnetic modes. In the vicinity of the unmodified Lamb mode, with $\Omega = K$, K_z becomes imaginary. Hence in equation (2.30) we replace K_z by $\tilde{K}_z = |K_z|$, $\sin(\tilde{K}_z D)$ by $\sinh(\tilde{K}_z D)$ and $\cos(K_z D)$ by $\cosh(\tilde{K}_z D)$. Crossing of the pure modes occurs at $K = K_l = \Omega_m$, where Ω_m is given by equation (2.37); at this point equation (2.26) shows that $\tilde{K}_z = 1/\gamma - 1/2$. To analyze the behavior of the full dispersion relation (2.30) around this point, we let

$$K = K_l + \delta K, \qquad \Omega = \Omega_m + \delta\Omega\,, \tag{2.43}$$

where δK and $\delta\Omega$ are regarded as small quantities. We expand $\tilde{\theta}$ to obtain $\tilde{\theta} = l\pi + 2s/\epsilon\,\delta\Omega$. Replacing $\tilde{K}_z$ and the right-hand side by the values at the crossing, we obtain the approximate dispersion relation

$$\begin{aligned}
(-1)^l \frac{4s}{\epsilon}(\Omega_m \delta\Omega - K_l \delta K)\delta\Omega \sinh[(\frac{1}{\gamma} - \frac{1}{2})D] = \\
2\frac{\epsilon}{\Omega_m} e^{D/4}\Big\{(\frac{1}{\gamma} - \frac{1}{2})K_l^3\Big[(-1)^l \cosh(D/4)\cosh[(\frac{1}{\gamma} - \frac{1}{2})D] - \cosh(D/2)\Big] \\
-(-1)^l \sinh(D/4)\sinh[(\frac{1}{\gamma} - \frac{1}{2})D]K_l^3(\frac{1}{\gamma} - \frac{1}{2})\Big\} \\
= (-1)^l \frac{2\epsilon}{\Omega_m} e^{D/4}(\frac{1}{\gamma} - \frac{1}{2})K_l^3\Big\{\cosh[(\frac{3}{4} - \frac{1}{\gamma})D] - (-1)^l \cosh(D/2)\Big\}\,,
\end{aligned} \tag{2.44}$$

or

$$\begin{aligned}
(\delta\Omega^2 - \delta K \delta\Omega)\sinh[(\frac{1}{\gamma} - \frac{1}{2})D] = \\
= \frac{\epsilon^2}{2s} e^{D/4}(\frac{1}{\gamma} - \frac{1}{2})K_l\Big\{\cosh[(\frac{3}{4} - \frac{1}{\gamma})D] - (-1)^l \cosh(D/2)\Big\}\,.
\end{aligned} \tag{2.45}$$

This gives a quadratic equation for $\delta\Omega$, which may be written as

$$\delta\Omega^2 - \delta K \delta\Omega - \frac{1}{4}\delta\Omega_{\min}^2 = 0\,, \tag{2.46}$$

with the solution

$$\delta\Omega = \frac{1}{2}\delta K \pm \frac{1}{2}(\delta K^2 + \delta\Omega_{\min}^2)^{1/2}\,. \tag{2.47}$$

Here

$$\delta\Omega_{\min}^2 = 16\frac{\eta^2}{\pi^2} K_l \frac{\sinh(D/4)}{\sinh[(\frac{1}{\gamma} - \frac{1}{2})D]}(\frac{1}{\gamma} - \frac{1}{2})\Big\{\cosh[(\frac{3}{4} - \frac{1}{\gamma})D] - (-1)^l \cosh(D/2)\Big\}\,, \tag{2.48}$$

where $\eta = \epsilon\pi/2s$ is the separation between the frequencies of adjacent magnetic modes.

In the case of rigid boundaries (HC) a similar expression was found, where $\delta\Omega^2_{\rm min}$ was non-negative for all values of l (see eq. [46] of HC); hence in that case the roots were always real. In contrast, for the solution given by equations (2.47) and (2.48) $\delta\Omega^2_{\rm min}$ is negative for even l. Hence, in the present case of vanishing gradients of the displacements at the boundaries, we obtain pairs of complex conjugate roots for even values of l when K is within the range $\pm|\delta\Omega_{\rm min}|$ of the location of the crossing of the pure modes. The consequences of this for the global behavior of the eigenfrequencies are discussed in §2.4, based on numerical solutions of the oscillation equations.

We now consider the minimum frequency separation $\delta\Omega^{(+)}_{\rm min}/\eta$ in an avoided crossing between the Lamb mode and a magnetic mode of odd l, shown in Figure 2.2 as a function of K for different D. Unlike the zero-displacement case (see Figure 4*b* of HC) one finds that in this case the minimum separation depends on K. Clearly, values of $\delta\Omega^{(+)}_{\rm min}/\eta$ exceeding unity indicate a breakdown of the asymptotic description and this occurs at smaller values of K in the case of zero-gradient boundaries. The dashed lines similarly show $|\delta\Omega^{(-)}_{\rm min}/\eta|$ for even l, corresponding to the range in K around the avoided crossing for which there are complex conjugate roots; thus $2|\delta\Omega^{(-)}_{\rm min}|$ gives the minimum separation in K between the eigen-curves at such an avoided crossing.

2.3.2.3 Avoided crossings between $p-$ or $g-$modes and $m-$modes

We now consider a crossing between a $p-$ or $g-$mode of order n, characterized by $K_z D = n\pi$, and a magnetic mode of order l with frequency $\Omega_m = \epsilon\pi l/2s$. We know from equation (2.26) that the crossing will take place at the point (K_{nl}, Ω_m) in the (K, Ω) diagram where

$$\frac{n^2\pi^2}{D^2} = \Omega_m^2 - K_{nl}^2\left(1 - \frac{\Omega^2_{\rm BV}}{\Omega_m^2}\right) - \frac{1}{4}\,. \tag{2.49}$$

As before, we let

$$K = K_{nl} + \delta K, \qquad \Omega = \Omega_m + \delta\Omega\,. \tag{2.50}$$

Expanding K_z we obtain

$$K_z \simeq \frac{n\pi}{D} - \frac{DK_{nl}}{n\pi}\left(1 - \frac{\Omega^2_{\rm BV}}{\Omega_m^2}\right)\delta K + \frac{D\Omega_m}{n\pi}\left(1 - K_{nl}^2\frac{\Omega^2_{\rm BV}}{\Omega_m^4}\right)\delta\Omega\,. \tag{2.51}$$

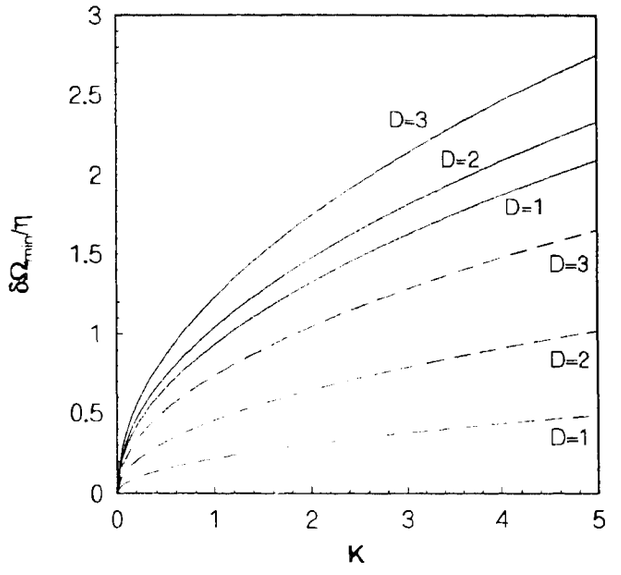

Figure 2.2: Asymptotic values for the minimum separation $\delta\Omega_{\min}$, in units of η, between adjacent avoided crossings between the Lamb mode and magnetic modes, as a function of K, for $\epsilon = 0.01$ and $\gamma = 5/3$. The solid lines show $\delta\Omega^{(+)}_{\min}/\eta$ for $D = 1, 2, 3$ for odd values of l, whereas the dashed lines show $|\delta\Omega^{(-)}_{\min}/\eta|$ for even l, for the same values of D.

The expansion of $\tilde{\theta}$ was already given in §2.3.1.2. We substitute these expansions into the left-hand side of equation (2.30), while the right-hand side and the factor $\Omega^2 - K^2$ are evaluated at (K_{nl}, Ω_m). This leads to

$$(-1)^{n+l}\frac{2s}{\epsilon}(\Omega_m^2 - K_{nl}^2)\frac{D^2}{n\pi}\left[\left(1 - K_{nl}^2\frac{\Omega_{\rm BV}^2}{\Omega_m^4}\right)\Omega_m\delta\Omega - \left(1 - \frac{\Omega_{\rm BV}^2}{\Omega_m^2}\right)K_{nl}\delta K\right]\delta\Omega$$
$$= \frac{\epsilon}{\Omega_m}e^{D/4}\frac{2n\pi}{D}K_{nl}^3\left[(-1)^{n+l}\cosh(D/4) - \cosh(D/2)\right] , \quad (2.52)$$

which can be further simplified to

$$\delta\Omega^2 - \frac{K_{nl}\Omega_m(\Omega_m^2 - \Omega_{\rm BV}^2)}{\Omega_m^4 - K_{nl}^2\Omega_{\rm BV}^2}\delta K\delta\Omega - \frac{\epsilon^2\pi^2n^2}{D^3s}\frac{K_{nl}^3[\cosh(D/4) - (-1)^{n+l}\cosh(D/2)]}{(\Omega_m^2 - K_{nl}^2)(\Omega_m^4 - K_{nl}^2\Omega_{\rm BV}^2)} = 0 . \quad (2.53)$$

Equation (2.53) provides a quadratic equation for $\delta\Omega$ as a function of δK. For $\delta K = 0$, the minimum separation between two branches can be obtained from equation (2.53) as

$$\delta\Omega_{\min}^2 = \frac{4s\eta^2n^2}{D^3}\frac{K_{nl}^3[\cosh(D/4) - (-1)^{n+l}\cosh(D/2)]}{(\Omega_m^2 - K_{nl}^2)(\Omega_m^4 - K_{nl}^2\Omega_{\rm BV}^2)} . \quad (2.54)$$

The behavior near the avoided crossing depends crucially on $n+l$. When $n+l$ is odd we obtain a normal avoided crossing in Ω. On the other hand, $\delta\Omega^2_{\rm min}$ is negative for even $n+l$, so that real solutions are again absent near the avoided crossings. We also note that $\delta\Omega_{\rm min}$ increases with K approximately as $K_{nl}^{3/2}$, *i.e.*, more rapidly than for the avoided crossings between the Lamb mode and the magnetic modes (*cf.*. Eq. [2.48]).

2.3.2.4 Avoided crossings with the gravity-Lamb mode

According to equation (B50), $K_z^2+1/4$ is a factor to all terms in the dispersion relation, upto and including the term of order ϵ^2. Thus, to this order, there is exact crossing between the $gL-$mode and the remaining modes, and an analysis similar to the one carried out in §§2.3.1.2 and 2.3.1.3 is not possible. In §2.5.1 we show, from numerical computations, that the actual behavior in the vicinity of the crossing points do indeed lead to avoided crossings with regions in K with no real solutions, the minimum separation scaling roughly as ϵ^2. This suggests that the exact factorization ceases to hold in the term of order ϵ^3 in equation (B50).

2.3.3 Mixed boundary conditions

To analyze the effects of boundary conditions on various elementary wave modes, we have chosen different combinations of conditions on the displacements at the boundaries. Specifically, we now examine the behavior of the normal modes for the following boundary conditions:

$$\xi_x = \xi_z = 0 \quad \text{at} \quad z = 0\,, \tag{2.55}$$

and

$$\frac{\mathrm{d}\xi_x}{\mathrm{d}z} = \frac{\mathrm{d}\xi_z}{\mathrm{d}z} = 0 \quad \text{at} \quad z = d\,. \tag{2.56}$$

This choice corresponds to a node at the base and an anti-node at the top boundary. As before, the asymptotic dispersion relation can be obtained by substituting equations (B16) and (B27) into equation (2.55) and equations (B44) and (B45) into equation (2.56); here we consider only the lowest-order terms, obtaining

$$[\sin(K_z D) + 2K_z\cos(K_z D)](\Omega^2 - K^2)\cos\tilde{\theta} = 0\,. \tag{2.57}$$

As before, to this order the dispersion relation has separated solutions. We obtain the following separate dispersion relations:

$$K_z + \frac{1}{2}\tan(K_z D) = 0 \,, \tag{2.58}$$

$$\Omega = K \,, \tag{2.59}$$

$$\cos\tilde{\theta} = 0 \,. \tag{2.60}$$

The solutions of equations (2.59) and (2.60) correspond to the Lamb and magnetic modes, discussed earlier. The Lamb mode is unaffected by the change in boundary conditions, while for the magnetic modes the frequencies are given by

$$\Omega_m = \frac{\epsilon\pi}{2s}(l + \frac{1}{2}) \,, \qquad (l = 0, 1, 2, \ldots) \,; \tag{2.61}$$

thus they are shifted by an amount $\epsilon\pi/4s$ in the diagnostic diagram with respect to the $m-$modes calculated for the previous sets of boundary conditions treated in §3.1 and in HC. However, the frequency separation between adjacent modes is the same as before.

We now return to the solution of equation (2.58), which represents the modified form of the $p-$ and $g-$mode dispersion relation. In fact, by applying the boundary conditions (2.55)-(2.56) to the solution ξ_z for an isothermal non-magnetic atmosphere given by equation (2.41), we get the exact dispersion relation

$$\sin(K_z D) + 2K_z\cos(K_z D) = 0 \,, \tag{2.62}$$

which is identical to equation (2.58). For large mode order n the solution can be approximated as

$$K_z D \simeq \left(n + \frac{1}{2}\right)\pi \,. \tag{2.63}$$

This expansion yields the usual $p-$ and $g-$modes with a frequency shift, as compared to HC and the previous case (§2.3.1), due to the additional term of $\pi/2$ on the right hand side of equation (2.63).

The general result of this analysis is therefore that the overall frequency spectrum of the $p-$/ $g-$modes, magnetic modes and the Lamb mode for a magnetic atmosphere (apart from a possible constant frequency shift) is insensitive to the precise nature of the boundary conditions.

We have also considered the normal modes for yet another set of boundary conditions, namely

$$\xi_x = \xi_z = 0 \quad \text{at} \quad z = d\,, \tag{2.64}$$

and

$$\frac{\mathrm{d}\xi_x}{\mathrm{d}z} = \frac{\mathrm{d}\xi_z}{\mathrm{d}z} = 0 \quad \text{at} \quad z = 0\,. \tag{2.65}$$

The results are the same as for the above case, because of symmetry. One can check this easily by using equation (2.41) for an isothermal non-magnetic atmosphere.

In principle the coupling between the separate solutions at points where they cross could be analyzed by including the term $O(\epsilon)$ in the dispersion relation (2.57). However, as discussed in § 2.4.3 below we have found that the behavior of the numerical results deviates strongly from the resulting expression. We shall not pursue this further here.

2.4 $K - \Omega$ Diagram for a weak field

We now consider numerical results for the weak-field case. The solutions were computed by solving equation (2.23) (formulated as a system of first-order differential equations) with a fourth-order Newton-Raphson-Kantorovich scheme (Cash and Moore 1980) which was used also in HC. We first consider the case of using the zero-gradient boundary conditions in equations (2.29). Figure 2.3*a* depicts the resulting variation of frequency with horizontal wave number, for $\epsilon = 0.01$, $\gamma = 5/3$ and $D = 1$ (this is used as the default case unless otherwise specified). The long dashed line corresponds to the Lamb solution $\Omega = K$ and the short dashed lines correspond to the gravity modes g_1, g_2 in a non-magnetic atmosphere. The solid and dotted lines, respectively, correspond to the numerical solution of equation (2.23) and the roots of the analytical dispersion relation (B50). The default choice $D = 1$ for the vertical extent of the cavity may appear to be somewhat idealized and not relevant to photospheric flux tubes. This choice is basically made to allow us to use the asymptotic analysis for a weak field over the entire extent of the atmosphere. The asymptotic analysis proves to be an extremely valuable tool for understanding the modal structure and permits us to understand the numerical results much better. By gradually increasing D, it is possible to see how the modal structure is modified and also to classify the modes.

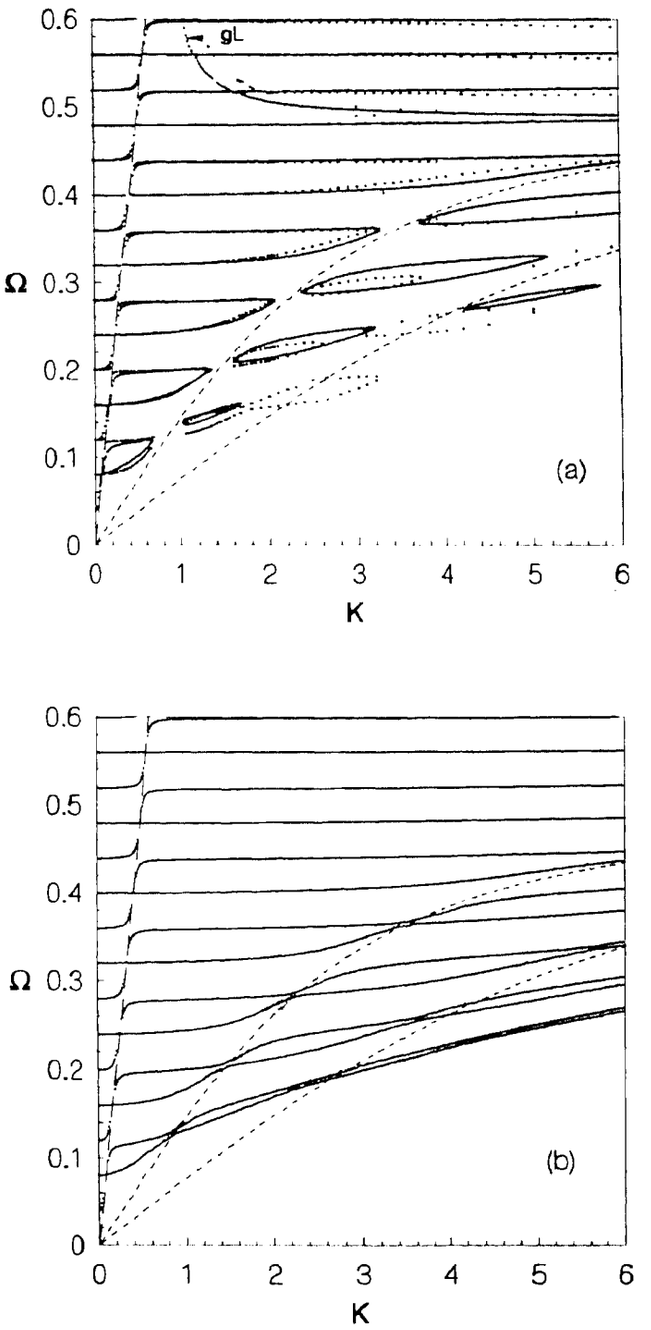

Figure 2.3: Variation of Ω with K in an isothermal atmosphere using the default values $\epsilon = 0.01$, $D = 1$ and $\gamma = 5/3$. The long-dashed curve represent the Lamb solution $\Omega = K$ and the short-dashed curves correspond to the g_1- and g_2-modes in a non-magnetic atmosphere. (*a*) Results for zero-gradient boundary conditions; the solid lines correspond to the numerical solution of equation (2.23) and the dotted lines to the solution of the dispersion relation (B50). (*b*) Results for rigid boundary conditions; solid lines correspond to the numerical solution of equation (2.23).

We first compare the numerical results with those obtained by solving the analytical dispersion relation (B50). For small values of K (roughly when $K < 1$), the agreement between the two sets of curves is very good. However, as K increases the two sets of solutions begin to differ, with the largest discrepancy for small values of Ω. The reason for this behavior has already been discussed in HC: it is essentially due to the breakdown of the asymptotic expansion for large K, such that $K^2 > \Omega^3 v_A/c_S$.

It is interesting to compare the results shown in Figure 2.3*a* with those obtained in HC using rigid boundary conditions. The latter are shown in Figure 2.3*b*. The most important qualitative difference between the two sets of calculations is in the appearance of the gravity-Lamb mode, labeled gL. This mode corresponds to the solution of equation (2.35). The remaining solutions for $\Omega < 0.6$ (the region shown in Figures 2.3*a* and 2.3*b*) consist of magnetic or $m-$modes, which interact with the Lamb mode (for $\Omega \simeq K$) or with the $g-$modes when equation (2.32) is satisfied; as pointed out in HC the frequency is restricted to be above the frequency of the m_1-mode.

Comparison of Figures 2.3*a* and 2.3*b* show that with the exception of the $gL-$mode the solutions are very similar for the two sets of boundary conditions apart from the vicinity of the avoided crossings. We now turn to an analysis of these, based on the asymptotic results obtained in §2.3. The interactions between the $gL-$mode and the remaining modes are discussed in §2.5.

2.4.1 Avoided crossings between the Lamb mode and the $m-$modes

Figure 2.4 shows an enlargement of a portion of Figure 2.3*a*, showing the interaction of the lowest-order $m-$modes with the Lamb mode. These modes have been labeled m_l ($l = 1, 2, \ldots$). The Lamb mode frequency, as mentioned above, tends to zero for $K = 0$. However, for finite K the Lamb mode frequency crosses those of the magnetic modes.

To investigate the resulting behavior, we focus first on the m_1 mode; as K increases, it begins to acquire the character of a magnetic Lamb mode with $\Omega \simeq K$. The m_2 mode, on the other hand, with frequency larger than that of the Lamb mode, behaves as a pure magnetic mode, with no dependence on K. As K increases further, the frequencies of

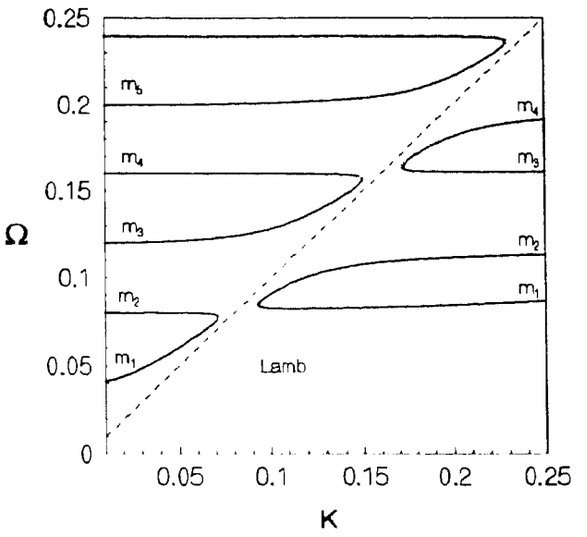

Figure 2.4: Variation of Ω with K in an isothermal atmosphere using the default values $\epsilon = 0.01$, $D = 1$ and $\gamma = 5/3$. The short-dashed curve represent the Lamb solution $\Omega = K$, and the solid line correspond to the numerical solution of equation (2.23) with zero-gradient boundary conditions. The magnetic modes have been labeled as m_l ($l = 1, 2, \ldots$).

the two modes approach closely. The modes corresponding to even-order $m-$modes do not have real solutions near the intersection points. On the other hand, as an odd $m-$mode approaches the $\Omega = K$ curve it acquires the character of a Lamb mode and avoids crossing it by merging with the next higher-order even mode. Thus the odd- and even-order magnetic modes behave differently as they approach the $\Omega = K$ curve; this is in accordance with the asymptotic expressions (2.47) and (2.48). The odd $m-$modes undergo a mode transformation to a Lamb mode, but since there is no real solution for the even-ordered $m-$modes near the avoided crossings, they cannot cross the intersection point and as a result merge with the modified Lamb mode. These merged modes reappear at some distance away from the avoided crossing and separate out as two independent magnetic modes. Physically, at the avoided crossing there is a strong coupling between the two modes, and the character of the solution is a mixture of a pure magnetic-like and a pure Lamb-like mode.

Thus, the asymptotic analysis explains the difference in the connectivity of the eigen-curves near the avoided crossings for even and odd values of l. Note that this result is entirely different from the case of rigid boundaries (considered in HC), where $\delta\Omega_{\rm min}$

is always real for all values of l. Consequently, in that case, for all l the nature of the solutions near the intersection points follows the pattern of the odd solutions found for zero-gradient boundary conditions.

2.4.2 Avoided crossings between the $m-$modes and the $g-$ and $p-$modes

Figure 2.5*a* shows the interaction between $g-$ and $m-$modes, assuming default values of the parameters. We first consider the m_1-mode. As K increases this mode acquires the character of a g_1-mode. In accordance with the asymptotic description in equation (2.54), the nature of the solution near the intersection point, similar to the previous section, is one where this mode merges with m_2. To the right of the intersection point, there are two branches: the lower branch is a modified m_2-mode whereas the upper one is a modified g_1-mode. The latter undergoes an avoided crossing with the magnetic mode m_3, but this time the interaction is different due to the fact that we have an odd $m-$mode. This phenomenon is repeated when the next odd magnetic mode (m_3), which behaves like a gravity mode, approaches the m_4-mode. Regarding the two branches on the right of the intersection point, we find that they merge again, possibly due to the influence of the g_2-mode.

At higher values of K the validity of the asymptotic expressions is dubious. However, the qualitative nature of the avoided crossings is similar, leading to the formation of extended "islands" in the $K-\Omega$ diagram (cf. Figure 2.3*a*). The location of these islands coincides closely with the almost parallel eigen-curves found in the case of zero-displacement boundary conditions (see Figure 2.3*b*).

The interaction between the p_1-mode and higher-order magnetic modes is depicted in Figure 2.5*b*. The first avoided crossing (in the lower half of Fig. 4*b*) between the p_1-mode and an odd-order mode (labeled as m_o) leads to a merger in accordance with equation (2.54), since $n+l$ is even. When these two modes reappear away from the intersection point, they separate into an $m-$mode and a p_1-mode. When the p_1-mode comes closer to the next even-order $m-$mode it undergoes a mode transformation in the form of an ordinary avoided crossing, the p_1- and the $m-$mode exchanging character. Furthermore, the alternation between the narrow (in K) and wide (in Ω)

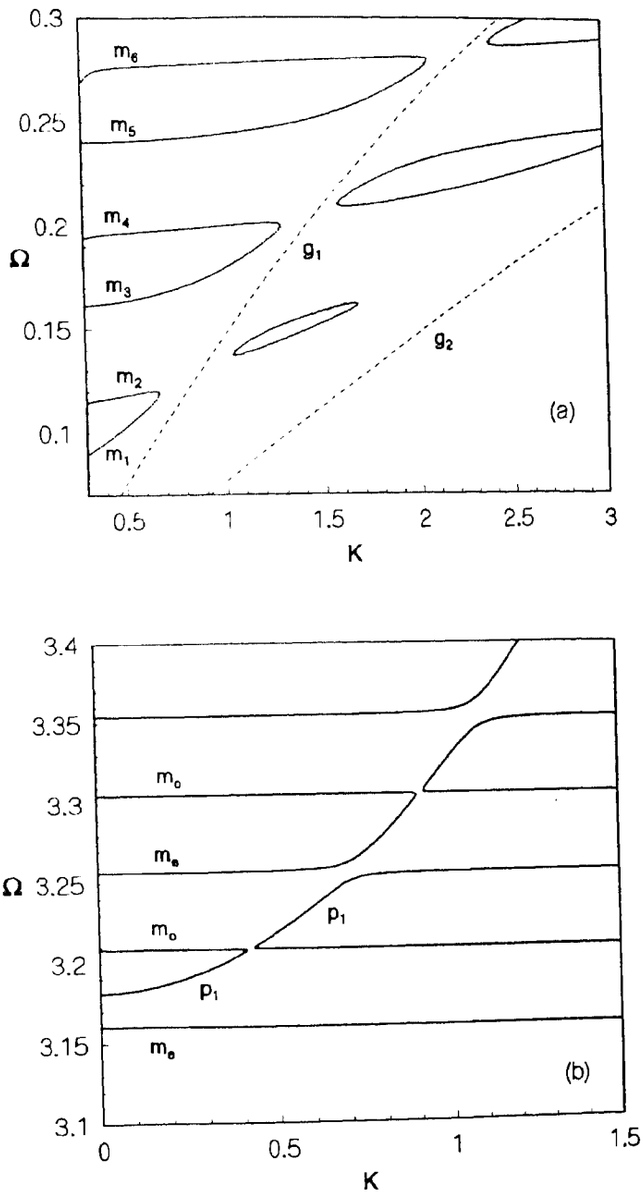

Figure 2.5: Expanded regions of the diagnostic diagram for the default parameters. The solid lines show numerical solutions using zero-gradient boundary conditions. (*a*) Region of interaction between $g-$ and $m-$type solutions. The solid curves correspond to the magnetic modes and have been labeled as m_l (l =1,2, ...), and the dashed curves (labeled as g_1, g_2) show frequencies of $g-$modes in the field-free case. (*b*) Region of interaction between $p-$ and $m-$type solutions. The odd- and even-ordered magnetic modes are denoted as m_o and m_e, respectively. The $m-$modes have orders between 80 and 83.

separations for even and odd $n + l$ is evident here. Thus the asymptotic analysis enables us to understand the alternate behavior of the magnetic modes, which leads to merging of nearest-neighbor eigen-curves around an avoided crossing accompanied by mode transformation.

2.4.3 Mixed boundary conditions

Figure 2.6*a* shows a $K - \Omega$ diagram for mixed boundary conditions (eqs [2.55]-[2.56]), using the default parameters. The solid lines show the numerically computed frequencies for this case, whereas the long-dashed and short-dashed lines show the Lamb mode and the lowest-order $g-$modes, respectively. A closer inspection reveals that the frequencies of the magnetic modes have in fact been shifted by half the frequency separation, as predicted by equation (2.61). However, the most striking difference from the previous cases is in the behavior at the avoided crossings: although formally these are topologically equivalent to those in Figure 2.3*b*, alternating between avoidance in Ω and avoidance in K, the separation is now so large as to leave an extended mode-free region surrounding the location of the Lamb-mode, with similar regions surrounding the low-order $g-$modes. This behavior is particularly striking in Figure 2.6*b*, which shows the region of low K for $\epsilon = 0.002$, but otherwise using the default parameters. Here the density of magnetic modes is so high that the regions of avoidance are clearly delineated. We have found from numerical solutions that these regions are essentially independent of the value of ϵ, for small ϵ. This behavior is qualitatively different from what is obtained for zero-displacement or zero-gradient boundary conditions. In particular, we note from equations (2.48) and (2.54) that in the latter case $|\delta\Omega_{\rm min}| \propto \epsilon$ at a given point (K, Ω) in the diagnostic diagram. However, for mixed boundary conditions it appears that the minimum separation at avoided crossings is much larger than the separation between adjacent magnetic modes, thus invalidating the simple asymptotic description. We hope to return to this point in a future publication.

We have also computed numerical solutions for the boundary conditions (2.64) and (2.65). As argued in § 2.3.2 the separate solutions are the same as in the case considered in Figure 5; however, the behavior at the avoided crossings is even more extreme, leading to an apparent near suppression of the modes to the right of the Lamb line $\Omega = K$ at

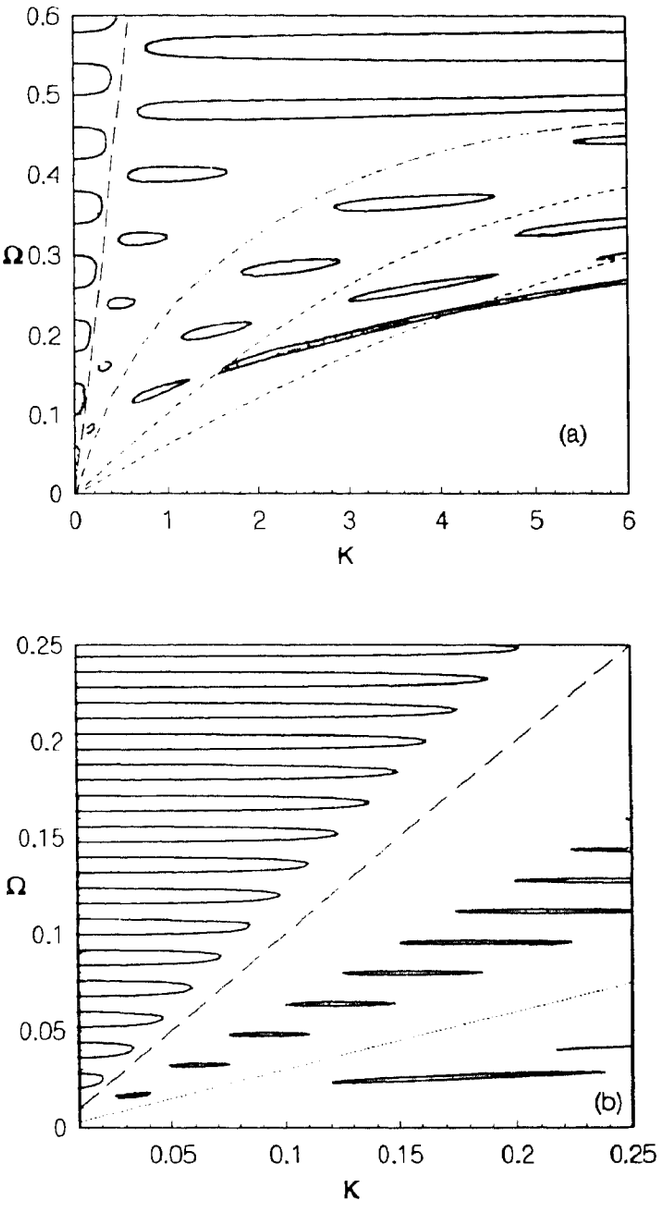

Figure 2.6: Variation of Ω with K in an isothermal atmosphere using the default values $D = 1$ and $\gamma = 5/3$, and the mixed boundary conditions (2.55)- (2.56). The long-dashed curve represent the Lamb solution $\Omega = K$ and the short-dashed curves correspond to the g_1- , g_2- and g_3-modes in a non-magnetic atmosphere. The following values of ϵ are shown: *(a)* $\epsilon = 0.01$; *(b)* $\epsilon = 0.002$.

frequencies below $\Omega \simeq 0.5$. This case deserves closer scrutiny.

2.5 Properties Of The Gravity-Lamb Mode

The gravity-Lamb mode is a new feature of the solution for the zero-gradient boundary conditions. Its interactions with the other modes lead to a number of intricate phenomena, some of which are apparently related to the fact that more than two modes may be involved in a given interaction. Here we examine these interactions in some detail.

2.5.1 Avoided crossings between the gravity-Lamb mode and the magnetic modes

The asymptotic analysis in § 2.3.1 left some uncertainty about the interaction between the $gL-$ and the $m-$modes in the weak-field limit. To investigate this interaction by means of numerical calculations, Figure 2.7 shows results for avoided crossings near $\Omega = 0.8$, for $D = 1$, $\gamma = 5/3$, and $\epsilon = 0.01, 0.02, 0.05$ and 0.1. It is evident that the crossings are indeed avoided, leaving regions in K corresponding to complex solutions for Ω. Also, the minimum separation $\delta K_{\min}$ in K is extremely small for small ϵ: the numerical results can be approximated quite accurately by $\delta K_{\min} \simeq 4.5\epsilon^2$. On the scale of Figure 2.3 this behavior is evidently invisible.

2.5.2 Effect of the gravity-Lamb mode on avoided crossings between pure Lamb and magnetic modes

Figure 2.7 illustrates the interaction between a magnetic mode and what might be considered the pure gravity-Lamb mode. However, the frequency separation between the latter and the ordinary Lamb mode is comparable with, or smaller than, the separation in the avoided crossing for $\epsilon = 0.1$. This suggests that all three modes must be taken into account when studying the interaction. We have not attempted an asymptotic analysis of this very complex case; however, the numerical results provide an indication of the phenomena that it gives rise to. As a reference, we first briefly recall the behavior observed in HC for rigid boundary conditions. Figure 2.8*a* shows the avoided crossings between the Lamb mode and magnetic modes for $\epsilon = 0.1$. In the limit $K \to 0$, we denote the magnetic modes m_l ($l = 1, 2, \ldots$). The Lamb mode is represented by the

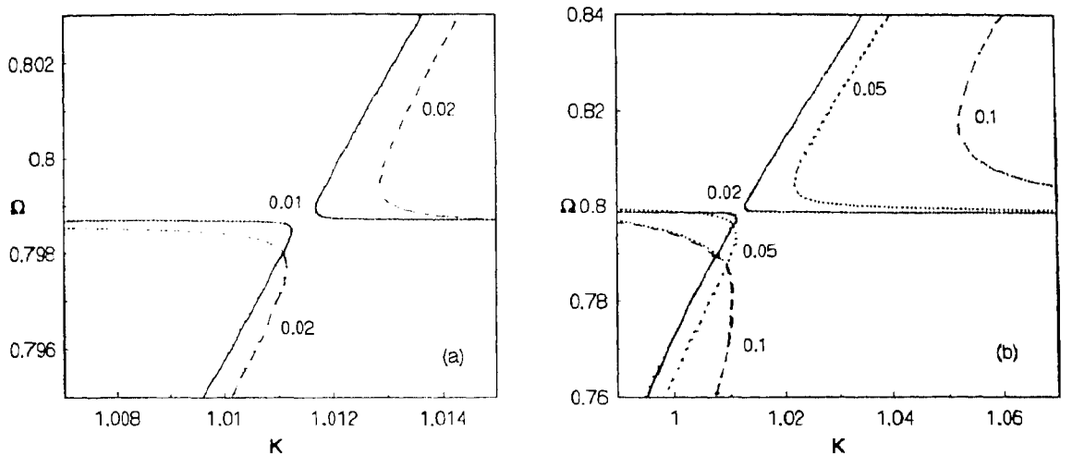

Figure 2.7: Avoided crossings between the gravity-Lamb mode and a magnetic mode, using the zero-gradient boundary conditions (2.29), for $D = 1$, $\gamma = 5/3$, and different values of ϵ, as indicated in the figure. In panel (*a*) the solid line is for $\epsilon = 0.01$ and the dashed line for $\epsilon = 0.02$. In panel (*b*) the solid line is for $\epsilon = 0.02$, the dotted line for $\epsilon = 0.05$ and the dashed line for $\epsilon = 0.1$.

dashed line. The main feature, which has already been pointed out in HC, is that successive magnetic modes undergo avoided crossings due to one of the modes becoming transformed into a Lamb mode, which then undergoes avoided crossings with the next higher-order magnetic mode. This behavior can now be compared with Figure 2.8*b*, for zero-gradient boundary conditions (2.29), but otherwise using the same parameters as for Figure 2.8*a*. In the limit $K \to 0$, and for K substantially higher than the value corresponding to the Lamb mode, the frequencies of the magnetic modes appear at approximately the same locations in the diagnostic diagram as in Figure 2.8*a*. However, in Figure 2.8*b* we note the appearance of the gravity-Lamb mode. Also, the mode coupling is much more complicated than before. This can be illustrated by considering in some detail the interactions near the intersection point marked by a cross in Figure 2.8*b*. As K increases, the m_1−mode begins to acquire the character of a magnetic Lamb mode as before, but as it approaches the intersection point, the two magnetic modes join up. This is equivalent to the behavior observed in Figure 2.4 for smaller ϵ. However, in the present case the magnetic modes emerging to the right of the intersection immediately encounter the gravity-Lamb mode. This leads to a new pair of avoided crossings, the

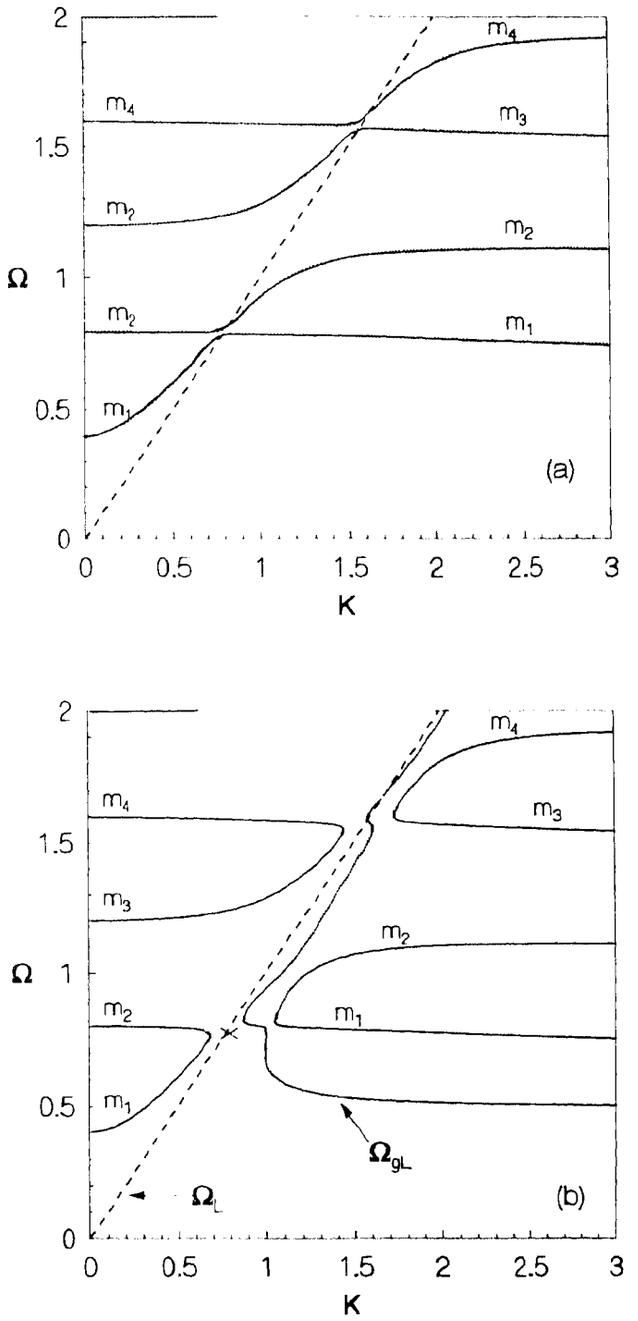

Figure 2.8: Region in the diagnostic diagram, for $\epsilon = 0.1$, where there are magnetic and Lamb-type solutions. The dashed curve corresponds to the pure Lamb solution $\Omega = K$. (*a*) Results for zero-displacement boundary conditions; the solid curves show magnetic modes with orders 1 to 4. (*b*) Results for zero-gradient boundary conditions; the pure Lamb mode ($\Omega = K$) has been shown with a dashed line, and the gravity-Lamb mode frequency (given by equation 15) has been labeled as Ω_{gL}, whereas the other solid curves correspond to the magnetic modes of order 1 to 4.

lower of which was shown in more detail in Figure 2.7*a*. Only after this additional interaction does the pair of magnetic modes emerge and continues towards higher K. The same pattern of behavior is repeated near the subsequent intersection points, such as the m_3-, m_4-modes also shown in Figure 2.8*b*; however, here the separation between the Lamb and the gravity-Lamb modes is so small that the two sets of avoided crossings almost merge.

Another interesting feature of this analysis concerns the lowest possible frequency of the normal modes, for a weak field. In HC, we found that this is given by the m_1-mode. However, in the present case the lower cutoff is given by the smaller of the m_1 and the gravity-Lamb mode frequencies. This behavior persists even as we increase the strength of the magnetic field, as can be seen in Figures 8*a-d*, where we present the $K-\Omega$ diagram for $\epsilon = 0.15$, 0.20, 0.25 and 0.30. The short-dashed and dotted lines depict the pure Lamb and $gL-$modes respectively. With increasing ϵ, the frequencies of the magnetic modes increase, but the $gL-$mode is unmodified with frequency $\Omega \to \Omega_{BV}$ for large K.

2.5.3 Avoided crossings between $p-$modes, magnetic modes and the gravity-Lamb mode

The situation becomes further complicated when interactions involving the $p-$modes are considered. This is also illustrated in Figures 2.9*a-d*, where the long-dashed line shows the p_1-mode in the non-magnetic case. With increasing ϵ the frequencies of the magnetic modes shift past the $p-$mode frequencies, leading to shifting patterns of avoided crossings. Particularly striking is the formation of "islands" of modes which drift towards higher K; this is visible, for example, in going from panel (*c*) to panel (*d*) in Figure 2.9. Also, the connectivity of the eigen-curves changes. This is illustrated in more detail in Figure 2.10, corresponding to values of ϵ intermediate between those for panels (*a*) and (*b*) in Figure 2.9. It is evident that there are values of ϵ where an actual crossing of the curves take place, leading to degeneracy in the eigen-spectrum. Although we have not analyzed this behavior further, it appears to be linked to the interaction, even though fairly distant, with the p_1-mode. The development of the $K-\Omega$ diagram for somewhat stronger field, corresponding to $\epsilon = 0.5$, is illustrated in Figure 2.11. Here

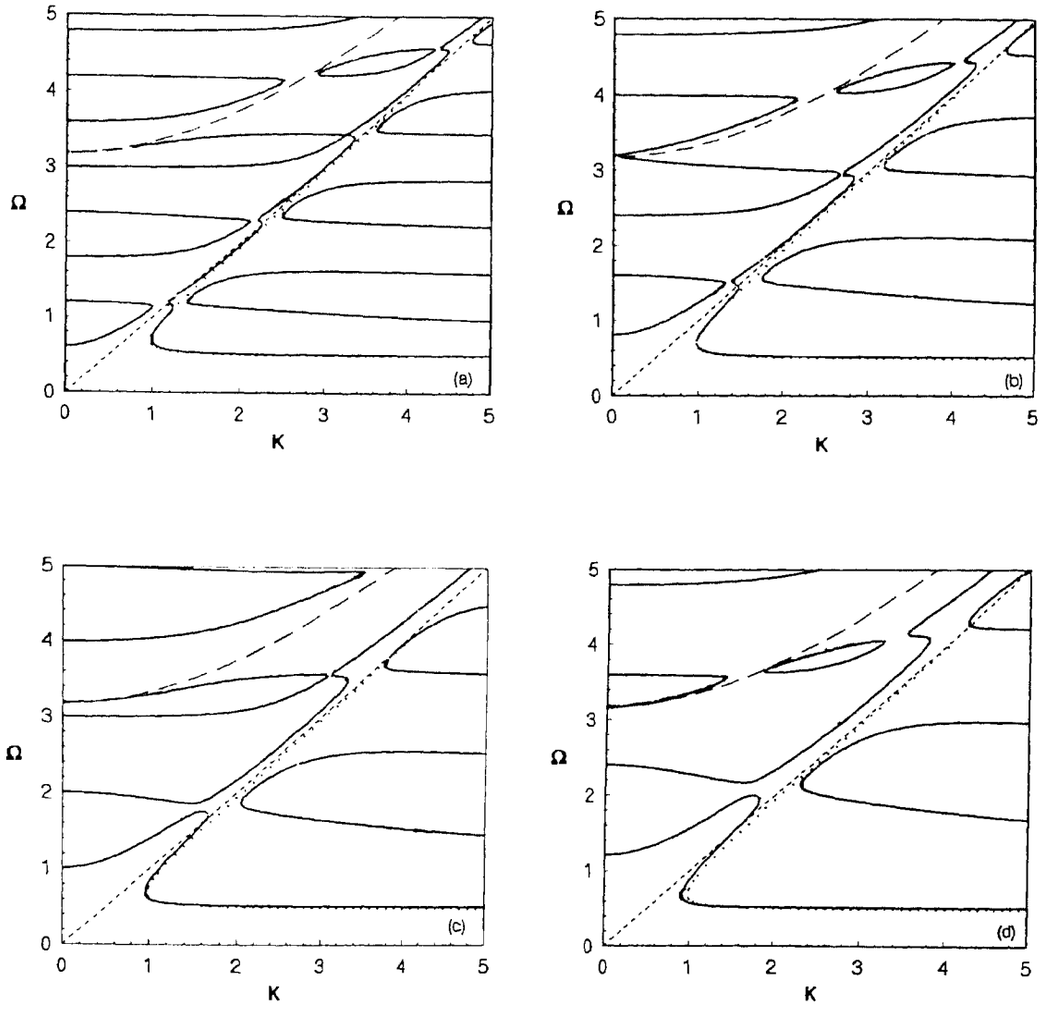

Figure 2.9: The evolution of the $K - \Omega$ diagram with increasing ϵ, for $D = 1$, $\gamma = 5/3$ and zero-gradient boundary conditions. The following values of ϵ are shown: (*a*) $\epsilon = 0.15$; (*b*) $\epsilon = 0.20$; (*c*) $\epsilon = 0.25$; (*d*) $\epsilon = 0.30$. The pure Lamb mode ($\Omega = K$) has been shown with a short dashed line, the pure gravity-Lamb mode frequency (given by equation 2.39) by a dotted line, and the pure p_1−mode by a long dashed line.

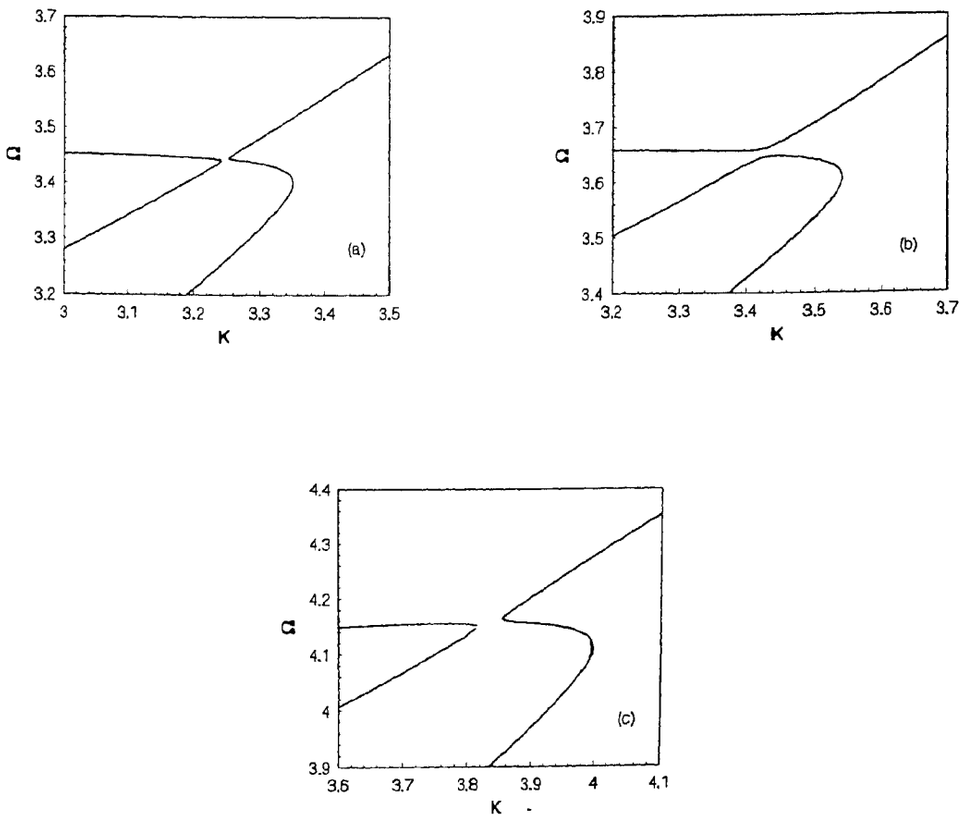

Figure 2.10: Details of the changes in the connectivity of the $K - \Omega$ diagram with ϵ, for $D = 1$, $\gamma = 5/3$ and zero-gradient boundary conditions. The following values of ϵ are shown: (a) $\epsilon = 0.15$; (b) $\epsilon = 0.16$; (c) $\epsilon = 0.185$.

the dashed curves correspond to the zero-displacement boundary conditions of HC and the continuous lines represent the zero-gradient boundary conditions. In the latter case the lowest two magnetic modes m_1 and m_2, the lowest p–mode p_1 and the gravity-Lamb mode are present. The behavior of the mode coupling is drastically different in the two cases. In the zero-displacement case, the avoided crossing occurs through the interaction of a Lamb-modified magnetic mode with a p–mode, which results in a conversion of a modified m_1–mode to a p_1–mode and vice versa. On the other hand, for the zero-gradient boundary conditions the gravity-Lamb mode merges with the m_1– and the p_1–modes, in a manner similar to Figure 2.9. In fact, near the avoided crossing

the coupling is here between three different modes, namely the p_1-, the modified m_1- and the gravity-Lamb mode; thus the coupling cannot be explained in terms of the two-mode coupling analyzed so far. To the right of the intersection points we find, similar to the behavior in Figure 2.9, the appearance of the m_1 and p_1 branches. At higher K, the behavior is similar to that found for rigid boundary conditions.

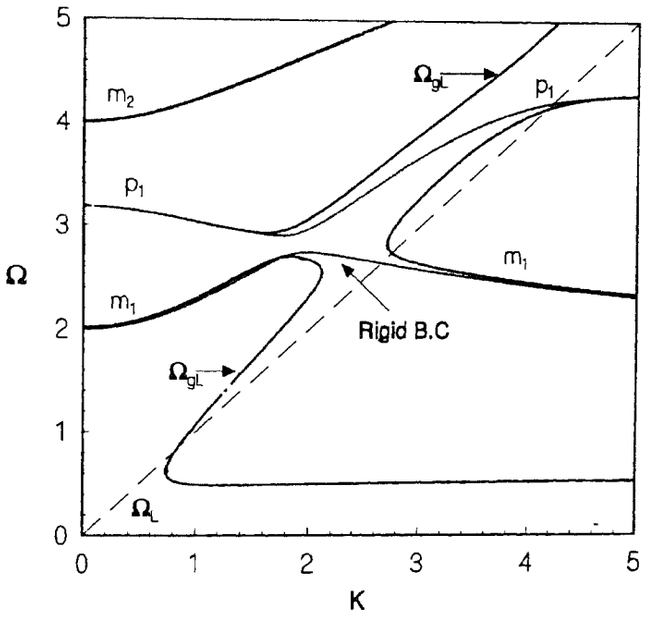

Figure 2.11: Details of avoided crossings in the diagnostic diagram between the p_1-mode, magnetic modes and Lamb mode for $\epsilon = 0.5$, corresponding to moderate field strength. The solid curves are for the zero-gradient boundary conditions and dashed curve are for the rigid boundaries used in HC.

Another interesting feature of the results, visible in Figures 2.9 and 2.11, is that as ϵ increases the $gL-$mode starts crossing the $\Omega = K$ line. In this region of the diagram, the mode begins to feel the increasing effects of the magnetic field and its classification as a $gL-$mode is not fully appropriate: thus the validity of equation (2.39) is questionable. However, on the basis of a local treatment it appears that the appropriate generalization of equation (2.39) is

$$\Omega^4 - (\epsilon^2 + 1)K^2\Omega^2 + \Omega_{\rm BV}^2 K^2 = 0\,. \tag{2.66}$$

This expression is taken from the analysis by Nagakawa *et al.* (1973) for trapped magnetoatmospheric waves, based on the use of a WKB approximation. Nagakawa *et al.* examined the domain of trapped magnetoatmospheric waves, and obtained equation (2.66) for of one of their boundary curves. Moreover, their $K-\Omega$ diagram shows this branch. The main concern of these authors was to find out the domains of trapped waves, but they did not identify the branch corresponding to equation (2.66) as a gravity-Lamb mode (or more accurately a magneto-gravity Lamb mode) for moderate to strong fields. From equation (2.66) we find that asymptotically, in the limit of large K, $\Omega \simeq (1+\epsilon^2)^{1/2}K$ on the upper branch of this mode, and for the lower branch, that $\Omega \simeq \Omega_{\rm BV}/(1+\epsilon^2)^{1/2}$. The quantitative agreement of this asymptotic behavior with the numerical results is discussed in the next section.

2.6 $K-\Omega$ Diagram For Strong Fields

We now consider an isothermal atmosphere extending over several scale heights for which $v_A \gg c_s$ over most of the atmosphere. This situation is somewhat similar to the atmosphere in a sunspot. We first classify the elementary wave modes present in such an atmosphere for zero-gradient boundary conditions and examine their behavior in the diagnostic diagram. Our main emphasis will be on the properties of the gravity-Lamb mode in a strong field.

2.6.1 Modes in the strong-field case

Figures 2.12*a*,*b* show the diagnostic diagram corresponding to $D=5.0, \epsilon=0.8$, and $D=10.0, \epsilon=0.5$. The solid lines were obtained by solving equation (2.23) numerically. We first consider the solution for small K. There are two families of solutions, which correspond to slow magnetoacoustic modes or $p-$like modes with frequencies given by

$$\Omega_{p,n} = \sqrt{\frac{n^2\pi^2}{D^2}+\frac{1}{4}}\,, \tag{2.67}$$

and fast magnetoacoustic modes or $n-$modes with frequencies approximately given by (Scheuer & Thomas 1981)

$$\Omega_{m,l} = \sqrt{\frac{\epsilon^2}{4}j_{2K,l}^2+K^2}\,, \tag{2.68}$$

where $j_{2K,l}$ denotes the l-th zero of J_{2K}. equations (2.67) and (2.68) are used to classify the modes close to $K = 0$ in the diagnostic diagram. Note that, unlike the weak-field case, the $p-$mode frequencies are essentially independent of K: the $p-$modes are indicated by the nearly horizontal dotted curves in the diagnostic diagram. Equation (2.68) suggests that $m-$mode eigen-curves, indicated by dashed curves in the diagnostic diagram, are nearly parabolic.

Unlike HC, where the p_1-mode provided a cutoff for the lowest possible frequency of the system for this set of parameters, we also find the presence of the $gL-$mode below this cut-off for large magnetic field. The avoided crossings around the $K = \Omega$ line in Figures 2.12*a*,*b* are due to the interaction between the $gL-$mode and $p-$modes. In Figure 2.12*a* the $gL-$mode crosses the $\Omega = K$ line because of the strong magnetic field (cf. the discussion following eq. [2.66]), and when it comes close to the p_1-mode it merges with it. The dot-dashed curve represents the solution of equation (2.66); it is interesting to note that the asymptotic limits are in quantitative agreement with the numerical results. Because of the strong magnetic field effect the pure $gL-$mode modifies into a magneto gravity-Lamb mode or $MgL-$mode. The $MgL-$mode reappears away from the avoided crossing and the same behavior is repeated. On the other hand the m_1-mode and p_3-mode undergo a mode transformation in the usual way.

Magnetoatmospheric waves for strong magnetic field were studied by Abdelatif (1990). To compare the results of the two analyses, we concentrate on Figure 2.12*b*, which can be compared with Figure 3 of Abdelatif (1990). One easily identifies the $gL-$mode near the $\Omega = K$ line; in fact, equation (2.68) shows that there are no $m-$modes in that part of the diagnostic diagram. Abdelatif did not recognize the presence of the $MgL-$mode and moreover he did not interpret correctly the interaction of this branch with the $p-$modes. The avoided crossings in other parts of Figure 2.12*b* can be explained in terms of interaction between $p-$modes and $m-$modes in the usual way.

2.6.2 Umbral oscillations

It is well known from observations, that oscillations in sunspot umbrae typically have periods in the range $\sim$ 2 to 3 mins. The lower layers of the umbral atmosphere are

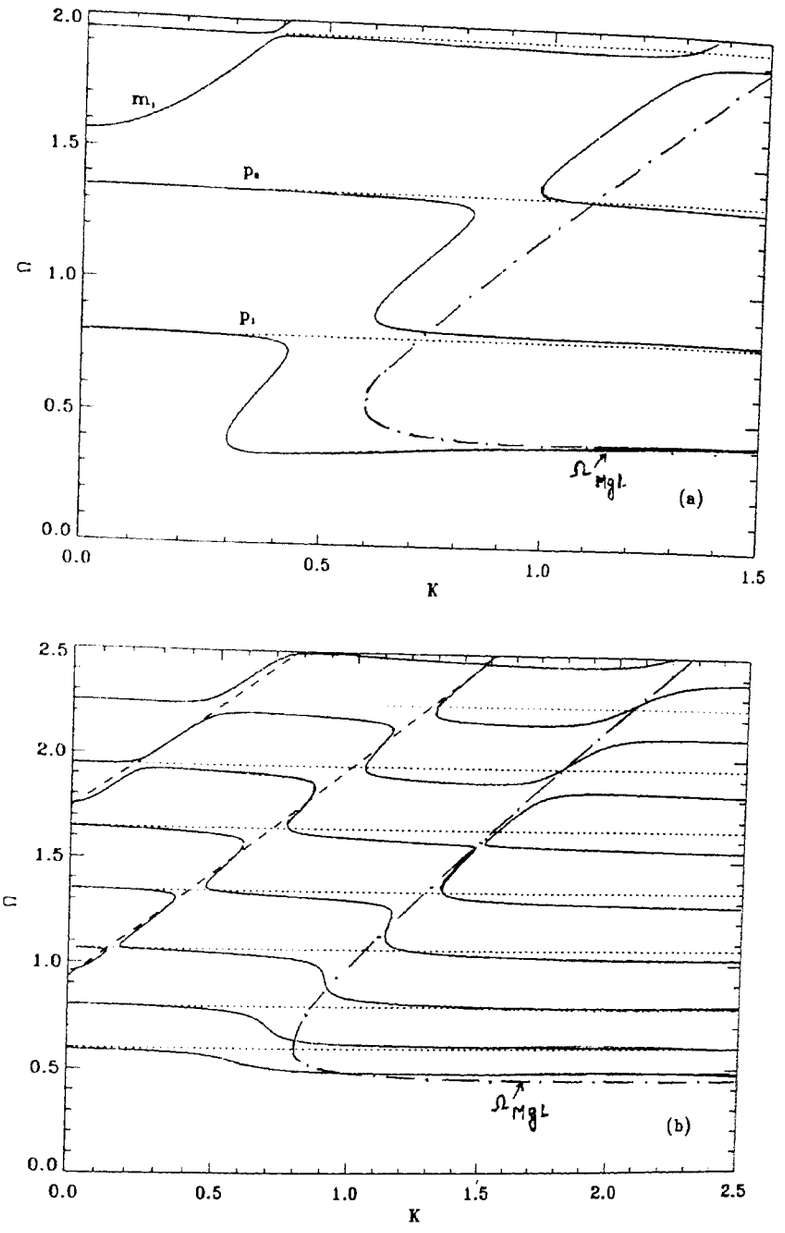

Figure 2.12: Variation of Ω with K in an isothermal atmosphere for the strong-magnetic field case. The classification of the modes into $p-$ and $m-$type refers to the solutions of equations (2.67) and (2.68), respectively, for $K = 0$. The dotted curves represent the $p-$type solutions and the dashed curves represent the $m-$type solutions. The magneto-gravity-Lamb mode (corresponding to the solution of equation [2.66]) is represented by the dot-dashed line labeled as Ω_{MgL}. Panel (a) is for $D = 5.0, \epsilon = 0.8$ and (b) for $D = 10, \epsilon = 0.5$.

found to have maximum power in the five minute range while the chromosphere and transition region have periods in the range 120 to 200 secs.

Our results on the $MgL-$mode may be applied to oscillations in the atmosphere of a sunspot umbra, which we idealize as an isothermal layer of vertical extension $D = 20$. For c_s=6.5 km/s (corresponding to a scale height of 100 km), the upper boundary is at a height of 2000 km, which roughly corresponds to the chromosphere in a sunspot. The sharp increase in temperature in these layers provides a natural reflection for the modes. Fig. 2.13 shows the $MgL-$mode in the $K - \Omega$ diagram for various values of ϵ or the field strength B, which are used to label the curves. We do not show the $p-$modes in the figure, as their spectrum is essentially the same as that shown in Fig. 10 of HC. The curves depicted in Fig. 2.13 closely follow the dispersion relation given by

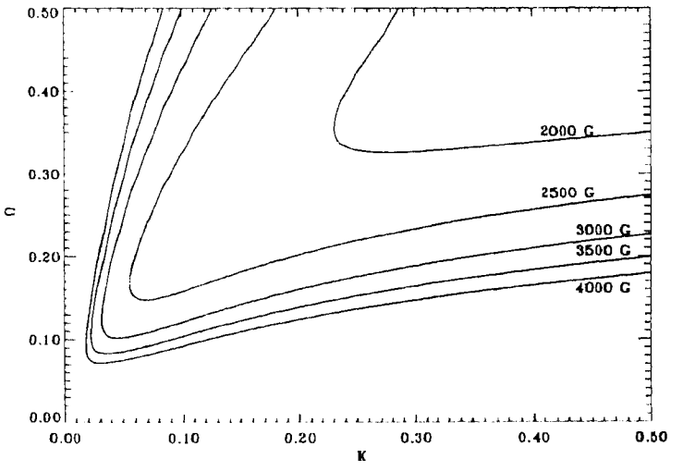

Figure 2.13: Region in the diagnostic diagram, for $D = 20$ and different field strengths, as labeled. Only the $MgL-$mode is present.

equation (2.66). An interesting point to note here is that with increasing magnetic field strength, the $MgL-$ mode resembles more of a magnetic mode than a pure $gL-$mode. We now determine the eigenfrequencies of the $MgL-$mode for a typical umbral radius in the range 3000 to 5000 km and magnetic field between 2000 G and 4000 G. Table 2.1 presents the eigenfrequencies of the $MgL-$mode obtained from our model atmosphere with $D = 20$. Following Scheuer and Thomas (1981) let us treat the sunspot umbra as a cylinder of radius a. It can easily be shown that our analysis for a plane can be carried over in a straightforward way to cylindrical geometry, by treating axisymmetric

modes and regarding ξ_x and k as the radial displacement and wave number respectively. Assuming that the radial component of the displacement vanishes at $r = a$, we find that k takes discrete values given by $ka = j_{1,\nu}$, where $j_{1,\nu}$ denotes the zero of the Bessel function J_1 of order ν. We consider the lowest-order mode (where order refers to the horizontal direction) corresponding to ν=1. This provides us with a relation between the horizontal wave number and radius of the spot.

a (km)	B (G)	ω (s^{-1})	P (s)
3000.....	2500	0.0228	275
	3000	0.0317	198
3500.....	2500	0.0212	297
	3000	0.0298	211
	3500	0.0343	183
4000.....	2500	0.0198	317
	3000	0.0278	226
	3500	0.0324	194
5000.....	2500	0.0145	432
	3000	0.0224	280
	3500	0.0267	235
	4000	0.0298	211
6000.....	3000	0.0209	301
	3500	0.0250	251
	4000	0.0293	214
7000.....	3000	0.0172	365
	3500	0.0208	302
	4000	0.0234	268

Table 2.1: Eigenfrequencies of the MgL−mode for different radii and magnetic field strength of a sunspot umbra.

We thus see that for field strengths and radii typical for sunspots, the MgL−mode has periods in the observed range. It should also be noted that the lowest-order fast magnetoacoustic mode or m_1−mode appears at $\Omega = 0.8$ which corresponds to a period of 119 s. Though our model atmosphere is somewhat idealized we show that the MgL−mode might be relevant to umbral oscillations.

2.7 Discussion

The present analysis has revealed many interesting features regarding wave propagation in a stratified media. As in HC, we have largely concentrated our analysis on the weak-field limit ($v_A/c_s = \epsilon \ll 1$) and extended the previous calculations to different types of boundary conditions. For $v_A/c_s \ll 1$, the character of the waves can be analyzed in terms of elementary modes of a non-magnetic atmosphere and pure magnetic modes. Our analysis confirms the result found in HC that, to lowest order in ϵ, the magnetic Lamb mode is also a solution. As noted in HC, the Lamb mode is not a mode of a non-magnetic atmosphere, since it does not satisfy the boundary conditions. However, this becomes possible in the presence of a magnetic field, through a slight coupling with the magnetic modes via the boundary conditions.

Our treatment of the weak-field limit has permitted an analysis of the $K-\Omega$ diagram in terms of asymptotic approximations; this has allowed us to understand the nature of the modes in a vertical magnetic field. The insight so gained has proved useful in extending the computations to the moderate- to strong-field case.

A new feature of the present analysis is the occurrence of an additional mode. For larger K, this mode has one branch merging with Ω_{BV} and a second branch which is close to the pure Lamb mode; this leads us to refer to it as a gravity-Lamb mode (see Fig. 7*b*). It is striking that the gravity-Lamb mode is also a solution in a non-magnetic atmosphere for zero-gradient boundaries. In the asymptotic description the mode arises from a factor $K_z^2 + 1/4$ in the dispersion relation (B50) which seems to persist to fairly high asymptotic order. We do not find the presence of this mode for other sets of boundary conditions used in HC and in this study as well. The main emphasis of this work has been on the properties of this mode. We have extended our analysis to moderate to strong fields also and find that the gravity-Lamb mode becomes modified as a magneto-gravity-Lamb mode. Due to the influence of the strong magnetic field it crosses the pure Lamb mode and merges with the magnetic modes (Figures 2.39 and 2.11). The identification and interaction of this mode with other modes does not appear to have been carried out earlier, despite the fact that it appears in the local analysis of Nagakawa *et al.* (1973). However, the results of a local analysis, which do not take into account boundary conditions, should be viewed with caution (Thomas

1982). Our results based on a rigorous approach confirm that the gL–mode is present in the special case of vanishing gradient boundary conditions, but not for all sets of boundary conditions.

Another aspect of the results regards the influence of the magnetic field on the dense spectrum of g–like modes. The analysis of HC revealed that the entire low frequency spectrum of g–modes below the frequency of the m_1–mode is effectively eliminated by the magnetic field. As the magnetic field increases, the lower threshold frequency can become larger than the Brunt-Väisälä frequency for rigid boundary conditions. In this case, we find that it is the Brunt-Väisälä frequency which provides the lower cutoff. Thus, even when the magnetic field becomes large, there is always a gravity-like mode present at large K.

The present calculations also demonstrate that when the same reflecting boundary conditions are used at the top and the bottom of the layer the overall nature of the frequency spectrum, at least for weak fields, is insensitive to the precise form of the boundary conditions, away from the avoided crossings; an exception is the gL–mode which exists only when the gradients vanish at both boundaries. However, the qualitative nature of mode interaction close to the intersection point can be sensitive to the boundary conditions. This feature appears to hold even for strong fields. The use of mixed boundary conditions (zero displacement on one boundary and zero gradients on the other) introduces a frequency shift in the $m-$, $p-$ and g–modes corresponding approximately to half the frequency separation between adjacent modes.

The change of the boundary conditions has a striking effect on the connectivity of the eigen-curves at avoided crossings, relative to the results obtained in HC with zero-displacement conditions. This was already noticeable in the results of Abdelatif (1990). The zero-displacement boundary conditions provide real solutions for the frequency Ω at all wavenumbers K; in contrast, calculations with zero-gradient conditions at both or one of the the boundaries lead to complex-conjugate pairs of roots for Ω when K is in the vicinity of some or all of the avoided crossings. In terms of the real solutions, the avoidance happens in K rather than in Ω. This behavior can be understood from asymptotic analysis of the solution near the avoided crossings. A mathematically analogous phenomenon was found by Lee & Saio (1990) in the case of coupling between

stellar pulsation and rotation. It is obvious that one of the complex branches of Ω corresponds to overstable modes. In the case of rotating stars, the growth of the mode results from a transfer of energy from rotation to the pulsation, as noted by Lee & Saio. In the present case, the energy input to the growing mode must presumably occur at the boundaries, but the physical details of this process so far elude us. For mixed boundary conditions the behavior is superficially similar, although the minimum separations in the avoided crossings are substantially larger, leading to extensive regions in the diagnostic diagram where no modes are found.

Oscillations in a realistic stellar atmosphere are affected by radiative dissipation and energy loss at the boundaries. Thus the modes are damped, with complex frequencies. The effects on the topology of the $K - \Omega_r$ diagram (Ω_r being the real part of the frequency) in the vicinity of an avoided crossing depend on the relative magnitude of the damping rates of the two modes involved and the minimum separation in the (undamped) avoided crossing (Christensen-Dalsgaard 1981). If the minimum separation exceeds the difference in damping rates between the modes, Ω_r undergoes an avoided crossing, while the damping rates cross. On the other hand, if the difference in damping rates exceeds the minimum separation, the avoided crossing of the undamped modes is converted to an actual crossing.

It is appropriate to mention that the main thrust of our investigation has been to examine the physics of wave propagation in a stratified atmosphere with a vertical magnetic field. One of our objectives has been to examine the modal structure and see how it is influenced by the field. These studies of modal physics form a useful background for physically more realistic situations. In HC, a specific set of boundary conditions was used to study this problem. We have now extended the previous results to different boundary conditions, and seen how they influence the various modes. We have also demonstrated that the new MgL–mode has periods that fall within those observed in umbral oscillations. In forthcoming investigations, we hope to further enlarge the scope of our analysis to more realistic conditions; especially to consider wave leakage from the boundaries. For polytropic and sunspot atmospheres, this problem has been studied by Cally & Bogdan (1993) and Cally, Bogdan & Zweibel (1994) Following Spruit & Bogdan (1992), slow modes are allowed to drain energy by propagating downwards

through the bottom boundary. This provides an effective method of absorbing energy from external $p-$modes, by the coupling between these modes in layers where the sound and Alfvén speeds are comparable. However, a careful analysis of the effect of the field on the modal structure still needs to be carried out. This we hope to attempt in subsequent study. We expect that study of the present kind of mode physics will also help us in understanding heating in active regions through the process of mode conversion.

Chapter 3

Wave Leakage from Magnetized Atmosphere

3.1 Introduction

The detection of oscillations in magnetic elements has led to the development of several theoretical models to understand their physical nature. Bulk of the work in this area has focussed on oscillations in sunspots, particularly in the umbra where the magnetic field can be regarded as almost vertical. Theoretical models for understanding umbral oscillations in the 3-min band fall into two distinct classes. In the first one, the oscillations are considered to be fast modes trapped in a resonant cavity located in the photospheric layers of the umbra and below (Scheuer and Thomas 1981; Thomas and Scheuer 1982). The other model proposed by Zhugzhda *et al.*(1983, 1984) and Gurman and Leibacher (1984) treats the oscillations as resonantly trapped slow modes within a chromospheric cavity. However, more recent work by Hasan (1991) suggests that both types of cavities may exist simultaneously in the umbral atmosphere. Furthermore, it appears that there may be a strong coupling between the two cavities, especially for modes with horizontal wave numbers that undergo avoided crossings in the $k-\omega$ diagram. This can have many important consequences, particularly as it can lead to a transfer of energy between the cavities.

The purpose of this Chapter is to examine in greater detail the character of MAG waves, particularly in the avoided crossing regions of the $k-\omega$ diagram. We expect that the strong mode coupling of different waves in such regions can have interesting effects, which could be relevant for sunspots and more generally for stratified flux tubes. With

this view in mind, we undertake an exhaustive study of the effects of mode coupling on MAG waves. In the previous Chapter we made a detailed investigation of the nature of MAG oscillations in an isothermal medium. By using the weak field approximation, it was possible to derive an analytic dispersion relation and thereby infer many useful properties of the waves. Assuming the eigenfrequencies to be purely real it was found that, when the vertical gradients of the velocities vanish at one of the boundaries, the avoided crossings in the $k-\omega$ diagram could be characterized by large voids or zones of avoidance. From an analysis of the asymptotic dispersion relation, it was predicted that the eigenfrequencies in these regions become complex. This is certainly an unexpected finding and will be examined further in this Chapter. We shall show that a consequence of this result is that there is a leakage of wave energy out of the cavity, despite the absence of an explicit dissipative mechanism. This leakage of wave energy occurs only at specific locations in the $k-\omega$ diagram.

It is worthwhile to note that similar results have been obtained in other physical systems. For instance a detailed analysis of wave interactions in fluid flows was done by Craik (1988). Using dynamical boundary conditions he derived a dispersion relation which has complex conjugate roots. He attributed the instability in the flow to the exponentially growing mode. Modes with real ω are neutrally stable. Cairns and Lashmore-Davies (1983) proposed an interesting model for mode coupling in inhomogeneous media. They provided a unified theory for a class of mode conversion problem. Here we propose an alternative theory of wave leakage from the photospheric cavity where mode coupling plays a crucial role in determining the frequency spectrum.

The plan of this Chapter is as follows: we begin in §3.2 by briefly recapitulating the form of the $k-\omega$ diagram. This is followed by calculations giving the damping rates of various modes along with eigenfunctions in §3.3. The coupling between different modes are examined by inspecting the changes in the eigenfunctions as they approach an avoided crossing. In §3.4 we present the wave energy equation, which allows us to calculate the time averaged net energy densities and energy flux associated with these wave modes. In §3.5. the properties of the gravity-Lamb mode are examined in detail while looking at their eigenfunctions and different components of energy density. In §3.6 we treat the strong-field case. Finally, a discussion of the results and comparison

with previous studies are taken up in §3.7.

3.2 Solution of Wave Equation in the weak - Magnetic field case

We first consider the case of zero-gradient boundary conditions at the top and bottom of the cavity,

$$\frac{\mathrm{d}\xi_x}{\mathrm{d}z} = \frac{\mathrm{d}\xi_z}{\mathrm{d}z} = 0 \quad \text{at} \quad z = 0 \quad \text{and} \quad z = d\,; \tag{3.1}$$

where d is the height of the cavity. The linearized wave equations for an isothermal

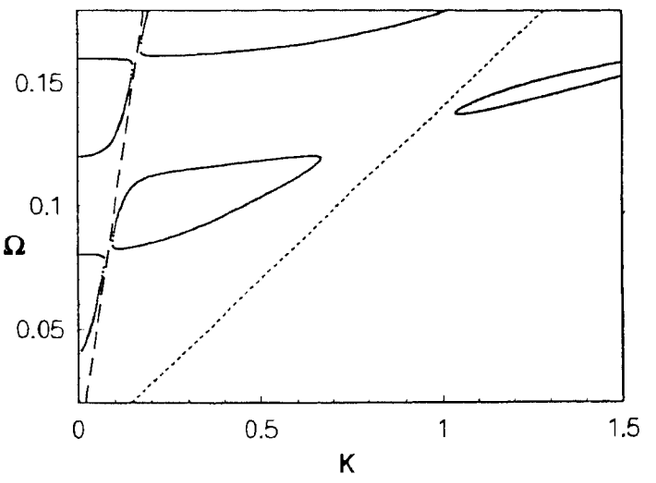

Figure 3.1: Variation of Ω with K using default values $\epsilon = 0.01, D = 1.0, \gamma = 5/3$. The solid lines correspond to the numerical solution of Eq. (2.23) obtained assuming real frequencies. The long dashed curve corresponds to the Lamb solution $\Omega = K$ and the short-dashed curve corresponds to $g-$ mode in a non-magnetic atmosphere.

atmosphere with a vertical magnetic field (Eq. 2.23) were solved numerically, using a complex version of the Newton-Ralphson-Kantorovich scheme with the above boundary conditions, to determine Ω for different values of K. We first compare our results with those of the previous Chapter, in which the eigenfrequencies were assumed to be purely real. Figure 3.1 shows an enlarged view of Figure 2.3 which depicts the variation of the real part of Ω with K, for $D = 1$, $\epsilon = 0.01$ and $\gamma = 5/3$ (henceforth, the default parameters for this Chapter). The dispersion relations for this particular choice of

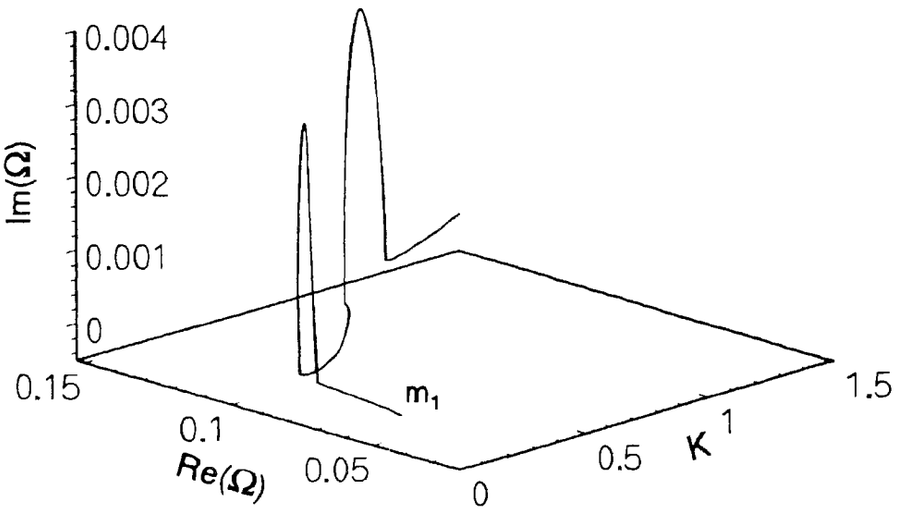

Figure 3.2: Three dimensional view of the diagnostic diagram of the first magnetic mode corresponding to an atmosphere with $\epsilon = 0.01, D = 1.0, \gamma = 5/3$.

boundary condition allows us to identify the different elementary modes (see Eqs. [2.33] – [2.35]). The various solid curves depict magnetic or slow modes m_l- (l denotes order of the mode), the long dashed line corresponds to the Lamb solution $\Omega = K$, and the short dashed line correspond to the lowest order gravity mode g_1- in a nonmagnetic atmosphere. We now focus our attention on the region in the $K - \Omega$ diagram where there are voids. In §2.3.1.2 of Chapter 2, we had pointed out that these regions are physically related to a strong coupling between modes. The nature of the solutions near the vicinity of the intersection point depends upon the boundary conditions. For vanishing gradient boundary conditions, the avoided crossings take on the character of "zones of avoidance" or voids, where the frequencies become complex. For illustration, let us consider a single mode, which we choose as the lowest order magnetic mode m_1-, and follow its behavior as it interacts with the Lamb and gravity modes. Figure 3.2 gives a three dimensional view of the complex diagnostic diagram of the first magnetic mode, where the imaginary part of Ω is plotted along the z-axis. This plot clearly reveals that Ω is complex precisely in the regions of the real $K - \Omega$ diagram where there are voids, whereas elsewhere Ω is purely real. Thus, we see that the gaps in the diagnostic diagram are now filled up by the real part of the complex frequency.

3.3 Eigenfunctions for various wave modes

We now examine the form of the eigenfunctions, *i.e.* the variation of ξ_x and ξ_z with z. To study the nature of coupling we first look at the eigenfunctions of the elementary modes. In order to do that we choose a combination of frequency and wave number in the diagnostic diagram away from the avoided crossing. Then we inspect the changes in the eigenfunctions as they approach an avoided crossing. We will use zero gradient boundary conditions.

3.3.1 Elementary modes

3.3.1.1 Magnetic Lamb mode

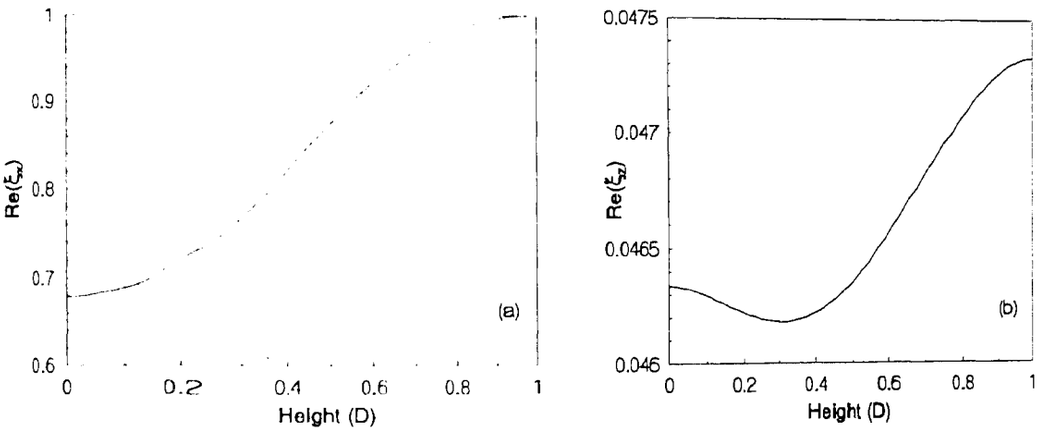

Figure 3.3: The real part of ξ_x (panel a) and ξ_z (panel b) as a function of height for $K = 0.04$ and $\Omega = 0.054$ corresponding to a Lamb-like mode. The normalization is arbitrary.

Let us consider a magnetic Lamb mode with a purely real frequency, given by $\Omega = 0.054$ at $K = 0.04$ (see Fig. 3.1). This mode is simply a horizontally propagating sound wave, which is evanescent in the vertical direction. The eigenfunction of this mode is clearly real. Figure 3.3 shows the variation with height of the horizontal and vertical components of the displacement, *viz.* ξ_x and ξ_z for the above mode. It is seen that $\xi_x \gg \xi_z$, which is a general property of a Lamb mode. Strictly speaking, a pure Lamb mode does not have any vertical component, but this modified Lamb mode acquires a small vertical component due to the influence of the magnetic mode. Also, we find that ξ_x increases monotonically with height, which for small values of z approximately

follows the form for a Lamb wave, given by

$$\xi_x \sim e^{\frac{(\gamma-1)z}{\gamma H}} \tag{3.2}$$

The above equation follows from equation (2.17) with $\xi_z = 0$. At the upper boundary, this form is modified by the effects of the magnetic mode which influences the above behavior through the boundary condition requiring that the gradient of the displacement vanishes.

3.3.1.2 Low-order magnetic mode

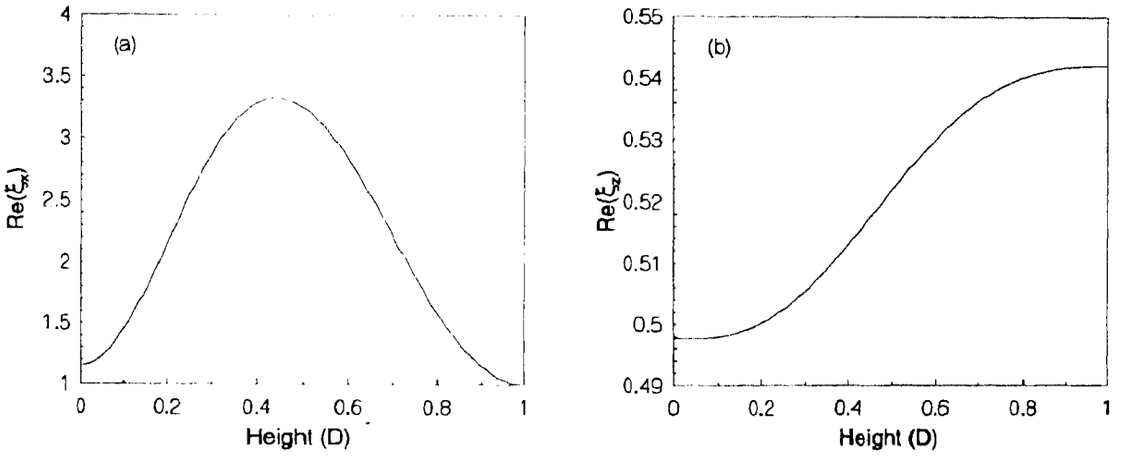

Figure 3.4: The real part of ξ_x (panel a) and ξ_z (panel b) as a function of height for $K = 0.04$ and $\Omega = 0.08$ corresponding to a pure magnetic mode. The normalization is arbitrary.

We now consider the lowest order magnetic mode in the K -Ω diagram, for which $K = 0.04$ and $\Omega = 0.08$ (see Fig. 3.1). Figure 3.4 shows the eigenfunctions as a function of height in the cavity. We find that this mode is approximately transverse since $\xi_x >> \xi_z$, which is consistent with the asymptotic analysis presented in the previous Chapter (see Eq. [2.38]). This mode can be interpreted as a gravity modified slow mode in a weak magnetic field.

3.3.1.3 High-order magnetic mode

We choose a high frequency region of the $K - \Omega$ diagram and follow the behavior of a magnetic mode with high order. Figure 3.5 shows the eigenfunctions as a function of

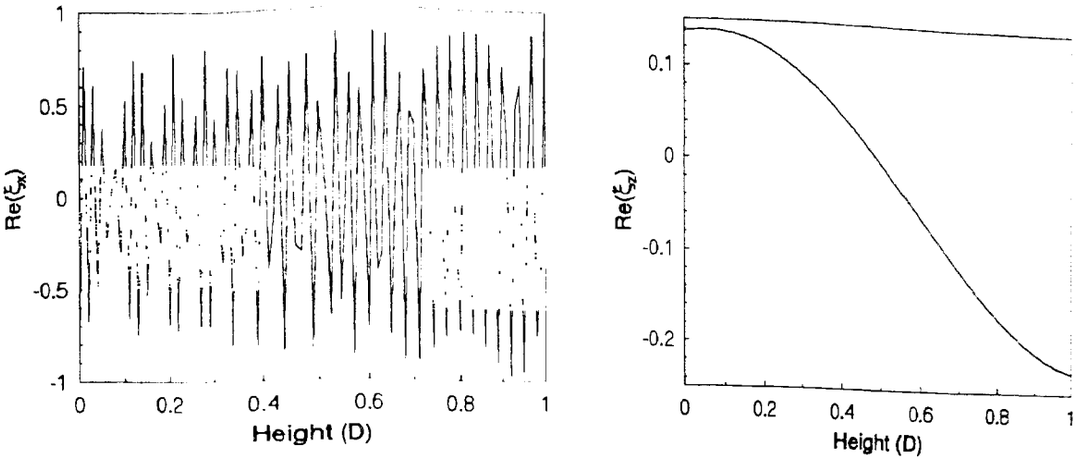

Figure 3.5: The real part of ξ_x (panel a) and ξ_z (panel b) as a function of height for $K = 0.1$ and $\Omega = 3.21$ corresponding to m_{80}- , which is a high frequency magnetic mode. The normalization is arbitrary.

height in the cavity for a $m_{80}-$ mode. The wiggly behavior of the horizontal component are due to the high mode order, which result in closely spaced nodes.

3.3.1.4 p- modes

Let us now turn our attention to a p_1- mode in the $K-\Omega$ diagram for which $K = 0.6$ and $\Omega = 3.23$. The complex diagnostic diagram is not shown for this case, since in Figure 2.5b, the gaps are rather small, so that the complex diagram does not differ from the corresponding real diagram. Figure 3.6 shows the eigenfunctions as a function of height in the cavity. The smaller fluctuations in the $x-$ component of the displacement indicate the influence of the high ordered $m-$ modes. The high frequency $m-$ modes (order 80) which are transverse in nature interact with the p_1- modes and produce these smaller fluctuations in the horizontal component. The absence of these fluctuations in the vertical component reconfirms the influence of the high ordered magnetic modes. Figure 3.6 also shows that $\xi_z >> \xi_x$, which further indicates that these modes are essentially $p-$ or acoustic modes. Now we will concentrate on regions in the diagnostic diagram where the two modes comes closer and the behavior of the resultant mode is a mixture of both.

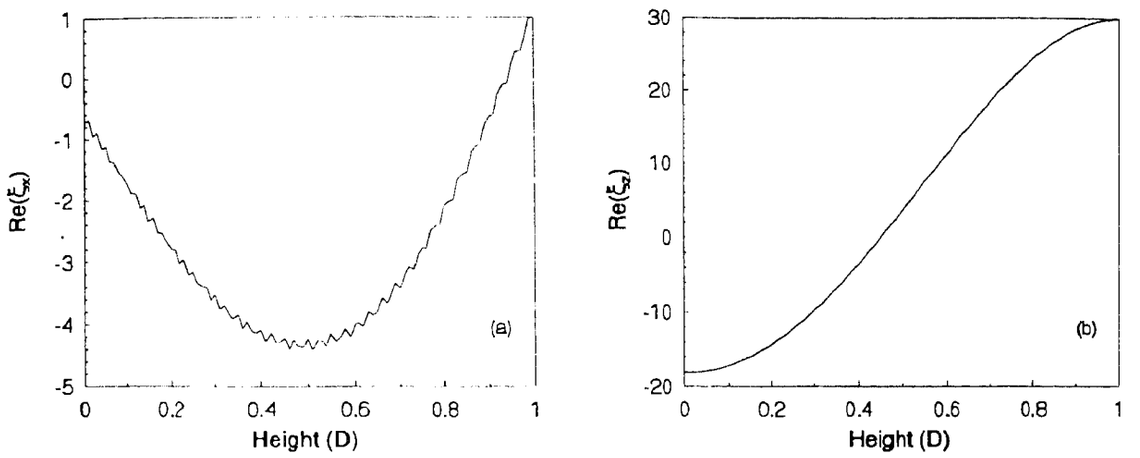

Figure 3.6: The real part of ξ_x (panel a) and ξ_z (panel b) as a function of height for $K = 0.6$ and $\Omega = 3.23$ corresponding to p_1- mode in the high frequency domain of the diagnostic diagram. The normalization is arbitrary.

3.3.2 Mixed modes

3.3.2.1 Coupling between Lamb and m- type mode

Let us concentrate on a mixed mode with $K = 0.072$ and $\Omega = (0.078, 0.0012)$ in order to examine an avoided crossing between the Lamb mode and the magnetic mode (see Fig. 3.9a). Clearly the eigenfunctions will be complex for this mode. Figures 3.7a,b show the real and imaginary components of ξ_x and ξ_z as functions of height in the atmosphere. A comparison of Figures 3.3a, 3.4a with Figure 3.7 reveals that the behavior of the real part of the eigenfunction of the mixed mode closely follows the behavior of the pure Lamb like mode, whereas the imaginary part follows that of the magnetic type. Thus at the avoided crossing, because of strong coupling between these two modes, the resultant mode acquires the properties of both of them. From this we conclude that after a mode transformation these modes exchange their properties but in the avoided crossing regions they lose their individual characteristics and can be regarded as a mixture of the two individual modes.

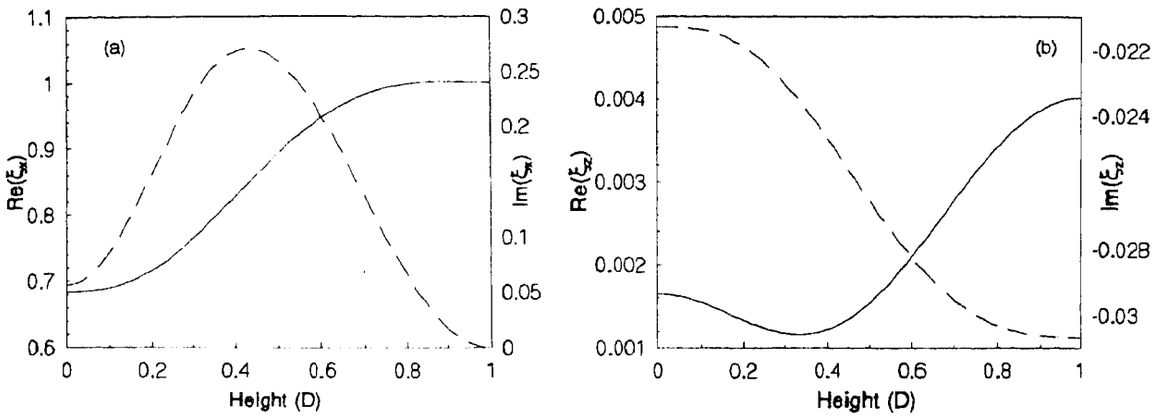

Figure 3.7: The real (solid line) and imaginary (dashed line) parts of displacements as a function of height for $K = 0.072$ and $\Omega = (0.078, 0.0012)$ corresponding to a mixed mode composed of a Lamb type and $m-$ type mode. Panel (a) shows variation of ξ_x and Panel (b) shows the variation of ξ_z. The normalization is arbitrary.

3.3.2.2 Coupling between p- type and m- type mode

Now we look at the high frequency domain of the diagnostic diagram and choose a mode, with $K = 0.416$ and $\Omega = (3.21, 0.0005)$ corresponding to an avoided crossing between a $p-$ mode and a high order $m-$ mode. Figure 3.8 shows the behavior of the eigenfunction of this coupled mode as a function of height in the cavity. A comparison of Figures 3.6a, 3.5a with Figure 3.8a,b indicates that the behavior of the eigenfunction of the coupled mode is a combination of the two individual modes. This is all the more apparent if one compares ξ_z, the vertical components of the eigenfunctions, shown in Figures 3.6b, 3.5b and Figure 3.8c. We therefore find that the real part of the eigenfunction of the coupled mode behaves more as a $p-$ mode and the imaginary component behaves as a high order $m-$ mode, similar to the previous case.

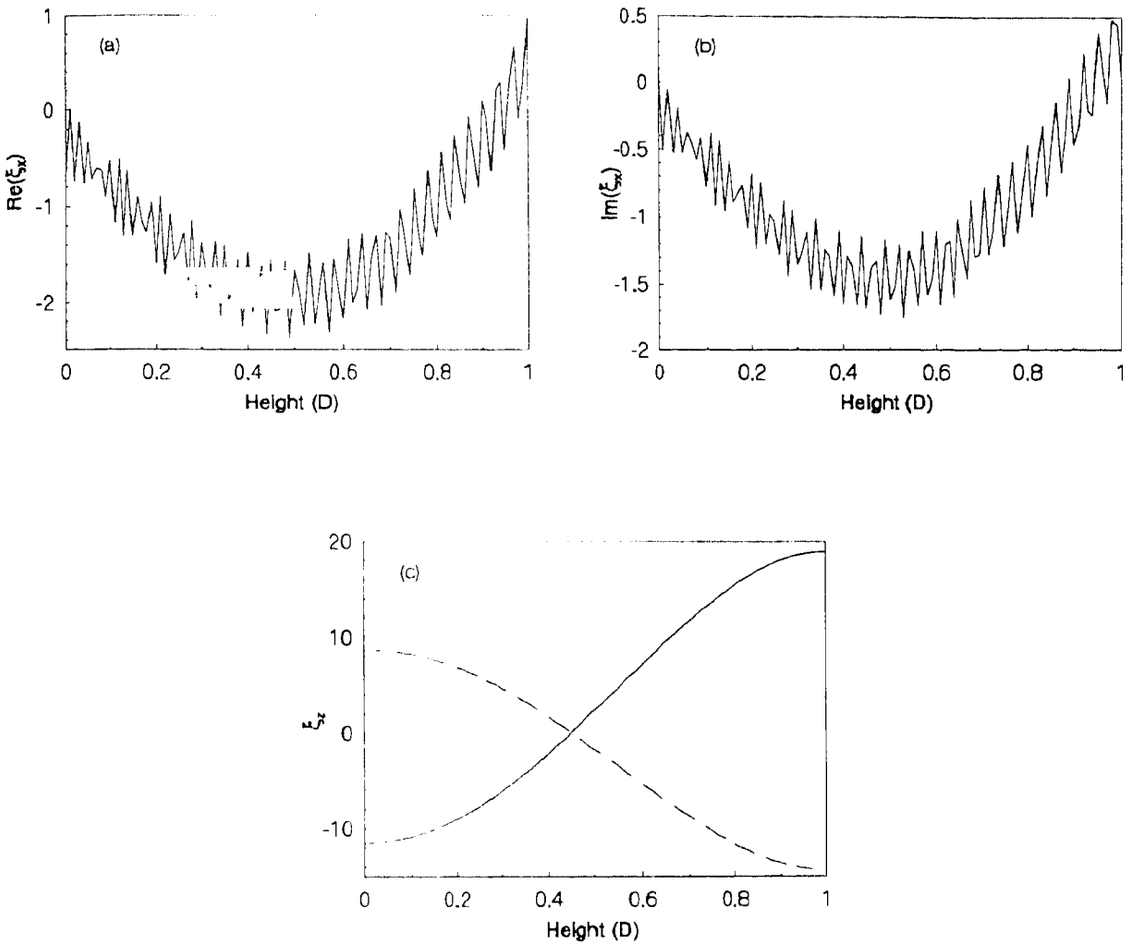

Figure 3.8: Displacements (in arbitrary units) as a function of height for $K = 0.416$ and $\Omega = (3.21, 0.00051)$ corresponding to a mixed mode composed of a $p-$ type and $m-$ type mode. Panel (a) shows the variation of the real part of ξ_x, whereas panel (b) shows the variation of the imaginary part of ξ_x and panel (c) shows the variation of the real (solid line) and imaginary (dashed line) parts of ξ_z.

3.4 Wave-Energy Equation

Let us now consider the energy density and energy flux associated with the MAG waves discussed in the previous Chapter. The wave energy equation can be obtained from the linearized MHD equations and is given by (Bray & Loughhead, 1974),

$$\frac{\partial W}{\partial t} + \nabla \cdot \mathbf{Q} = 0, \tag{3.3}$$

where W denotes the time-averaged energy density and $\mathbf{Q}$ the energy flux. The energy density of the waves is given by,

$$< W >= \frac{1}{4}\rho_0 \mathbf{v} \cdot \mathbf{v}^* + \frac{\delta p \delta p^*}{4\rho_0 c_s^2} + \frac{1}{c_s^2} g^2 \rho_0 (\gamma - 1)\xi_z \xi_z^* + \frac{\delta \mathbf{B} \cdot \delta \mathbf{B}^*}{16\pi} , \tag{3.4}$$

where δp and $\delta \mathbf{B}$ denote the Eulerian perturbations in the pressure and magnetic field respectively and are given by equation (2.13). The time-averaged net upward energy flux is given by,

$$< Q_z >= \frac{1}{4}(\delta p v_z^* + \delta p^* v_z) - \frac{B_0}{16\pi}(\delta B_x v_x^* + \delta B_x^* v_x), \tag{3.5}$$

where the asterisks denotes complex conjugate. The energy density can be split in terms of its various components as follows,

$$W = W_k + W_p + W_g + W_m , \tag{3.6}$$

where

$$W_k = \frac{\gamma p}{4}(v_x \cdot v_x^* + v_z \cdot v_z^*) , \tag{3.7}$$

$$W_p = \frac{p}{4\gamma}(\frac{\delta p}{p} \cdot \frac{\delta p^*}{p}) , \tag{3.8}$$

$$W_g = \frac{\gamma p}{4}\Omega_{\mathrm{BV}}^2(\xi_z \xi_z^*) , \tag{3.9}$$

$$W_m = \frac{\gamma p \epsilon^2}{4}(\frac{\partial \xi_x}{\partial z}\frac{\partial \xi_x^*}{\partial z} + K^2 \xi_x \xi_x^*) . \tag{3.10}$$

The different components W_k, W_p, W_g, W_m are the kinetic, internal, gravity and magnetic energy densities respectively. The energy density and energy flux can be expressed in terms of the eigenfunctions ξ_z and ξ_x and eigenfrequency Ω.

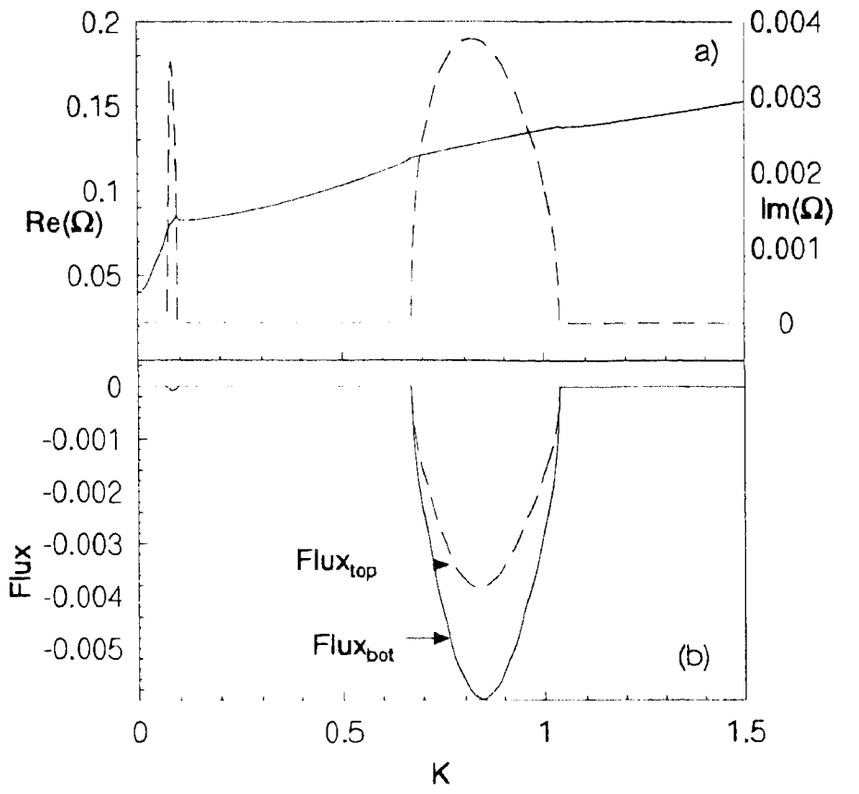

Figure 3.9: Expanded region of the diagnostic diagram showing the interaction between the m_1- mode with the Lamb mode and the gravity mode for zero-gradient boundary conditions. (a) Variation with K of the real (solid line) and the imaginary (dashed line) parts of the frequency, (b) Variation with K of the time-averaged net upward flux from the boundaries as indicated.

3.4.1 Energy Flux

First we will look at the energy flux associated with the individual modes. Figure 3.9 depicts the variation with K of the real (solid line) and imaginary (dashed line) parts of Ω corresponding to the m_1- mode of Figure 3.1. The main difference with the result of Chapter 2 is that we find complex eigenfrequencies in the regions of avoided crossings: instead of voids in the $K-\Omega$ diagran, as found earlier, the branches of the solution are connected by the real part of the complex eigenfrequencies. Also, Im(Ω) has a substantial value in the region where there is a crossing between the magnetic m_1- and the gravity g_1- mode. This behavior is consistent with the asymptotic equations (2.53) and (2.54), if we note that $\delta\Omega^2_{\rm min}$ is negative. Panel (b) in Figure 3.9 depicts the net upward flux from the boundaries. Note that the net negative flux from the

lower boundary is more than the flux leaking out from the top, which indicates that net energy is leaking out from the lower end of the cavity. Moreover the strong interaction between the gravity and magnetic modes results in a considerable amount of energy leakage compared to the Lamb-magnetic mode interaction.

Now we will apply another set of boundary condition, *viz.*

$$\xi_x = \xi_z = 0 \quad \text{at} \quad z = 0 \,, \text{and} \quad \frac{\mathrm{d}\xi_x}{\mathrm{d}z} = \frac{\mathrm{d}\xi_z}{\mathrm{d}z} = 0 \quad \text{at} \quad z = d \,. \tag{3.11}$$

This choice corresponds to a node at the base and an anti-node at the top boundary.

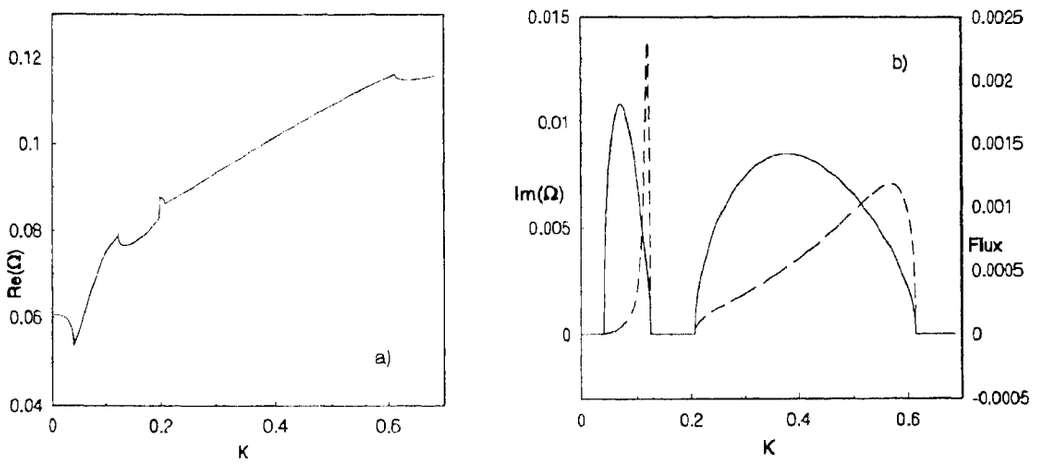

Figure 3.10: Expanded region of the diagnostic diagram showing the interaction between the m_1- mode with the Lamb mode and the gravity mode for mixed boundary conditions. (a) Variation with K of the real (solid line) part of the frequency. (b) The solid line depicts the variation with K of the imaginary part of the frequency and the dashed line depicts the variation with K the time-averaged net upward flux from the top boundary.

As before we allow the frequencies to become complex and follow the behavior of the m_1- mode in the $K - \Omega$ diagram as it interacts with the Lamb and the gravity mode respectively. Figures 3.10a,b show the variation with K of the real and imaginary parts of Ω and the net upward flux by. We find that there is energy leakage from the upper boundary because of a coupling between different modes. The imaginary part of Ω peaks at values of K which correspond to an avoided crossing. Moreover, a comparison of Figure 3.9 with Figure 3.10 suggests that the coupling between the above-mentioned modes is much stronger for the case of mixed boundary conditions

than for the previous case. This results in the imaginary part of Ω having a larger value, leading to an enhanced energy leakage from the top.

3.4.2 Energy density

We now consider the spatial variation of various components of the energy density, first for two elementary wave modes and then for a mixed mode corresponding to an avoided crossing region in the complex $K - \Omega$ diagram.

3.4.2.1 Coupling between a Lamb and m- mode

Figures 3.11a,b show the variations of the different components of the energy density as a function of height for a magnetic Lamb and a magnetic type mode respectively. In this region of the diagnostic diagram ($K = 0.04$) these two modes are uncoupled, and the dominant contribution to the total energy density comes from the internal energy. As we approach an avoided crossing, at $\Omega = (0.078, 0.0012)$ and $K = 0.07$, the contribution of different components of the energy density as a function of height corresponding to a mixed mode is shown in Figure 3.11c. The eigenfunction of this mode (see Fig 3.7) indicates that this mode behaves as a mixture of the two individual modes. It once again clearly reveals that the behavior of the coupled mode is quite different from that of the individual modes. When these modes are away from an avoided crossing they are uncoupled and they can be described as separate elementary modes, but as they approach a crossing these modes coalesce. Thus near an avoided crossing these coalesced modes with complex conjugate roots have the properties of both the modes. Mode conversion process goes on during this period and they reappear as separate modes away from an avoided crossing. This process of mode coalescence leads to mode damping. Note that the magnetic energy does not constitute the dominant component of the total energy of the magnetic mode. This is because the magnetic energy density is proportional to K^2 and ϵ^2 (from Eq. [3.9]) and since K and ϵ are both small by assumption, W_m is also small.

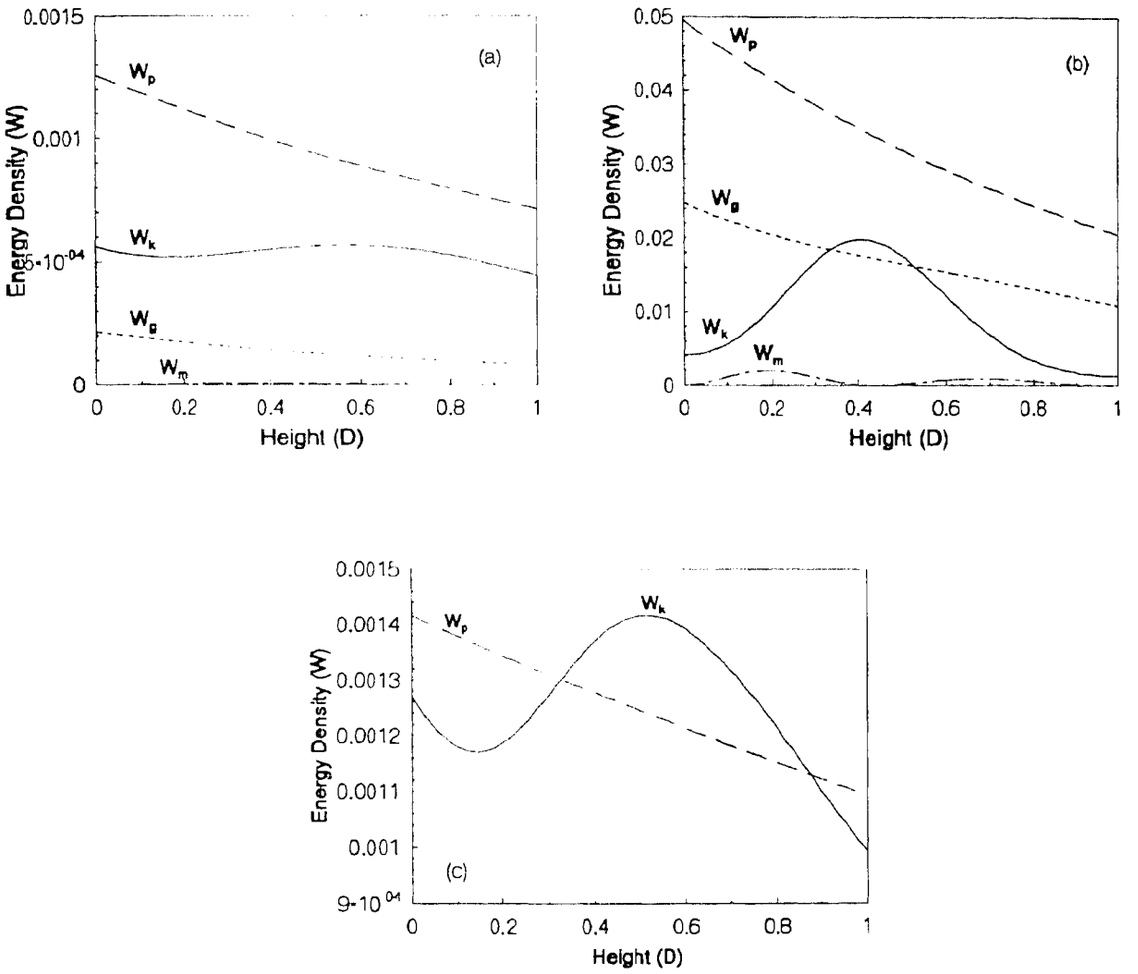

Figure 3.11: Height dependence of energy density of the magnetoatmospheric waves (in arbitrary units). Different line style correspond to different types of energy density (W_k for kinetic, W_p for internal, W_g for gravity and W_m for magnetic). Panel (a) is for $K = 0.04, \Omega = 0.054$ corresponding to a Lamb like mode, (b) for $K = 0.04, \Omega = 0.08$ corresponding to a $m-$ type mode and (c) for $K = 0.07, \Omega = (0.078, 0.0012)$ corresponding to a coupled mode.

3.5 Properties of the gravity-Lamb mode

We have seen that the $gL-$ or gravity-Lamb mode exists only for zero-gradient boundary conditions. The general properties of this mode have already been mentioned in §2.5. Here we will focus our attention on the eigenfunctions and energy densities for the $gL-$ mode, which were not discussed earlier.

3.5.1 Eigenfunction of the $gL-$ mode

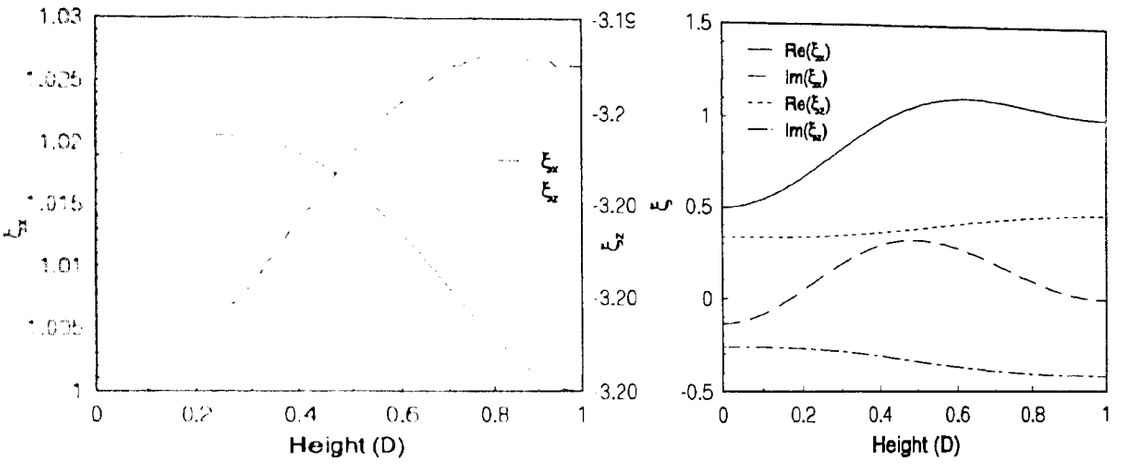

Figure 3.12: Eigenfunctions for $gL-$ mode corresponding to moderate field strength ($\epsilon = 0.1$). In panel (a) the real part of ξ_r and ξ_z are shown by solid and dashed lines respectively for $K = 2.0, \Omega = 0.513$. In panel (b) the various parts of displacements are indicated by different line styles for $K = 0.7$ and $\Omega = (0.77, 0.016)$.

Let us consider a $gL-$ mode with $K = 2.0$ and $\Omega = 0.513$ (see Fig. 2.8), and examine the nature of the eigenfunctions for this mode. For larger values of K the frequency of the $gL-$ mode approaches the Brunt-Väisälä frequency Ω_{BV} (=0.5 in dimensionless units). Figure 3.12a shows the horizontal and vertical components of the Lagrangian displacement for this mode for $\epsilon = 0.1$, which is slightly higher than the default value. (A higher value of ϵ is chosen mainly to isolate this mode from the influence of other modes. For smaller values of ϵ the magnetic modes tend to interfere with this mode.) We find that this mode behaves like a gravity mode in a nonmagnetic atmosphere. Let us follow this mode as K increases and look at its eigenfunction as it interacts

with the Lamb mode. Figure 3.12b shows the variation of different components of the displacements as a function of height for $K = 0.7$ and $\Omega = (0.77, 0.016)$. Note that the mode has acquired a considerable imaginary component because of mode coupling. Consequently this coupled mode can be regarded as a mixture of Lamb and gravity modes. This particular mixed mode has comparable values of the horizontal and vertical components of the displacements, unlike the Lamb mode which is dominantly horizontal. Thus this mode behaves quite differently from the gravity and Lamb modes.

Now let us increase the magnetic field strength further and examine the implication for the $gL-$ mode. Figure 3.13 shows the eigenfunction of a $gL-$ mode with $K = 0.4$ and $\Omega = (0.39, 0.21)$ for a field strength of $B \sim 1000$G *i.e.* $\epsilon = 0.5$ (see Fig. 2.11). For this set of values of K and Ω this mode is expected to behave as Lamb-like. In Figure 3.12b ($\epsilon = 0.1$) and Figure 3.13 ($\epsilon = 0.5$) the magnitude of the vertical displacements does not vary with height. Thus, the qualitative nature of the $gL-$ mode remains unchanged when the magnetic field strength increases.

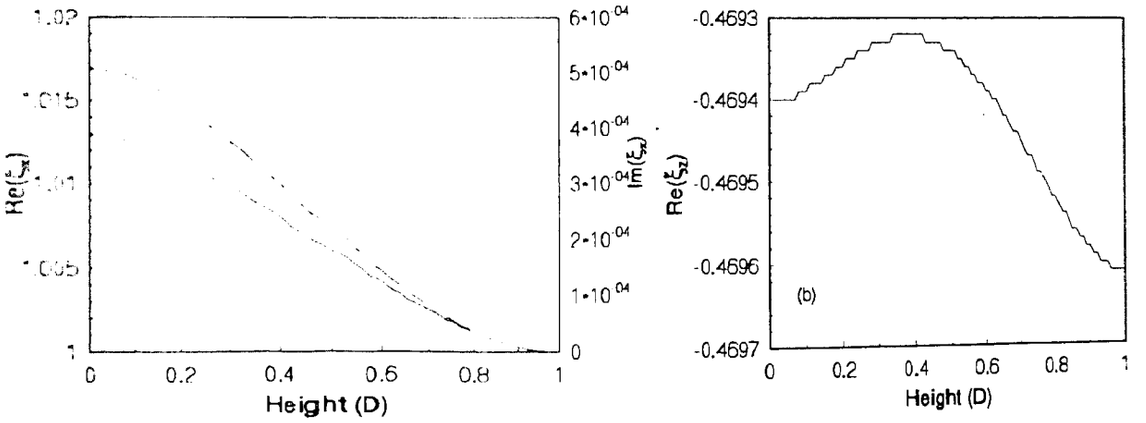

Figure 3.13: Eigenfunctions for $gL-$ mode corresponding to moderate field strength ($\epsilon = 0.5$) with $K = 0.4, \Omega = (0.39, 0.21)$. In panel (a) the real (solid line) and imaginary (dashed line) parts of ξ_x are shown. Panel (b) shows the real part of ξ_z.

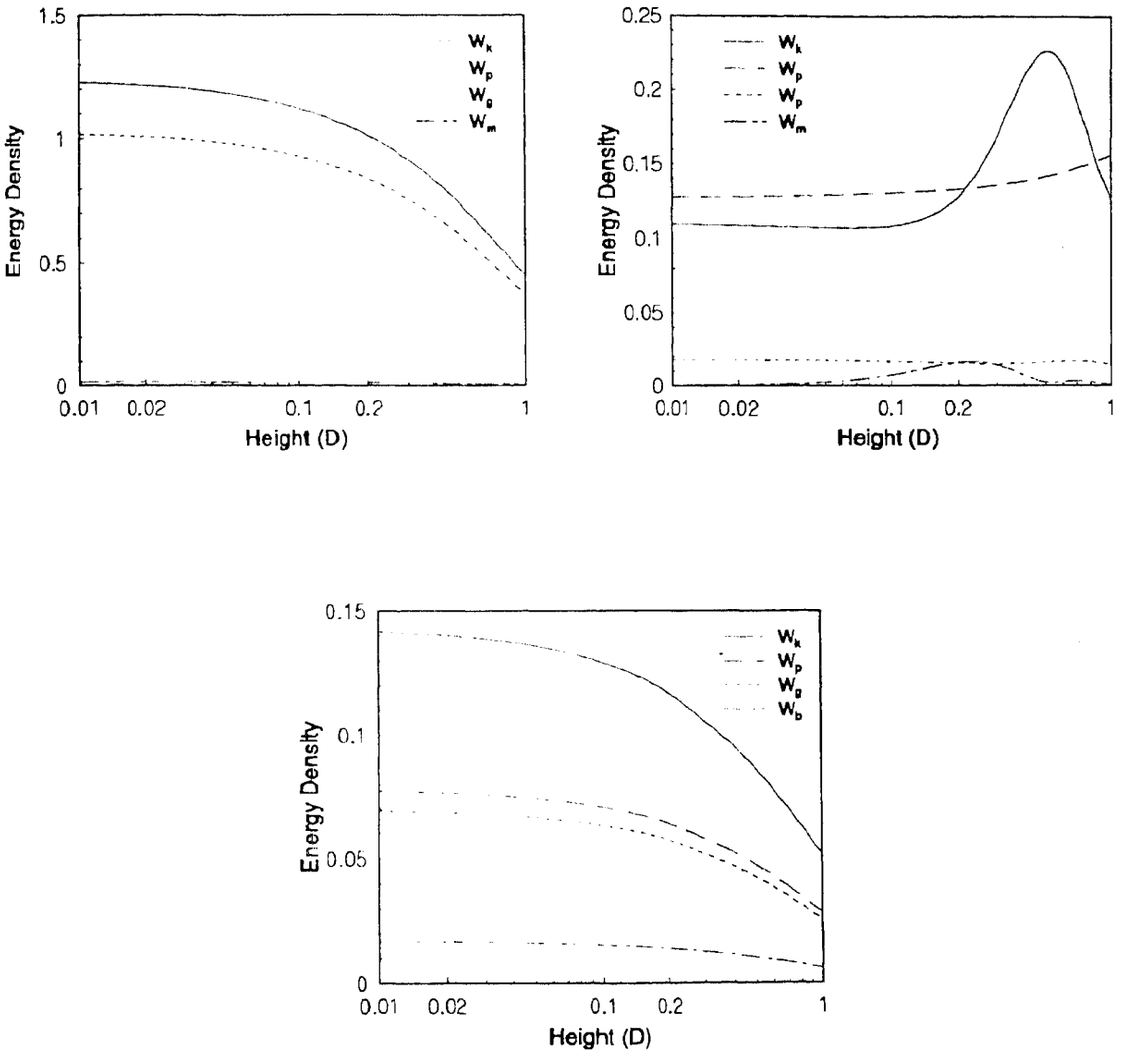

Figure 3.14: Energy density of the $gL-$ mode for (a) $K = 2.0$, $\Omega = 0.51$, and $\epsilon = 0.1$, (b) $K = 0.7$, $\Omega = (0.77, 0.016)$ and $\epsilon = 0.1$, (c) $K = 0.4$, $\Omega = (0.39, 0.21)$ and with slightly higher field strength $\epsilon = 0.5$. Different line styles corresponds to different types of energy density as labeled.

3.5.2 Energy density of the $gL-$ mode

Let us concentrate on the different components of the energy density as a function of height for the $gL-$ mode with $K = 2.0$ and $\Omega = 0.51$ (corresponding eigenfunctions are plotted in Fig. 3.12a). Figure 3.14 shows the variation of the different components of the energy densities with height. Figure 3.14a reveals that the kinetic and gravitational energy densities are the dominant ones whereas the internal and magnetic ones are negligible. This mode has the character of a gravity mode. If we now turn our attention to the complex $gL-$ mode with $K = 0.7$ and $\Omega = (0.77, 0.016)$ and examine panel (b) in the above figure, we find that its behavior is considerably different from panel (a), indicating that this mixed mode does not have the nature of a gravity mode. For this mode, the internal energy density forms the dominant component, suggesting the similarity to a Lamb mode (see Fig. 3.11a). We now consider the $gL-$ mode with $K = 0.4$ and $\Omega = (0.39, 0.21)$ for a higher field strength, $\epsilon = 0.5$ (see Fig. 2.11). From Figure 3.14 we find that the internal energy density is comparable to the kinetic energy density — which is generally true for a Lamb mode, unlike that for a gravity mode. This further confirms the conclusion drawn in the earlier Chapter that the $gL-$ mode behaves as a Lamb like mode for low K, and as a gravity mode for large K.

3.6 Strong magnetic field case

We consider now an isothermal atmosphere extending over several scale heights (large D). This situation is more realistic as far as the solar photosphere is concerned. At the lower boundary, the Alfven speed is typically less than the sound speed, but at higher levels the contrary is true. If we consider an atmosphere with a vertical extent of several scale heights, then over most of the atmosphere the strong field solutions of the wave equation are applicable (see §2.6).

Let us look at the complex $K - \Omega$ diagram for high magnetic fields. Figure 3.15a, shows an enlarged portion of the diagnostic diagram (Fig. 2.12b) for $D = 10, \epsilon = 0.5$. The long-dashed line represents the $m-$ type solutions. Note that the voids are filled with the real part of the complex frequencies. Figure 3.15b also reveals that there are peaks in the complex frequency, corresponding to a mode coupling between the $p-$

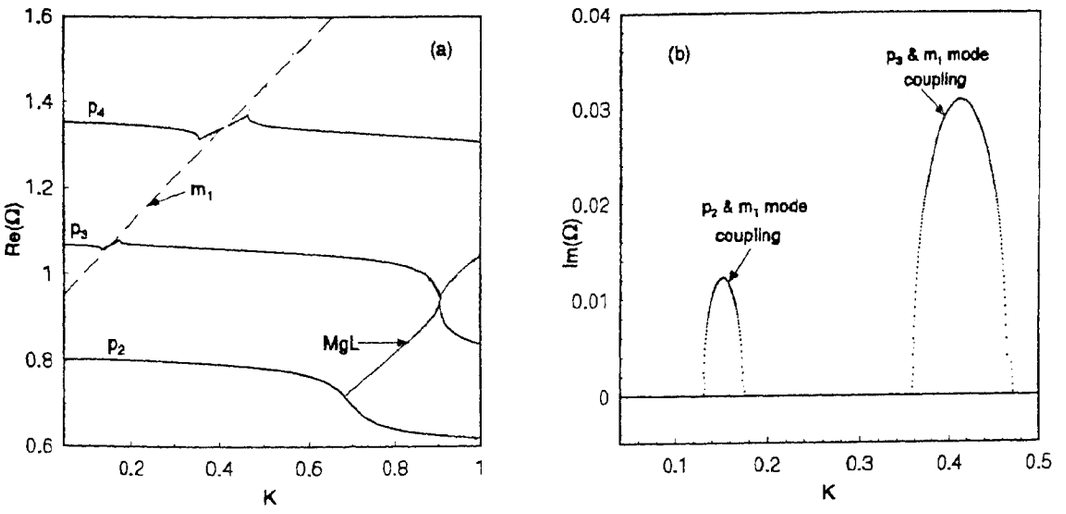

Figure 3.15: Enlarged portion of the diagnostic diagram in the strong field case with $D = 10$ and $\epsilon = 0.5$. Panel (a) shows the variation of real part of the frequency and panel (b) shows the variation of the imaginary part of the frequency with K.

and $m-$ modes. Mode coupling leads to a temporal decay of oscillations with a form $\exp(-t/\tau_D)$, where $\tau_D = \mathrm{Im}(1/\omega)$ denotes the characteristic damping. Table 3.1 lists the eigenfrequencies of a few coupled modes corresponding to a structure with $D = 10$ and $B = 1200$ G. It clearly indicates that the coupling of the $p-$ modes with the $m-$ modes is not as strong compared with its coupling to the $MgL-$ mode. The lifetime of the mixed mode composed of $p-$ and $m-$ modes is very large, it decays after several time periods, whereas the coupled $p-$ and $MgL-$ modes decay within two oscillation periods. Thus mode coupling alone enables certain modes to decay rapidly, even when there is no explicit dissipative mechanism. It also indicates that for a sunspot umbra the coupling between a $p-$ and $m-$ mode leads to an energy leakage of a small amount whereas the coupling of other modes with the $MgL-$ mode could be very important for small flux tubes with radii in the range 300 to 500 km. Note that this enhanced coupling with the $MgL-$ mode can be observed for large K values only; thus mode coupling with the $MgL-$ mode may not be important for wave leakage from sunspot umbra. Before we focus our attention to the application of our result to sunspots in detail (Chapter 4), we would like to study the general properties of the modes present in sunspots, in this Chapter.

Coupled mode type	K	Radius (km)	Re(Ω)	Im(Ω)	P(S)	$\tau_D(S)$	τ_D/P
p_2 & m_1	0.15	2100	1.066	0.0121	91	1271	13.97
p_3 & m_1	0.38	825	1.325	0.0249	73	618	8.46
p_2 & MgL	0.75	420	0.775	0.1225	125	125	1.00
MgL & Lamb	0.84	375	0.854	0.106	114	145	1.27
p_3 & MgL	0.93	338	0.982	0.079	99	195	1.96

Table 3.1: Eigenfrequencies (corresponding to different magnetic structures) of different coupled modes for a model atmosphere with $D = 10, B = 1.2$ kG.

3.6.1 Energy densities

Now we will discuss the properties of the modes in the strong field case (discussed in §2.6.1), particularly the height variation of the energy density and its various constituents. Let us focus on modes corresponding to $D = 10$, $\epsilon = 0.5$ (see Fig. 3.15a) subject

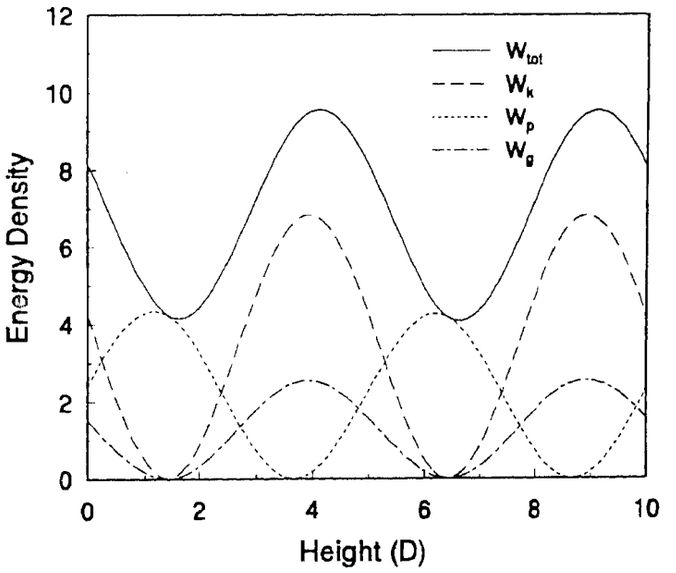

Figure 3.16: Height variation of the different components of the total energy density in a slow magnetoacoustic mode corresponding to a p_2- mode for an atmosphere with $D = 10.0$, $\epsilon = 0.5$, $K = 0.1$ and $\Omega_{p2} = 0.8$.

to zero-gradient boundary conditions. Figure 3.16 shows the variation of different components of the energy density with z for the p_2- or second order slow magnetoacoustic

mode with $K = 0.1$ and $\Omega_{p2} = 0.8$. Figure 3.16 reveals that the kinetic energy density is the dominant component to the total energy density, whereas the internal and gravity energies contribute to a lesser extent. However, the magnetic energy also does not contribute, which is not surprising since we are essentially dealing with an acoustic mode in a cavity. We also find that the total energy density is a harmonic function of height and is spread over the entire extension of the cavity. Let us turn our attention

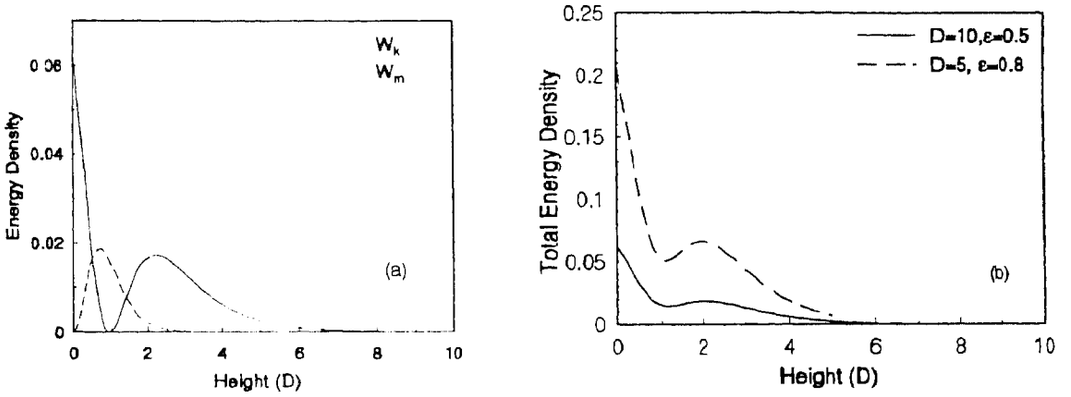

Figure 3.17: Energy density of the fast magnetoacoustic mode in the high magnetic field case. Panel (a) shows the kinetic(solid line) and magnetic (dashed line) energy density corresponding to m_1- mode in an atmosphere with $D = 10.0$ and $\epsilon = 0.5$ at $K = 0.01$ and $\Omega_{m1} = 0.96$. Panel (b) shows the total energy density corresponding to m_1- mode. The dashed line corresponds to an atmosphere with $D = 5.0, \epsilon = 0.8$ at $K = 0.1, \Omega_{m1} = 1.6$ and the solid line corresponds to an atmosphere with $D = 10.0, \epsilon = 0.5$ at $K = 0.01, \Omega_{m1} = 0.96$.

to the fast magnetoacoustic modes or $m-$ modes in the strong field limit. Figure 3.17a shows the height variation of the various components of the total energy density for $D = 10.0, \epsilon = 0.5$ for the m_1- mode with $K = 0.01$ and $\Omega_{m,1} = 0.96$. In Figure 3.17b we show the energy density in a fast magnetoacoustic mode for different values of D and ϵ. The solid line corresponds to the m_1- mode for $D = 5.0, \epsilon = 0.8$ at $K = 0.1$ and $\Omega_{m,1} = 1.6$, and the dashed line correspond to $D = 10.0, \epsilon = 0.5$ at $K = 0.01$ and $\Omega_{m,1} = 0.96$. If we examine the fast mode, we notice that the wave energy density decreases rapidly with height, which suggests that such waves are localized in the lower regions of the atmosphere within a few scale heights of the bottom boundary. In the lower part of the cavity, the main contribution to the total energy density comes from the magnetic and kinetic energy. The latter is mainly due to the horizontal velocity

perturbation. This is of course related to the fact that we are dealing with a fast mode of the magnetic type trapped in a cavity, in which the wave is reflected back at a fairly low height, due to the rapid increase of the Alfvén speed. We now examine the proper-

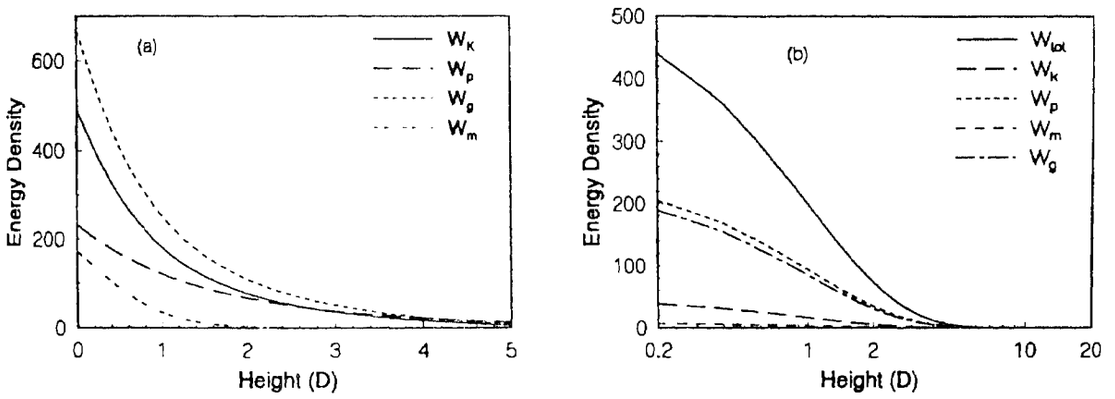

Figure 3.18: Height variation of the energy density for $MgL-$ mode in an atmosphere with (a) $D = 5.0, \epsilon = 0.8$ at $K = 1.5$ and $\Omega = 0.412$, (b) $D = 20.0, \epsilon = 1.05$ at $K = 0.2$ and $\Omega = 0.2$.

ties of the $gL-$ mode in the strong field limit. Indeed because of the strong magnetic field, the pure $gL-$ mode modifies into a magneto- gravity-Lamb mode or $MgL-$ mode (as already pointed out in §2.6.1). Figure 3.18a shows the height dependence of energy density for a $MgL-$ mode in an atmosphere with $D = 5.0, \epsilon = 0.5$ for $K = 1.5$ and $\Omega = 0.412$ (Fig. 2.12a shows the corresponding $K - \Omega$ diagram). Note that the gravitational energy is the major contributor to the total energy density of this mode, which further supports the fact that this mode behaves essentially as a gravity mode for large K. Because of the strong magnetic field the magnetic energy density has also grown considerably as compared to Figure 3.14a. We also find that the energy density falls off very rapidly with height similar to the fast modes. Let us increase the height of the cavity still further to $D = 20$ and also consider a large magnetic field strength such that $\epsilon = 1.05$. This choice of parameters might be relevant to an active magnetic field concentration region. The height dependence of the energy density for the $MgL-$ mode has been plotted in Figure 3.18b with $K = 0.2$ and $\Omega = 0.2$ (Fig. 2.13 shows the corresponding $K - \Omega$ diagram). Note that the magnetic and the internal parts are the dominant contributors to the total energy density. We find once again that similar to

the fast modes, the energy density for this mode is localized in the lower lower part of the atmosphere. This suggests that the $MgL-$ mode may not be a good candidate for heating the atmosphere above highly concentrated magnetic field structures.

3.6.2 Umbral oscillations

Let us now consider the application of our result to umbral oscillations. As already pointed out, observed umbral oscillation falls in the range 120 - 200 s. From the preceding discussion and that in Chapter 2, we find that these oscillations fall into three basic categories associated with slow, fast and $MgL-$ modes. The last two are essentially confined to photospheric regions (*i.e.*the lower part of the atmosphere), where the wave energy density in the former is spread over the entire extension of the cavity. As far as wave heating is concerned, the slow mode appears to be a more promising candidate than the other two. Figure 3.19 shows a part of the diagnostic diagram for $D = 20$(Chromospheric height) and $\epsilon = 1.3$ ($B = 3000$ G) corresponding to the zero-gradient boundary condition. (This diagnostic diagram could be relevant for observed

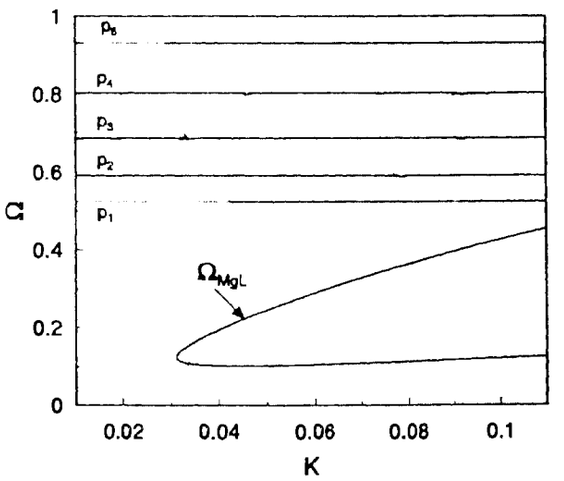

Figure 3.19: Enlarged portion of the diagnostic diagram in the strong field case with $D = 20$ and $\epsilon = 1.3$ ($B = 3000$ G).

umbral oscillation, and differs from the one given by Hasan (1991), in the choice of

boundary conditions. In this part of the diagnostic diagram we find only slow modes and the $MgL-$ mode. The figure reveals the absence of avoided crossings since the modes are widely separated in frequency, suggesting that they can be studied in terms of uncoupled modes. Figure 3.19 also indicates that for the slow modes the frequency

Mode type	Ω	P(s)
MgL	0.2969	325
p_1	0.5241	184
p_2	0.5905	164
p_3	0.6870	140
p_4	0.8029	120

Table 3.2: Eigenfrequencies of different modes corresponding to a sunspot with $D = 20, B = 3$ kG and radius = 5000 km.

hardly varies with K; moreover these frequencies match well the ones calculated from expression (2.67). Thus in the limit $K \to 0$, the dispersion relation (Eq. [2.67]) is quite accurate. One can also show that these slow modes are insensitive to the strength of the magnetic field as already pointed out by Hasan (1991). Table 3.2 lists

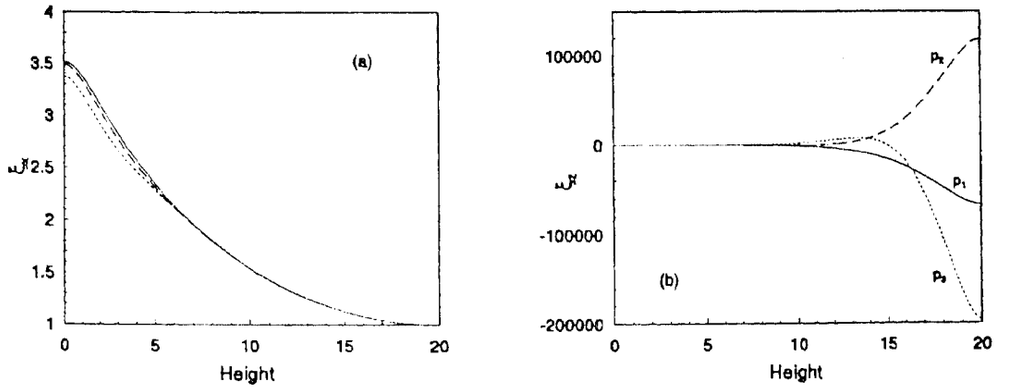

Figure 3.20: The real part of ξ_x (panel a) and ξ_z (panel b) as a function of height for $K = 0.1$ corresponding to different order $p-$ modes as labeled with frequencies $\Omega_{p1} = 0.524, \Omega_{p2} = 0.59, and \Omega_{p3} = 0.687$ for an umbra with $D = 20$ and $B = 3000$ G. The normalization is arbitrary.

calculated eigenfrequencies from Figure 3.19 for $K = 0.062$, which corresponds to a typical sunspot umbra with a radius of 5000 km. It shows that the uncoupled slow modes are very much within the observed range. Thus the mode leakage phenomenon

due to mode coupling may not be as important for sunspots, as for small flux tubes as already pointed out(see Table 3.1 and Fig. 3.15). To shed further lights on the properties

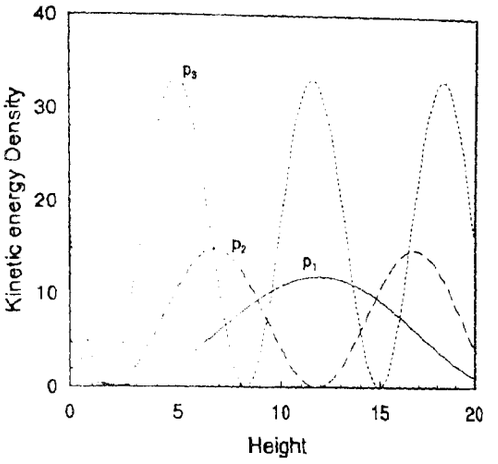

Figure 3.21: Variation of W_{kin} with z for $n = 1, 2, 3$ assuming $B = 3000$ G and $K = 0.1$ (Radius = 3150 km). The normalization is arbitrary.

of the slow modes we plot the eigenfunctions and kinetic energy densities associated with these modes. Figure 3.20a,b depict the variation of ξ_x and ξ_z with height for the first three ordered slow modes. The change in ξ_z, close to the upper boundary, occurs because of the rapid decrease in the density. Now let us examine the variation of the kinetic energy density with height for various order $p-$ modes. Figure 3.21 shows the height variation of W_{kin}. Note that the energy of the modes is distributed uniformly over the height range under study. The occurrence of multiple peaks for higher order is due to the existence of nodes in the velocity distribution.

3.7 Conclusion

In this study we have undertaken a detailed examination of the complex wave frequency spectrum. On the basis of quantitative calculations, the present analysis has brought out many useful properties of waves in a magnetized stratified medium. The asymptotic analysis in the weak field limit carried out in Chapter 2 predicted the presence of complex roots in certain regions of the $k - \omega$ diagram. Indeed, our calculations show that the large gaps near the vicinity of avoided crossings (found under the assumption

of real frequencies) get filled up by the real part of the complex frequency. In these regions, the imaginary part of the frequency is finite, and zero elsewhere. An interesting feature of the results concerns the nature of the eigenfunctions when there is a strong coupling between modes. We find that at the avoided crossings between two modes, the mixed mode acquires the properties of both the modes, which manifests itself by the real and imaginary components of the displacement taking on the characteristics of both the modes.

An important consequence of the above results is that mode coupling can lead to a leakage of wave energy from the cavity, *even in the absence of a dissipative mechanism.* It appears that the boundary conditions permit the phase relationship between the modes to be changed in a manner so as to allow the wave to leak out from the boundary, thereby leading to a loss of energy from the cavity. This behavior occurs only when there is a strong mode coupling for certain combination of frequencies and wave numbers. For the strong magnetic field case, we find that the coupling of the $MgL-$ mode with a $p-$ mode can lead to a leakage of the wave energy from a cavity in a time as short as two oscillation periods. This may be relevant for small flux tubes of radii in the range 300-500 km. Our results complement those of Cally and Bogdan (1993) and Cally, Bogdan and Zweibel (1994), where wave-leakage through the lower boundary of a magnetized polytropic atmosphere is explicitly taken into account. However, in our calculations the leakage of wave energy occurs precisely at the avoided crossings, but not elsewhere.

By studying the the height variation of the wave energy density and its different constituents, we have been able to get further insight into the nature of the various modes in the atmosphere. For parameters typical to sunspots, we find that the fast and $MgL-$ modes are localized in the lower part of the cavity, whereas the slow mode energy is distributed over the full extension of the cavity. We identify the slow mode as a potential candidate for heating the atmosphere in active regions. For umbral oscillations, our results are complementary to those of Hasan (1991), who made a detailed analysis of the nature of various modes in sunspots.

Despite the assumption of an isothermal atmosphere, our results provide an insight into the fundamental nature of mode coupling in magnetic flux tubes. So far we have

assumed adiabatic conditions, in the forthcoming Chapter we enlarge the scope of our analysis by explicitly taking the influence of radiative damping on the various wave modes.

Chapter 4

Effects of Radiative Cooling on Waves

4.1 Background

In the previous Chapters the interaction of various elementary modes in a stratified magnetized atmosphere was studied in the purely adiabatic limit. Oscillations in a realistic stellar atmosphere are affected by radiative dissipation and energy losses at the boundaries. Thus the modes are damped and have complex frequencies. In this Chapter we examine the influence of non-adiabatic effects on the modes of an isothermal stratified magnetized atmosphere. The inclusion of radiative dissipation based on Newton's law of cooling demonstrates the importance of this effect in the study of magnetoatmospheric waves. It was pointed out by Bünte and Bogdan (1994) that Newtonian cooling can be incorporated in the solution of isothermal magnetoatmospheric wave problem by replacing γ, the ratio of specific heats, by a complex frequency-dependent quantity. This procedure permits one to generalize easily the previous calculations to include radiative dissipation. Bünte and Bogdan treated a planar, isothermal and stratified atmosphere in the presence of a horizontal magnetic field, whereas in this study we consider a vertical magnetic field. We shall consider the effects of radiation losses on MAG waves in a stratified magnetized atmosphere. We consider wave damping by radiative energy exchange, which is likely to be efficient in the solar photosphere, where radiative relaxation times are very short compared to typical wave periods. By comparison, damping of hydromagnetic waves due to viscous dissipation and particle conduction is entirely negligible in those layers of the solar atmosphere where small amplitude disturbances are likely to occur. As we will see later, the condition for the

propagation of gravity waves, which depends on the existence of the buoyancy force, is more stringent in the presence of radiative damping than in its absence (Bray and Loughhead, 1974). Equally significant are the changes which result in the phase and amplitude relationship among the perturbations in density, pressure, temperature, and velocity. In fact, observations of such relationships may ultimately prove to be of crucial importance in identifying the wave modes actually present in the solar photosphere and chromosphere. In this connection, Schatzman and Souffrin (1967) have pointed out that radiative damping may lead to heating of the atmosphere.

Noyes and Leighton (1963) pointed out that the time scale τ_R for radiative relaxation is of the order of 1 s at the photospheric level, but increases rapidly with height. Leighton *et al.* (1962) measured the mean lifetime of oscillations by the decay of the velocity time autocorrelation function and give a value of 380 s. According to Zirker (1964), oscillations persist for 2 to 4 cycles. Deubner (1967) gives 20 min as a mean lifetime. Temperature fluctuations which are correlated with the oscillations were observed by Leighton *et al.* (1962).

The radiative damping of oscillatory modes in a optically thin, isothermal, unmagnetized medium was studied by several authors (Stix, 1970; Souffrin, 1972; Mihalas and Mihalas, 1984). Bogdan and Knölker (1989) obtained the dispersion relation for linear compressive plane waves in a homogeneous, unstratified, uniformly magnetized radiating fluid. Here we consider the propagation of optically thin MAG waves in a stratified, uniformly magnetized medium in which radiative energy exchange occurs through Newton's law of cooling. The main effect of radiation is to damp the waves. The plan of the Chapter is as follows: in §4.2, the basic wave equations are presented, including Newton's law of cooling. This is followed in §§4.3 and 4.4 by an analysis of the asymptotic solutions in the limits of vanishing and infinite horizontal wave number respectively. In §4.5 we present the dispersion relation for a weak field followed by numerical results in the form of $K - \Omega$ diagram. In §4.6 we treat the strong field case. Finally, a discussion of the results are taken up in §4.7.

4.2 The wave equation with Newtonian cooling

We shall confine our attention to an isothermal atmosphere with a vertical magnetic field which is unbounded in the horizontal direction. In addition to the momentum equation (Eq. [2.2]), we rewrite the energy equation as,

$$\partial_t \frac{\delta T}{T} + \delta v_z \frac{1}{T}\frac{\mathrm{d}T}{\mathrm{d}z} + (\gamma - 1)\nabla \cdot \delta v = -\frac{1}{\tau_R}\frac{\delta T}{T} \tag{4.1}$$

where $\delta \mathbf{v} = \partial_t \vec{\xi}$ is the velocity perturbation, T is the temperature of the gas and δT the temperature perturbation. We assume the Lagrangian displacement $\vec{\xi}$ varies $e^{i(\omega t - kx)}$, where ω is the angular frequency and k is the horizontal wave number. Unlike the adiabatic case considered previously, we allow for radiative losses, approximating them by Newton's law of cooling (*e.g.* Spiegel, 1957; Mihalas and Mihalas, 1984), which assumes that temperature fluctuations are damped radiatively on a time scale τ_R, given by

$$\tau_R = \frac{\rho c_v}{16\chi\sigma T^3}. \tag{4.2}$$

where χ is the mean absorption coefficient per unit length, c_v the specific heat per unit volume, and σ the Stefan-Boltzmann constant. For simplicity, we assume that τ_R is constant over the atmosphere. If the vertical dimension of the perturbation is small compared to the local scale height, the relation between the Lagrangian perturbations in pressure p and density ρ is then approximately given by $\delta p/p \simeq \gamma^* \delta\rho/\rho$, where

$$\gamma^*(\omega) = \frac{1 + i\omega\tau_R\gamma}{1 + i\omega\tau_R}\ ; \tag{4.3}$$

With these assumptions, the linearized equations for MAG waves are given by a system of two coupled differential equations,

$$[v_A^2 \frac{\mathrm{d}^2}{\mathrm{d}z^2} - (\tilde{\gamma}c_S^2 + v_A^2)k^2 + \omega^2]\xi_x - ik(\tilde{\gamma}c_S^2 \frac{\mathrm{d}}{\mathrm{d}z} - g)\xi_z = 0\ , \tag{4.4}$$

$$[\tilde{\gamma}c_S^2 \frac{\mathrm{d}^2}{\mathrm{d}z^2} - \tilde{\gamma}\gamma g \frac{\mathrm{d}}{\mathrm{d}z} + \omega^2]\xi_z - ik[\tilde{\gamma}c_S^2 \frac{\mathrm{d}}{\mathrm{d}z} - (\tilde{\gamma}\gamma - 1)g\ ]\xi_x = 0\ , \tag{4.5}$$

where ξ_z and ξ_x are the amplitudes of the vertical and horizontal displacement, g is the acceleration due to gravity, and $\tilde{\gamma} = \gamma^*/\gamma$. The adiabatic sound speed and Alfvén speed are given, respectively, by

$$c_S = \sqrt{\frac{\gamma p}{\rho}} \quad \text{and} \quad v_A = \frac{B}{\sqrt{4\pi\rho}}\ . \tag{4.6}$$

equations (4.4) and (4.5) have the same structure as the linearized wave equation for adiabatic perturbations (see Eqs. [2.16]–[2.16]), apart from the appearance of the parameter $\tilde{\gamma}$, which incorporates radiative cooling. In non-dimensional form equation (4.3)

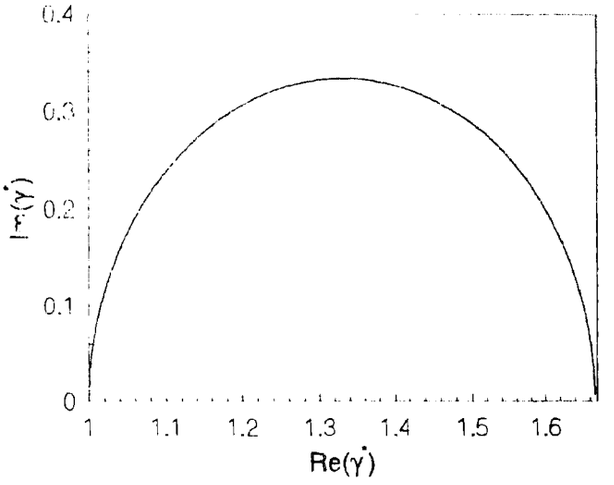

Figure 4.1: The complex parameter γ^* as a function of $\Omega\tilde{\tau}_R$. As $\Omega\tilde{\tau}_R$ varies from 0 to ∞, γ^*, defined in Eq. (4.7), describes a semi-circle in the complex plane.

can be written as

$$\gamma^* = \frac{1 + i\Omega\tilde{\tau}_R\gamma}{1 + i\Omega\tilde{\tau}_R} , \tag{4.7}$$

where the dimensionless relaxation time scale is given by $\tilde{\tau}_R = (c_S/H)\tau_R$. As $\Omega\tilde{\tau}_R$ varies from 0 to ∞ , γ^* describes a semi-circle in the complex plane as shown in Fig 4.1 (see also Bünte and Bogdan). Figures 4.2 a and b show the variation of the real and imaginary parts of γ^* respectively as a function of $\Omega\tilde{\tau}_R$. We find that for $\Omega\tilde{\tau}_R < 0.1$, γ^* approaches the isothermal limit, and $\gamma^* = 1$. For $\Omega\tilde{\tau}_R > 10$, $\mathrm{Re}(\gamma^*) = 5/3 = \gamma$. Thus in the limit $\tau_R, \rightarrow \infty$ *i.e.* in the limit of adiabatic perturbations, $\gamma^* = \gamma$ and $\tilde{\gamma} = 1$. Letting $\tilde{\gamma} = 1$ in equations (4.4) and (4.5) we recover the linearized equations given in Chapter 2. The imaginary contribution to γ^* is maximum for $\Omega\tilde{\tau}_R \sim 1$. Thus to study the maximum effect of radiative heat exchange we should choose our parametric values such that $\Omega\tilde{\tau}_R$ becomes close to 1. In terms of the variables defined by equations (2.20) – (2.22), equations (4.4) and (4.5) can be combined into a fourth-order differential

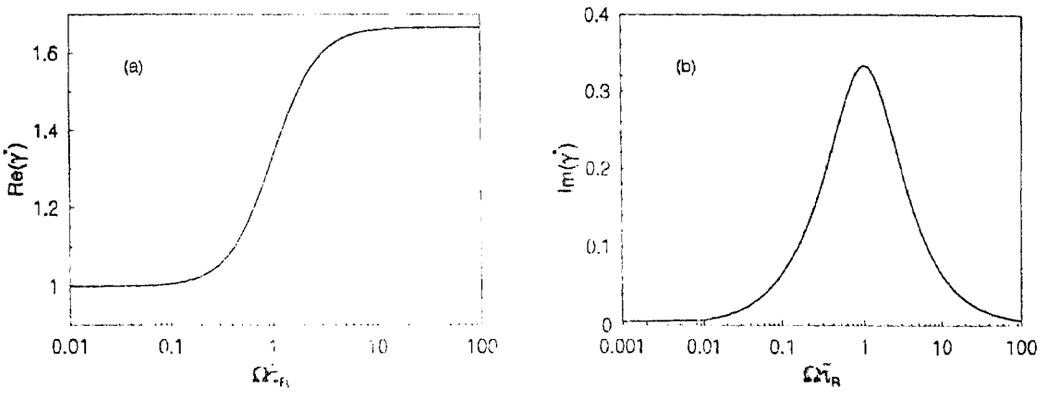

Figure 4.2: The complex parameter γ^* as a function of $\Omega\tilde{\tau}_R$. Panels (a) represents the variation of the real part and (b) represents the variation of the imaginary part of γ^*.

equation for ξ_x,

$$\Big\{\theta^4\frac{\mathrm{d}^4}{\mathrm{d}\theta^4}+4\theta^3\frac{\mathrm{d}^3}{\mathrm{d}\theta^3}+[1+4(\frac{\Omega^2}{\tilde{\gamma}}-K^2)+4\theta^2]\theta^2\frac{\mathrm{d}^2}{\mathrm{d}\theta^2}-[1-4(\frac{\Omega^2}{\tilde{\gamma}}+K^2)-12\theta^2]\theta\frac{\mathrm{d}}{\mathrm{d}\theta}$$
$$+16[(\frac{\Omega^2}{\tilde{\gamma}}+K^2(\frac{\tilde{\Omega}_{\mathrm{BV}}^2}{\Omega^2}-1))\theta^2-\frac{\Omega^2K^2}{\tilde{\gamma}}]\Big\}\xi_x=0\ ,(4.8)$$

where $\tilde{\Omega}_{\mathrm{BV}}^2=(\gamma^*-1)/\gamma\gamma^*$ is the square of the effective Brunt-Väisälä frequency (in dimensionless units). This Brunt-Väisälä frequency is a function of frequency in the non adiabatic case. Figure 4.3 shows the dependence of $\tilde{\Omega}_{\mathrm{BV}}$ on the radiative relaxation

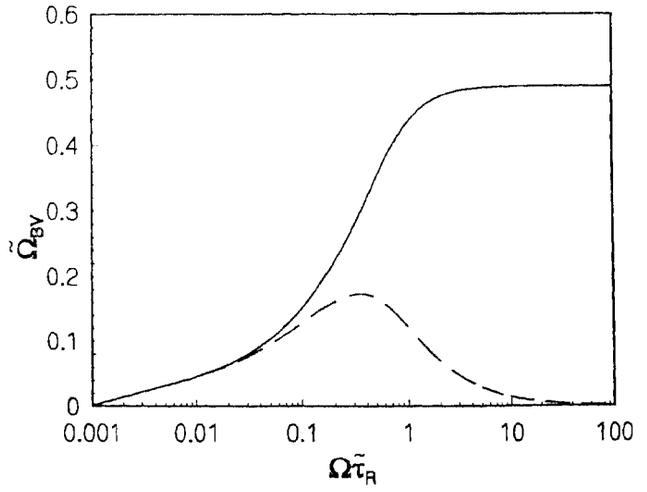

Figure 4.3: The variation of the real part (solid line) and the imaginary part (dashed line) of the effective Brunt-Väisälä frequency $\tilde{\Omega}_{\mathrm{BV}}$, (in dimensionless units) as a function of $\Omega\tilde{\tau}_R$.

time $\tilde{\tau}_R$. The solid line depicts the real part whereas the dashed line represents the

imaginary parts of $\tilde{\Omega}_{\rm BV}$. Note that for $\Omega\tilde{\tau}_R > 10$, $\tilde{\Omega}_{\rm BV}$ reaches a constant value of 0.5 (corresponding to the adiabatic limit). On the other hand, as $\Omega\tilde{\tau}_R \rightarrow 0$, Re($\tilde{\Omega}_{\rm BV}$) < 0.1. Thus in the isothermal limit, $\tilde{\Omega}_{\rm BV}$ which is the higher cutoff frequency for the $g-$ modes is very low, the consequences of this will be taken up again when we discuss the properties of $g-$ modes in detail. Figure 4.3 also reveals that the imaginary part of $\tilde{\Omega}_{\rm BV}$ is significant only for $\Omega\tilde{\tau}_R \sim 1$.

The general solution of equation (4.8) can be expressed in terms of Meijer functions (Zhugzhda 1979) as follows:

$$\xi_x^{(h)} = G^{12}_{2,4}\left(\mu_h, \begin{matrix} a_1 & , & a_2 \\ \mu_1, \cdots, \mu_i, & \cdots, & \mu_4 \end{matrix} \Big| \theta^2\right) \qquad (i,h = 1,\ldots,4;\ i \neq h)\,, \quad (4.9)$$

where

$$\mu_{1,2} = \frac{(1 \pm i\alpha)}{2}, \qquad \mu_{3,4} = \pm K\,, \tag{4.10}$$

$$a_{1,2} = \frac{(1 \pm \phi)}{2}\,, \tag{4.11}$$

$$\alpha = \sqrt{4\frac{\Omega^2}{\tilde{\gamma}} - 1}\,, \tag{4.12}$$

$$\phi = \sqrt{-\alpha^2 + 4K^2(1 - \tilde{\Omega}^2_{\rm BV}/\Omega^2)}\,. \tag{4.13}$$

These solutions are very similar in nature to the purely adiabatic case (see Appendix B). Once $\xi_x^{(h)}$ is known, it is fairly straightforward to determine the corresponding solutions $\xi_z^{(h)}$ from either of equations (4.4) or (4.5). The complete solutions satisfying the required boundary conditions can be constructed as linear combinations of $\xi_x^{(h)}$ and $\xi_z^{(h)}$.

4.3 Solutions for $K \rightarrow 0$

For physical reasons and also for the purpose of mode classification it is instructive to consider first the limiting case $K \rightarrow 0$. ¿From equations (4.4) and (4.5), we find that in the limit $K = 0$, ξ_x and ξ_z become decoupled. It is fairly straightforward to see that as $K \rightarrow 0$, there are two sets of solutions (HC):

$$\xi_x = c_1 J_0(2\theta) + c_2 Y_0(2\theta)\,, \qquad \xi_z = 0\,, \tag{4.14}$$

$$\xi_z = c_3\theta^{-1+i\alpha} + c_4\theta^{-1-i\alpha}\,, \qquad \xi_x = 0\,, \tag{4.15}$$

where $\alpha = (4\Omega^2/\tilde{\gamma} - 1)^{1/2}, c_i$ $(i = 1, 2, \ldots)$ are constants, and J_0 and Y_0 are the Bessel functions. The asymptotic limit of equation (4.14) corresponds to the slow MHD waves for arbitrary field strength and this solution is the same as in the case of purely adiabatic propagation. Thus the radiative diffusion does not affect the slow MHD waves discussed in Chapters 2 and 3. On the other hand, equation (4.15) represents a vertically propagating wave approximately when $|\Omega|$ exceeds the cutoff frequency Ω_c (which in dimensionless units is $\sqrt{|\tilde{\gamma}|}/2$). In the limit $\tau_R \to \infty$, Ω_c reduces to the adiabatic acoustic modes in an unmagnetized plasma. In the general case of a finite cooling time, the solutions of equation (4.15) are affected by the radiation field compared with the purely adiabatic case. The properties of these modes will be taken up in the next section.

4.4 Solutions for $K \to \infty$

In the limit $K \to \infty$, it can be easily seen that equations (4.4) and (4.5) reduce to the following differential equation (Moreno-Insertis and Spruit 1989; see also HC)

$$\frac{\mathrm{d}^2\xi_z}{\mathrm{d}z^2} - \frac{1}{H}\frac{\tilde{c}_T^2}{\tilde{\gamma}c_S^2}\frac{\mathrm{d}\xi_z}{\mathrm{d}z} + \frac{1}{H^2}\frac{c_S^2}{c_T^2}[\Omega^2 - \frac{c_T^2}{v_A^2}(\tilde{\Omega}_{BV}^2 + \frac{c_T^2}{\gamma\tilde{\gamma}c_S^2})]\xi_z = 0, \tag{4.16}$$

where $\tilde{c}_T$ denotes the complex tube speed given by

$$\tilde{c}_T^2 = \frac{\tilde{\gamma}c_S^2 v_A^2}{\tilde{\gamma}c_S^2 + v_A^2}\,. \tag{4.17}$$

When $c_S/v_A \gg 1$, $c_T \to v_A$ and equation (4.16) becomes

$$\frac{\mathrm{d}^2\xi_z}{\mathrm{d}z^2} + \frac{1}{H^2}\frac{c_S^2}{v_A^2}(\Omega^2 - \tilde{\Omega}_{BV}^2)\xi_z = 0\,. \tag{4.18}$$

equation (4.18) admits the solutions

$$\xi_z = d_1 J_0(\psi) + d_2 Y_0(\psi)\,, \tag{4.19}$$

where d_1 and d_2 are constants and

$$\psi = 2\frac{\theta}{\Omega}\sqrt{\Omega^2 - \tilde{\Omega}_{BV}^2}\,. \tag{4.20}$$

For propagating wave solutions, $\Omega > \tilde{\Omega}_{BV}$. Such solutions correspond essentially to MHD waves, modified by gravity. They will be discussed in greater detail in §4.5.1.1.

4.5 Normal modes in a weak magnetic field

4.5.1 Rigid boundary condition

We now determine the normal modes of a stratified atmosphere including nonadiabtic effects (approximated by Newton's law of cooling). We examine the same atmospheric modes as studied in Chapters 2 and 3.

To calculate the normal modes of the system let us first consider rigid boundary conditions, *viz.*

$$\xi_x = \xi_z = 0 \quad \text{at} \quad z = 0 \quad \text{and} \quad z = d\,. \tag{4.21}$$

The asymptotic properties of the solution in the purely adiabatic limit are presented in Appendix B. Following the same line of treatment using equations (4.9)–(4.13) and applying the boundary conditions given by equation (4.21) one can derive the following dispersion relation in the weak field limit

$$\begin{aligned}(\frac{\Omega^2}{\tilde{\gamma}} - K^2)\sin\tilde{\theta}\sin(K_z D) \;=\; & 2\sqrt{\tilde{\gamma}}\frac{\epsilon}{\Omega}e^{D/4}\Big\{K_z K^2[\cosh(D/4)\cos\tilde{\theta}\cos(K_z D) - 1] \\ & + \sinh(D/4)\cos\tilde{\theta}\sin(K_z D)[M(\frac{\Omega^2}{\tilde{\gamma}} - K^2) - K^2(\frac{1}{\gamma\tilde{\gamma}} - \frac{1}{2})]\Big\} + O(\frac{\epsilon^2}{\Omega^2}),\end{aligned} \tag{4.22}$$

where K_z^2 is given by

$$K_z^2 = \frac{\Omega^2}{\tilde{\gamma}} - K^2(1 - \frac{\tilde{\Omega}_{BV}^2}{\Omega^2}) - \frac{1}{4}\,, \tag{4.23}$$

and

$$M = K^2\frac{\tilde{\Omega}_{BV}^2}{\Omega^2} - \frac{1}{16}\,. \tag{4.24}$$

For $\epsilon << \Omega$, the dispersion relation to lowest order in ϵ/Ω becomes

$$(\frac{\Omega^2}{\tilde{\gamma}} - K^2)\sin\tilde{\theta}\sin(K_z D) \;=\; 0\,. \tag{4.25}$$

equation (4.25) admits the following solutions

$$\sin(K_z D) \;=\; 0\,, \tag{4.26}$$

$$\sin\tilde{\theta} = \; 0\,, \tag{4.27}$$

$$\Omega = \sqrt{\tilde{\gamma}}\;K. \tag{4.28}$$

We first consider the solution given by equation (4.26) which implies that $K_z D = n\pi$, where n is an integer and denotes the order of the mode. Using this condition equation (4.23) yields,

$$\frac{\Omega_i^4}{\tilde{\gamma}} - \Omega_i^2(K_i^2 + \frac{1}{4}) + K^2\tilde{\Omega}_{\rm BV}^2 = 0 \qquad (i = p, g)\,, \tag{4.29}$$

where $K_i^2 = K_z^2 + K^2$. Note that equation (4.29) looks very similar to the usual relation for $p-$ and $g-$ modes (see Eq. 2.36) apart from the factor $\tilde{\gamma}$ and modified $\tilde{\Omega}_{\rm BV}$. Because of the presence of these two factors, properties of these modes have changed drastically. Figures 4.4a,b give an overview of the behavior of the $g-$ and $p-$ type modes respectively. Their properties are reflected in these two $K-\Omega$ diagrams produced by solving equation (4.29) for different values of the relaxation time $\tilde{\tau}_R$. Figure 4.4a clearly shows that the g_1- mode has been pushed down to the low frequency part of the diagnostic diagram with decreasing value of $\tilde{\tau}_R$. As $\tilde{\tau}_R \to 0$, the g_1- mode tend to disappear, because $\tilde{\Omega}_{\rm BV} \to 0$. On the other hand, Figure 4.4b shows that inclusion of radiative exchange has not greatly changed the behavior of the p_1- mode, apart from a decrease of the acoustic cutoff frequency.

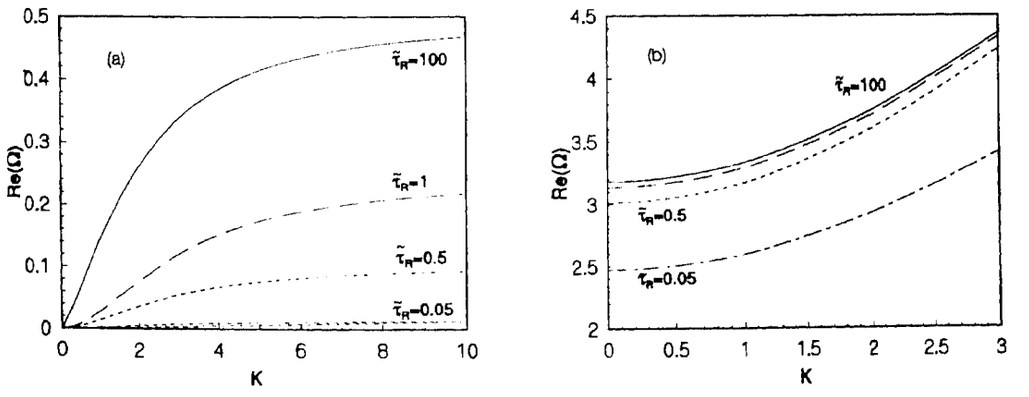

Figure 4.4: Diagnostic diagram for non adiabatic modes. Panel (a) for g_1- mode and (b) for p_1- mode. Different line styles correspond to different radiative relaxation time $\tilde{\tau}_R$ as labeled.

The solution corresponding to equation (4.28) can be recognized as a modified Lamb mode (compare with Eq. [2.33]). Thus we expect a frequency shift of the adiabatic Lamb mode. Consequences of this frequency shift will be taken up later. Turning our attention to the solution given by equation (4.27), we find that these modes are the same magnetic

modes present in the adiabatic conditions. Thus these slow modes are not affected by the inclusion of radiative losses in the weak field limit. This result complements the result of Bogdan & Knölker (1989), where it was conjectured that the uniform magnetic field reduces the temperature perturbations associated with these waves and therefore suppresses the radiative damping of these disturbances. This aspect will taken up later when we discuss the numerical solutions.

4.5.1.1 Numerical results

The behavior of the MAG waves is reflected in their properties in the $K-\Omega$ diagram. Figures 4.5 a,b show respectively the variation of the real and imaginary part of the complex frequency with horizontal wave number K, for $\tilde{\gamma}_R = 0.05$. The solutions were obtained by solving the equation (4.8) numerically, using a complex version of the Newton-Raphson-Kantorovich scheme (Cash and Moore, 1980). The atmosphere is characterized by $D = 1, \epsilon = 0.01$, and $\gamma = 5/3$. Figure 4.5 depicts a portion of the $K-\Omega$ diagram for $\Omega < 0.5$ where the magnetic modes are strongly influenced by the Lamb mode. The short-dashed curve represents the purely adiabatic Lamb mode, whereas the long-dashed curve represents the non-adiabatic Lamb mode solution given by $\Omega = \sqrt{\tilde{\gamma}}K$. Figure 4.5 also reveals that the frequency of the Lamb mode is changed due to damping. The separate dispersion relations for individual modes (Eqs. [4.26] -[4.28]) enable us to identify the elementary wave modes and discern the effects of radiative heat exchange on the general properties of the modes. Firstly, the real parts of the frequencies of the magnetic modes are not affected by the inclusion of radiative losses, as expected from asymptotic solutions (Eq. [4.27]). However, the avoided crossings have shifted because the pure Lamb mode has been modified. Another interesting feature, shown in Figure 4.5b, is that we have a substantial increase in the imaginary part of the frequency in that portion of the $K-\Omega$ diagram where there is an avoided crossing between the modified Lamb mode and the magnetic modes. It appears that damping is enhanced in those parts of the $K-\Omega$ plane where the modes behave predominantly as Lamb mode. The even ordered $m-$ modes, which behaves predominantly as a magnetic mode starts out with comparatively low $\mathrm{Im}(\Omega)$. At the avoided crossing of $\mathrm{Re}(\Omega)$, the two modes exchange their nature, leading to a crossing of the imaginary parts of the frequencies.

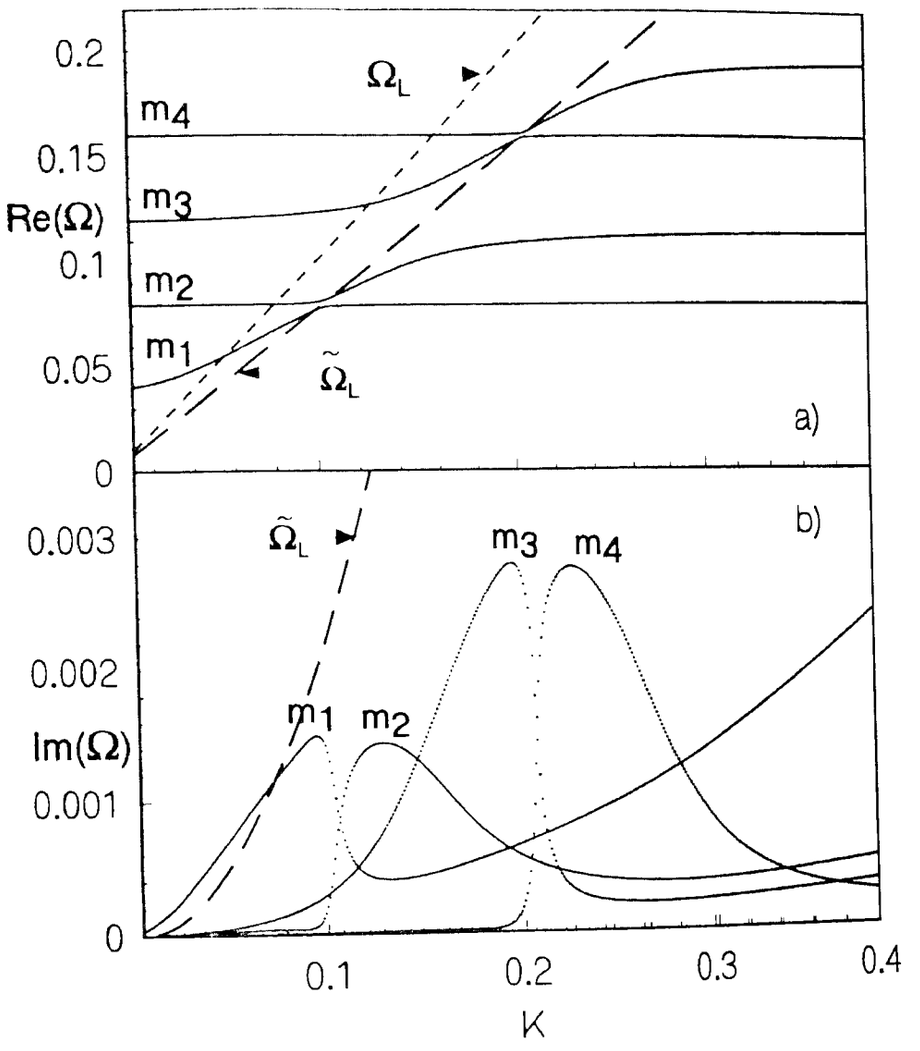

Figure 4.5: Variation with K of the (a) real (solid lines) and (b) imaginary (dotted lines) parts of the frequency. An expanded region of the diagnostic diagram has been chosen to focus on the interaction between the magnetic modes with the Lamb mode, for a dimensionless radiative relaxation time $\tilde{\tau}_R = 0.05$. In panel (a) the short dashed curve represents the adiabatic Lamb solution $\Omega = K$ and the long dashed curve represents the non-adiabatic Lamb solution $\Omega = \sqrt{\tilde{\gamma}}K$.

The alternation between narrow and broad avoided crossings of the real part of Ω in Figure 4.5a gives rise to an asymmetry in the behavior of the imaginary part of Ω as a given mode changes between being predominantly a $m-$mode and a Lamb-mode. This is closely analogous to the results of the asymptotic analysis of Chapter 2, concerning the behavior in the vicinity of nearly degenerate modes: in the present case of nonadiabatic wave propagation, we again find that 'even' crossings are typically much narrower than the 'odd' crossings.

A striking difference, compared with the adiabatic case, is the lack of an upturn in Ω (in Fig. 4.5a) as a function of K for the m_1- mode at the highest K considered (compare with Figure 5 of HC). As discussed in HC, this upturn probably arises because of the interaction with the lowest-order $g-$ mode; otherwise, the low-frequency $g-$ modes, with frequencies below the m_1- mode, appear to be eliminated. With Newtonian cooling, the effective Brunt-Väisälä frequency, given by $\tilde{\Omega}_{\rm BV}^2 = (\gamma^* - 1)/\gamma\gamma^*$ (in dimensionless units), decreases with decreasing τ_R and is zero for $\tau_R = 0$. The same is therefore true of the frequencies of pure (*i.e.*, non-magnetic) $g-$ modes. Indeed, in the case of a non-magnetic atmosphere it was shown (Mihalas and Mihalas, 1984; Bünte and Bogdan, 1994) that if cooling occurs on a sufficiently short time scale, gravity waves cannot exist. Physically, this is not surprising: the buoyancy force that drives gravity waves, arises solely from horizontal temperature fluctuations, which vanish when $\tau_{\rm R} \rightarrow 0$. This explains the lack of effect of the $g-$ mode interaction in Figure 4.5a; indeed, we note that the real part of $\tilde{\Omega}_{\rm BV}$, evaluated at $\Omega = 0.5$, is about 0.072 for this value of $\tilde{\tau}_{\rm R}$. We conjecture, however, that the comparatively rapid increase of the imaginary part of the frequency of the m_1- mode with K (in Fig. 4.5b) might be related to a beginning influence of the low-frequency $g-$ modes for larger values of K. Now let us increase the the value of $\tilde{\tau}_R$ and look for the influence of the $g-$ modes. Figure 4.6 shows the low frequency part of the K-Ω diagram for large values of K, with $\tilde{\tau}_R = 0.5$ (compare with Fig. 5b of HC). Now we can observe the upturn in Ω as a function of K for the low ordered magnetic modes at large K. This clearly indicated the influence of the $g-$ modes as expected. The $m-$ modes begin to acquire a $g-$ like character for $K >> \Omega$. For moderate K, the various modes, corresponding to solutions of equations (4.26) –(4.28), become decoupled. As a result, the solution neither

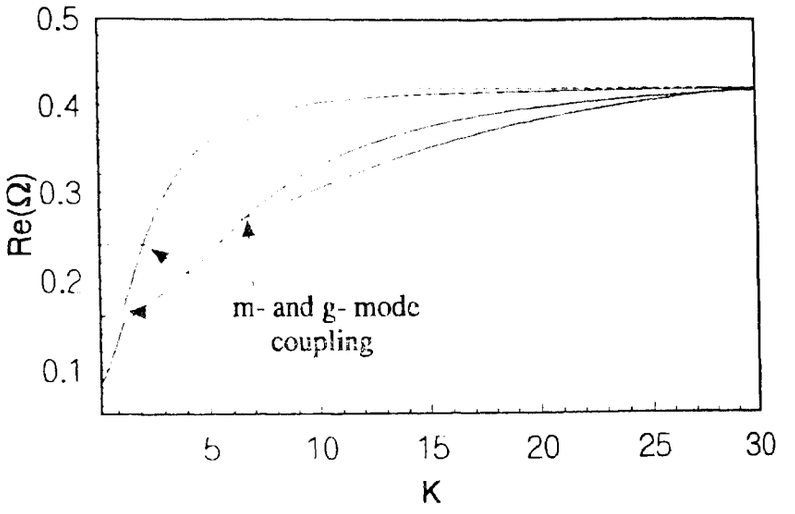

Figure 4.6: Diagnostic diagram showing the interaction between the magnetic modes with gravity modes, for a dimensionless radiative relaxation time $\tilde{\tau}_R = 0.5$ at moderate to large K.

resemble pure $m-$ modes nor pure $g-$ modes, but a combination of the two. As K is increased further, there is a tendency for the lowest modes to run in parallel with a small frequency separation, similar to the behavior in the purely adiabatic case (see Fig. 2.3b). We might note that superficially similar phenomenon have been obtained amongst the energy levels of hydrogen atom in a magnetic field (Friedrich and Wingen, 1989). The striking effect of finite $\tilde{\tau}_R$ is the frequency shift of the Ω_{BV}, which marks the upper bound on the $g-$ mode frequencies in the non-magnetic case. Figure 4.6 reveals that this upper bound has shifted to around $\Omega = 0.42$ for $\tilde{\tau}_R = 0.5$, as compared to the adiabatic case, where $\Omega_{BV} = 0.49$ for $\gamma = 5/3$ (see Fig. 5 of HC). This result is in agreement with the analytic solution discussed in §4.4. Let us concentrate on the magnetic mode and the modified Lamb-mode interaction in Figure 4.7a for different values of $\tilde{\tau}_R$, the dashed line representing the pure adiabatic Lamb mode. This shows the effect of different relaxation time scales on the modes. As $\tilde{\tau}_R$ increases, *i.e.*, as we approach the adiabatic limit, the avoided crossing shifts towards the left and the modified magnetic mode approaches the dashed line (behaves more as a pure adiabatic Lamb mode). Hence the general effect of a finite cooling time is the shift of the avoided intersection point. It is instructive to consider a single mode, which we choose as the

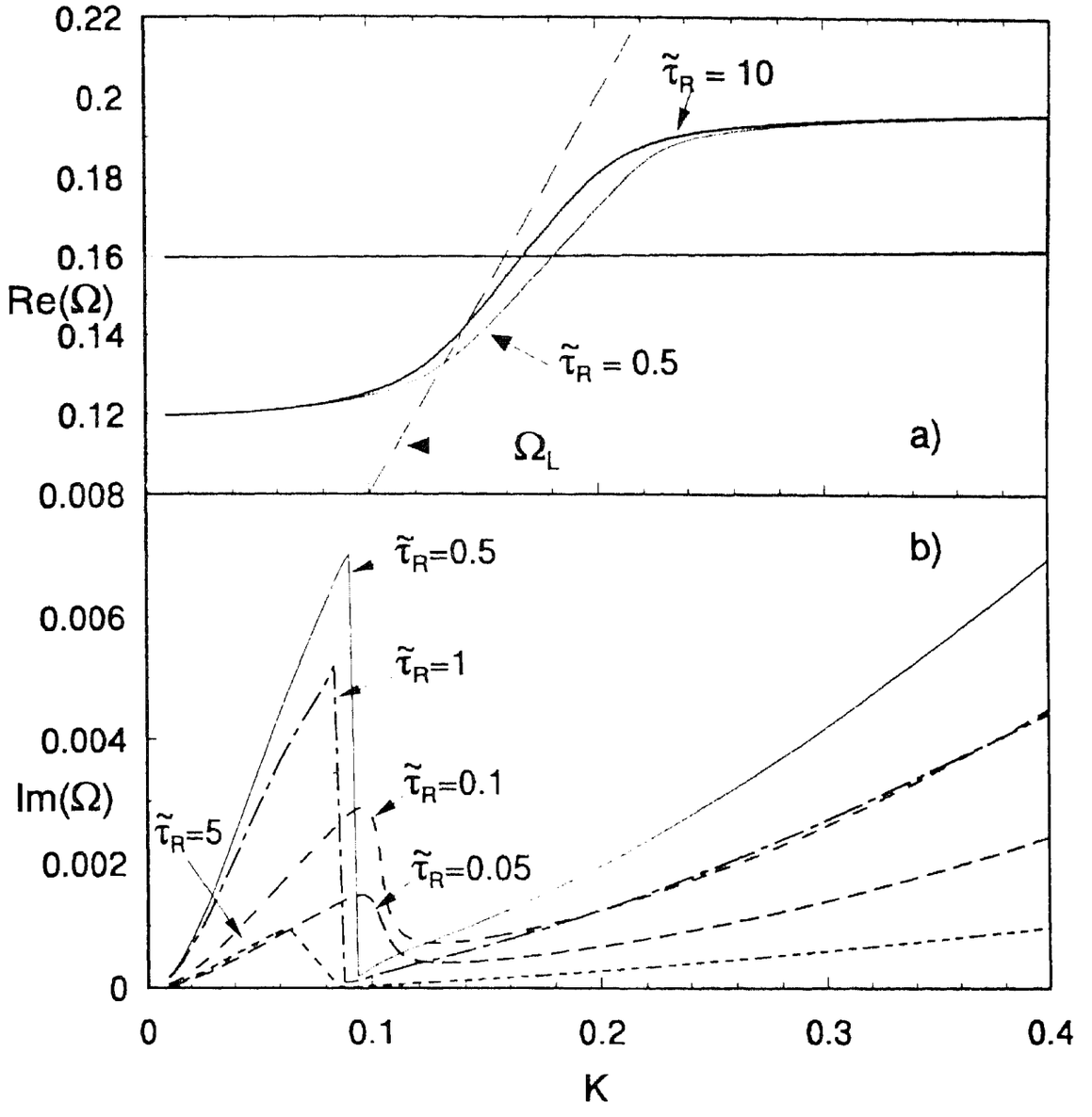

Figure 4.7: Region of interaction between m- and Lamb-type solutions for different values of $\tilde{\tau}_R$ as labeled. Variation of (a) real part and (b) imaginary part of the frequencies with K.

first magnetic mode m_1-, and follow its behavior as it interacts with the Lamb mode. Figure 4.7b depicts the variation with K of the imaginary part of the complex frequency, for different values of $\tilde{\tau}_R$. The figure clearly reveals that for $\tilde{\tau}_R > 5$ and $\tilde{\tau}_R < 0.05$ the imaginary part of Ω approaches zero, which further indicates that in these limits there is no dissipation. However, for intermediate values of $\tilde{\tau}_R$ there is mode damping. As seen above, the damping is largest where the modes take on the nature of a Lamb mode in the avoided-crossing regions. Another interesting feature is that in the range $0.05 < \tilde{\tau}_R < 5$ we have a considerable increase in the imaginary part of Ω for large values of K; as before, this indicates a growing coupling between $g-$ modes and the $m-$ modes which allows the modes to decay faster.

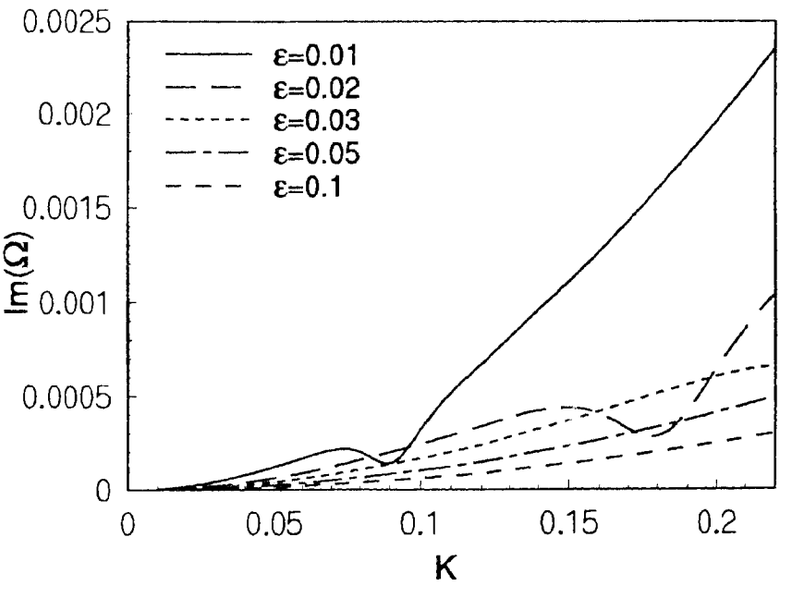

Figure 4.8: Variation of the imaginary part of Ω with K for $\tilde{\tau}_R = 0.5$. The different line styles corresponds to different ϵ values (which is a measure of magnetic field strength) as labeled.

Now we turn our attention to the effect of the strength of magnetic field on the damping of these waves. To delineate the influence of the magnetic field, we choose the m_2- mode, which is predominantly magnetic in nature. Figure 4.8 shows the variation of the imaginary part of frequency (which is a measure of the damping) with K for fixed $\tilde{\tau}_R = 0.5$. The different line styles corresponds to different ϵ values. It clearly reveals

that as we increase the value of ϵ (increasing magnetic field strength) the imaginary part reduces, indicating less damping of these wave modes. This result is in agreement with the conclusions drawn by Bogdan and Knölker (1989), that the magnetic field suppresses radiative damping. For horizontal magnetic field Bünte and Bogdan (1994) have also reported a "stiffening" of the atmosphere with increasing ϵ values.

4.5.2 Zero-gradient boundary condition

If we use zero-gradient boundary condition (Eq. [2.29]), in addition to all these modes we find another wave mode, namely the gravity-Lamb mode. The dispersion relation for this mode is given by

$$K_z^2 + \frac{1}{4} = 0 \,. \tag{4.30}$$

Combining equation (4.30) with (4.23) yields

$$\Omega^4 - \tilde{\gamma}\Omega^2 K^2 + \tilde{\gamma} K^2 \Omega_{\rm BV}^2 = 0 \,. \tag{4.31}$$

This equation has the solution

$$\Omega^2 = \frac{\tilde{\gamma} K^2}{2} \left[1 \pm \left(1 - 4 \frac{\tilde{\Omega}_{\rm BV}^2}{K^2 \tilde{\gamma}} \right)^{1/2} \right] . \tag{4.32}$$

The solution resembles a modified gravity mode on the lower branch and a Lamb mode on the upper branch. In order to see this, consider the limit $K \to \infty$. The smaller solution in equation (4.32) has the limit $\Omega \simeq \tilde{\Omega}_{\rm BV}$, which is the dispersion relation for a modified $g-$mode for large K; the larger solution has the limit $\Omega \simeq \sqrt{\tilde{\gamma}} K$ for large K, which shows that the mode behaves like a modified Lamb wave.

Thus the separate modes have changed their behavior in the diagnostic diagram in the non adiabatic case. It is important to know how these modified modes interact with one another in the presence of radiative losses. Mode coupling in the non adiabatic case will be different as compared to the adiabatic case studied in Chapters 2,3. In fact the right hand side of equation (4.22) contributes to the coupling

Let us now consider the moderate magnetic field strength case, Figure 4.9 shows a region in the diagnostic diagram for $\epsilon = 0.1$ ($B \sim 240$ G) and $\tilde{\tau}_R = 0.5$, subject to the zero-gradient boundary condition (compare this figure with Fig. 2.8b). The mode

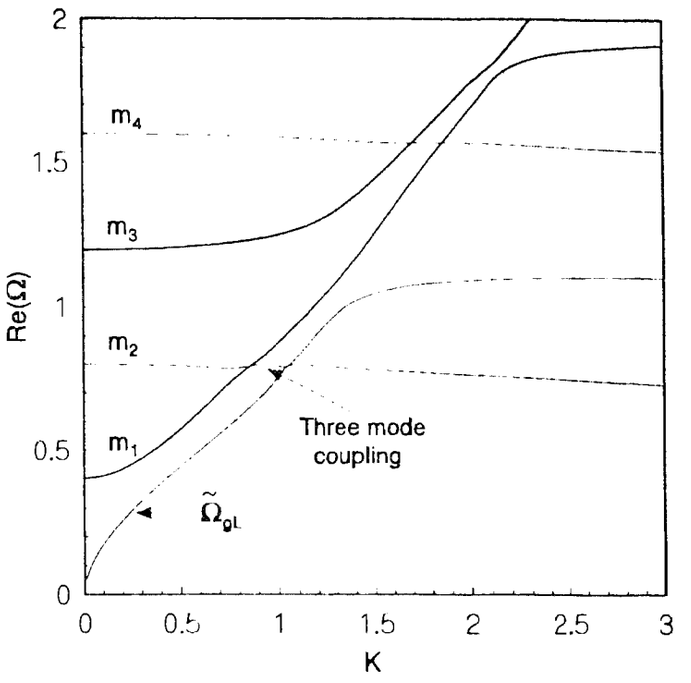

Figure 4.9: Region in the diagnostic diagram for moderate field strength ($\epsilon = 0.1$) and $\tilde{\tau}_R = 0.5$, where there are modified Lamb mode, magnetic mode and gravity-Lamb mode as indicated. Results for zero gradient boundary conditions.

coupling in this case is much more complicated because we have three mode interaction regions as indicated.

As K increases, the m_1- mode begins to acquire the character of a modified Lamb mode as before. Figure 4.10 a, which shows the variation of imaginary part of the frequency of the m_1- mode with K also reveals that, there is an enhancement as it approaches an avoided crossing (near $K = 0.8$) followed by a suppression due to mode transformation. Upto $K = 0.8$ this mode behaves as a magnetic Lamb mode and after the mode transformation it becomes a magnetic type. This process is repeated at higher frequency (around $K = 2$). Note the large drop due to magnetic field suppression. Figure 4.10 b shows the variation of imaginary part of the frequency of the m_2- mode (of Fig. 4.9) with K. The two peaks corresponds to modified Lamb and $m-$ mode coupling and modified $gL-$ and $m-$ mode coupling respectively. Note the steep rise of the imaginary component after the avoided crossing which indicates the effect of

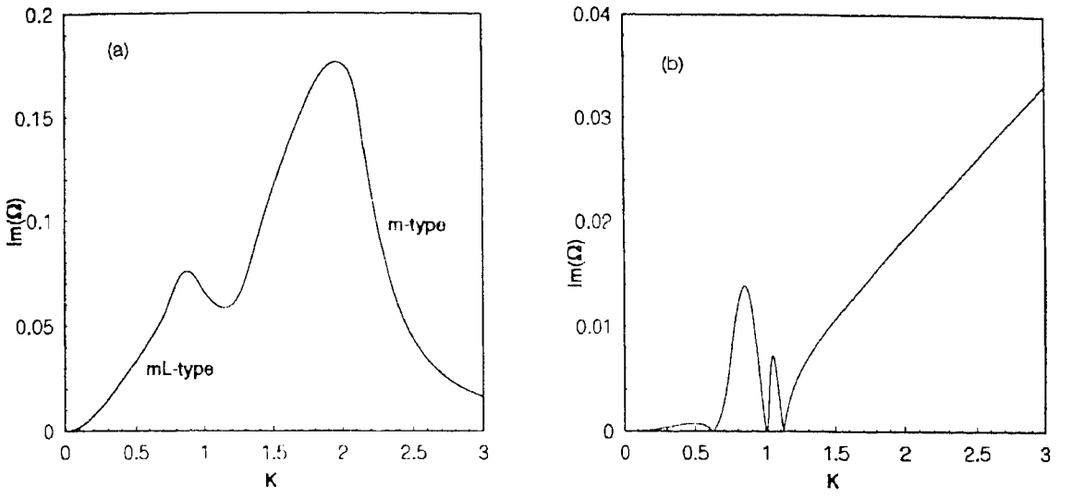

Figure 4.10: Variation of the imaginary part of Ω with K for moderate field strength ($\epsilon = 0.1$) and $\tilde{\tau}_R = 0.5$ Panel (a) shows the m_1- mode and panel (b) the m_2- mode.

gravity mode. Figure 4.9 also shows the lower branch of the modified gravity-Lamb mode (indicated as $\tilde{\Omega}_{gL}$) which was absent in Figure 2.8b.

4.6 High magnetic field case

We now consider a situation which is more realistic as far as the solar atmosphere is concerned. We consider an isothermal atmosphere extending over several scale heights for which $v_A \gg c_S$ over most of the atmosphere. This situation is somewhat similar to the atmosphere in sunspots.

It is well known that periods of oscillations above a sunspot's umbra range between 100 and 200 s. Upto now, a lot of new measurements in different spectral lines have been made (Thomas *et al.* 1984, 1987; Gurman, 1987; Alisandrakis *et al.* 1992). Recent observations (Kentischer and Mattig, 1995) of umbral oscillations in the middle and upper chromosphere show pronounced power at frequencies between 5 and 9 mHz. They conclude that the first peak at 5.9 mHz consists mainly of upward propagating waves traveling with sound speed. There are indications that these waves have their origin in the photospheric resonator. The second distribution is located at 7.5 mHz and oscillations involved here are standing waves which are confined to the chromosphere (chromospheric resonator).

The primary concern is to examine the effects of Newtonian cooling on the normal modes of an isothermal atmosphere including radiative losses. We have seen from previous studies (Hasan, 1991; Wood, 1990; see also Chapter 3) that the slow magnetoacoustic modes or $p-$ modes are the most important wave mode for carrying energy to the upper atmosphere. We will concentrate on the properties of this mode and will also study its interaction with other modes.

The frequencies of the slow magnetoacoustic modes or $p-$ modes can be found from equation (4.29) with $K = 0$, *i.e.*

$$\Omega_{p,n} = \sqrt{\tilde{\gamma}\left(\frac{n^2\pi^2}{D^2} + \frac{1}{4}\right)}\,, \tag{4.33}$$

where n denotes the order.

Table 4.1 represents the eigenfrequencies of different order $p-$ modes from our model atmosphere with $D = 10$, $\tilde{\tau}_R = 0.5$ and $\epsilon = 0.84$ ($B \sim 2$ kG). The relation between the horizontal wave number and radius of the flux tube has already been discussed in Chapter 2 (see §2.6.2). Table 4.1 reveals that radiative cooling shifts the eigenfrequencies away from the real axis. Note that the computed frequencies match very well with the ones calculated from expression (4.33). Also note that the p_2- mode has a period of 136 s in the presence of radiative losses, this value is very close to the observed peak at 7.5 mHz (Period 134 s) by Kentischer *et al.* (1995). This observation was reported at layers near the temperature minimum which correspond to about 1000 km over the photosphere (D = 10, in our notation).

	Adiabatic case ($\tilde{\tau}_R = 100$)			Radiative case ($\tilde{\tau}_R = 0.5$)			Isothermal case ($\tilde{\tau}_R = 0.05$)		
Mode	Re(Ω)	Im(Ω)	P(S)	Re(Ω)	Im(Ω)	P(S)	Re(Ω)	Im(Ω)	P(S)
p_1	0.5903	0.0007	164	0.5203	0.0658	186	0.458	0.0125	211
p_2	0.803	0.0009	120	0.7075	0.0895	136	0.624	0.017	155
p_3	1.07	0.0013	90	0.94	0.119	103	0.828	0.0227	117

Table 4.1: Eigenfrequencies of different order $p-$ modes for a model atmosphere with $D = 10, B = 2kG, \tilde{\tau}_R = 0.5$ and $K = 0.1$.

Radiative cooling leads to a temporal decay of oscillations of the form $\exp(-t/\tau_D)$. The frequency eigenvalues of the four modes are listed in Table 4.2 for different mag-

netic flux tubes together with the ratio of characteristic decay time τ_D =Im$(\omega)^{-1}$ and oscillation period = 2π/Re(ω). One should not attach a great deal of significance to any flux tube model (see Table 4.2); rather these structures have been chosen to illustrate a wide variety of possibilities. In the presence of Newtonian cooling all four

Structure	K	Radius (km)	Re(Ω)	Im(Ω)	P(S)	τ_D(S)	τ_D/P
Sunspot...	0.06	5000	0.520	0.0659	186	233	1.25
			0.605	0.0767	160	200	1.25
			0.706	0.089	137	173	1.26
			0.820	0.104	118	148	1.25
Magnetic knot..	0.37	850	0.52	0.0682	186	226	1.21
			0.604	0.080	160	192	1.20
			0.704	0.089	137	173	1.26
			0.819	0.103	118	149	1.27
Magnetic element..	1.57	200	0.523	0.067	185	230	1.24
			0.608	0.078	159	197	1.24
			0.709	0.091	136	169	1.24
			0.821	0.104	118	148	1.25

Table 4.2: Eigenfrequencies (corresponding to different magnetic structures) of different $p-$ modes for a model atmosphere with $D = 20, B = 2\text{kG}, \tilde{\tau}_R = 0.5$.

modes are damped by a factor e^{-1} within two oscillation periods. Let us now find out the importance of mode coupling on mode damping. Table 4.3 shows eigenvalues of two coupled modes for a model atmosphere with $D = 10$, $\tilde{\tau}_R = 0.5$ and $B = 2\text{kG}$. It shows that the coupled modes are heavily damped. Thus mode coupling enhances the damping.

Mixed mode	K	Radius (km)	Re(Ω)	Im(Ω)	P(S)	τ_D/P
p_1 & MgL	0.85	370	0.536	0.09	180	0.95
p_2 & MgL	0.7	450	0.6723	0.11	144	0.96

Table 4.3: Eigenfrequencies of different mixed modes for a model atmosphere with $D = 10, B = 2\text{kG}, \tilde{\tau}_R = 0.5$.

4.7 Conclusions

We have presented new solutions for magnetoatmospheric waves in an isothermal atmosphere with a vertical magnetic field in the presence of radiative heat exchange based on Newton's law of cooling. Radiation can radically alter the dynamical properties of wave modes in a fluid. This radiative heat exchange gives rise to a temporal decay of oscillations with a characteristic dimensionless decay time $\tilde{\tau}_{\rm D} = 1/\ \Omega_{\rm I}$, where $\Omega_{\rm I}$ is the imaginary part of Ω. Depending on the value of the radiative relaxation time $\tilde{\tau}_{\rm R}$, the modes are effectively damped by the radiative dissipation in as short a time as two oscillation periods; however, in the limits of very large or very small $\tilde{\tau}_{\rm R}$, corresponding to nearly adiabatic or nearly isothermal oscillations, the modes are essentially undamped. The existence of mode damping in the presence of radiative exchange is hardly surprising; however, a new feature of our analysis is that the damping is significantly enhanced by the mode coupling in the regions of avoided crossing. For small-scale magnetic structures on the Sun, such mechanisms might be very important for wave leakage.

Now we would like to critically evaluate the merits and demerits of using Newton's law to model heat exchange. At sufficiently low frequencies, the wavelength of a disturbance is so long, that it becomes optically thick (no matter how transparent the material is), and the Newtonian cooling approximation no longer holds. Conversely, at high frequencies the wavelength of a disturbance becomes so small that it is optically thin (no matter how opaque the material) and the Newtonian approximation holds good. Bünte and Bogdan(1994) have already pointed out that radiative effects on oscillations in photospheric and higher layers are clearly important. Radiative dissipation based upon Newton's cooling law is clearly an oversimplification of the problem; nevertheless it allows us to assess the effects of radiative damping on the modal structure. It also enables us to look at the full frequency spectrum and the interaction amongst various modes.

One should bear in mind that in a nonisothermal atmosphere, the use of the Newtonian cooling approximation provides a simple but unfortunately inconsistent method for studying the interaction between linear waves and the radiation field. Part of the inconsistency arises from the fact that we consider wave propagation in medium which is

not in radiative equilibrium. The physical mechanisms that determine the temperature structure is still largely unknown.

We expect this study to contribute to the investigation of heating in active regions. The present comprehensive treatment based on an asymptotic analysis allows us to understand the behavior of the normal modes in the presence of radiative heat exchange.

Chapter 5

Concluding Remarks

In this Chapter we summarize the important findings of the thesis with a brief outlook on future projects. This Chapter is divided into two subsections corresponding to the two parts of the thesis *viz.*, Energy transport to the solar corona by magnetic kink waves and magnetoatmospheric wave propagation in the solar atmosphere. In the first part we take resort to thin flux tube approximation and in the later our analysis pertains to homogeneous fields. The main thrust of our investigation is to examine the physics of wave propagation in a stratified atmosphere with a vertical magnetic field. It is also one of our objectives to examine the modal structure and see how it is influenced by field.

5.1 Magnetic kink waves

It is known for a number of years that the magnetic flux tubes acts as "windows" to the solar atmosphere, through which the wave energy generated in the solar convection zone is carried by various types of waves (longitudnal, transverse and torsional - see Spruit 1982). In the first part of the thesis we show that the magnetic kink waves generated by the motions of photospheric footpoints of the coronal flux tubes can supply adequate energy for heating the corona. Though footpoint motions with granular time and velocity scales may not be sufficient for providing adequate energy, observations clearly show that horizontal velocities as large as 3 km/s occur in the solar photosphere (Muller *et al.* 1994). Velocities of this magnitude or higher has also been reported by Berger and Title (1996). A rough estimate of generated wave energy flux by Muller *et al.* (1994) also demonstrate that the amount of wave energy available for heating is sufficient

to sustain the mean level of the observed radiative losses from the corona. These observations are also found to be in good agreement with recent theoretical advances. Time-dependent numerical simulations of the solar convection zone (Norduland and Dravins 1990; Cattaneo *et al.* 1991; Steffen 1993) indicates the presence of motions with horizontal velocities larger than 2 km/s near the top of the solar convection zone.

Another assumption in our analysis is to neglect the non-linearities which must become important in the higher regions where the amplitudes are large. One should calculate the wave energy fluxes in the non-linear regime. Ulmschneider *et al.* (1991) have shown numerically that the excited transverse tube waves are non-linear. Some portions of their energy will be transformed to longitudnal tube waves via the process of non-linear mode coupling. In general, this process may lead to damping of transverse tube waves during the propagation along magnetic flux tube and to heating of the local medium. We conjecture that this problem can be handled analytically in the non-linear regime. In that case the flux carried by the non-linear waves could be of the order of 10^9 ergs/ cm^2 s which can account for the observed enhanced heating in the chromospheric network. We hope to study this in near future.

One more assumption in our calculation is to neglect the merger of the neighboring flux tubes above the chromosphere (Spruit 1984). We wish to look at this aspect also in a future study.

5.2 Magnetoatmospheric waves

The second part of the thesis deals with the MAG wave propagation in a stratified isothermal atmosphere permeated by vertical magnetic fields. In Chapter 2 we concentrate on the effects of magnetic field on solar oscillations. On the basis of quantitative calculations, our analysis has brought out many features of waves in a stratified media. For the most general case, the problem of mode classification is extremely difficult, especially when v_A/c_S changes by several orders of magnitude over the vertical extent of the atmosphere. The stratification causes variation in the structure, which leads to mode conversion; hence when analyzing MAG waves in terms of elementary modes, one should bear in mind that their behavior described in this way may be a local property. We have largely concentrated on weak field limit, when $v_A \ll c_S$ throughout the layer.

The advantage of our asymptotic analysis is that it enables us to obtain the normal modes of the system. The general solutions involving Meijer functions are complicated and provide few clues about the physical nature of the waves. We have derived a dispersion relation which allows us to understand the nature of the modes and construct the $K - \Omega$ diagram. The insight gained from the asymptotic analysis in the weak field limit has proved useful in extending the computations from the moderate to strong field case.

Our solutions do not exhibit accidental degeneracy when frequencies of different modes approach each other. This can be explained while looking at the dispersion relation. At such frequencies the lowest order approximation breaks down and the higher order terms, which couple the modes have to be considered. This coupling is responsible for avoided crossings.

The new feature of our analysis is the occurance of an additional mode, namely the magneto-gravity-Lamb mode. To our knowledge, the identification and interaction of this mode has not been done carried out earlier. We find the relevance of this mode in umbral oscillations.

The present calculations also demonstrate that the change of boundary conditions has a striking effect on the mode coupling between different modes. The zero-displacement boundary conditions provide real solutions for the frequency Ω at all wavenumber K; in contrast, calculations with zero-gradient boundary conditions at both or one of the boundaries lead to complex conjugate pairs of roots for Ω, when K is in the vicinity of some avoided crossings. We explain this behavior in terms of an asymptotic analysis near the avoided crossings.

To understand the physical details of this we concentrate on the behavior of the modes near avoided crossings in Chapter 3. It appears that the boundary conditions permit the phase relationship between the modes to be changed in a manner so as to allow the wave to leak out from the boundary, thereby leading to a loss of energy from the cavity. We explore the implications of this kind of wave leakage from a adiabatic system, where no explicit energy loss mechanism is not taken into account, in context of umbral oscillations. We conjecture that the observed peaks at different frequencies (Abdelatif *et al.* 1986), could be due to mode coupling between different modes. We

explicitly show that without taking any non-adiabatic effects into consideration, the mixed modes present in magnetic structures can decay within two oscillation period because of mode coupling. The variations of eigenfunctions and various components of energy densities associated with a single mode allow us to study the general behavior of the individual and coupled modes and thereby enable us to identify potential candidates for heating the outer atmosphere.

Oscillations in a realistic stellar atmosphere are affected by radiative dissipation and energy loss at the boundaries. So it is natural to include some non-adiabatic effects into our theory of MAG wave propagation. Following Bünte and Bogdan (1994), we incorporate Newton's law of cooling through introduction of a complex ratio of specific heats, as indicated by equation (4.3). In the weak field limit, we derive a dispersion relation which allows to study the effect of radiative dissipation on the normal modes of the system. A finite Newtonian cooling time leads to complex frequency eigenvalues and hence the oscillation decay in time. A significant contribution of our analysis is to show that the mode coupling alters growth of mode damping. In places of $K - \Omega$ diagram it enhances the mode damping, whereas in some places it suppresses damping. We explicitly show that the presence of magnetic modes suppresses radiative dissipation. This result is in agreement with the conclusion drawn by Bogdan and Knölker (1989) and Bünte and Bogdan (1994).

These new solutions, although highly idealized, could be used in the studies of influence of magnetic field on $p-$ mode oscillation frequencies on the sun. So we have applied our results for the interpretation of umbral oscillations. The observed frequencies by Kenitscher *et al.* (1995) match quite well with our computed frequencies. The assumption of constant τ_R over the entire atmosphere was a oversimplification, but it enabled us to derive an analytic dispersion relation. We hope to extend the scope of our analysis to more realistic atmospheric conditions by including variation of τ_R with height in a future study. Another challenging task could be to determine the influence of magnetoatmospheric waves on spectral line profiles. We expect the waves to produce line shifts and assymetries. These lines which are used as a diagnostic for various heights of the atmosphere could be then used for identification of the wave modes present in those layers.

Appendix A

Displacement of the flux tubes in the two layers

Substituting equations (1.18), (1.19) and (1.51) in equations (1.49), (1.50) and using the dimensionless variables as given in equations (1.36), to (1.41) and (1.52), and also recalling the dispersion relations for different ranges of ω as given in the expressions (1.31) to (1.35), we find after some extensive but straightforward algebra that the displacement of the flux tube in the two layers are given by,

$$\begin{aligned}
\xi_1(s,\tau) = \quad & \frac{L}{\pi}\Bigg[\int_0^r du e^{(s-u^2/4\pi\lambda^2)} \frac{\chi_i \cosh\{(s-\alpha)\chi_i\} - \{r^2\chi_i'+q\}\sinh\{(s-\alpha)\chi_i\}}{\chi_i\cosh(\alpha\chi_i)+(r^2\chi_i'+q)\sinh(\alpha\chi_i)} \frac{\sin(u\tau)}{u} \\
& + \int_r^1 du e^{(s-u^2/4\pi\lambda^2)} \frac{\chi_i q \sinh\{(2\alpha-s)\chi_i\} + \chi_i^2\cosh(\alpha\chi_i)\cosh\{(s-\alpha)\chi_i\}}{\{r^2\chi_r'\sinh(\alpha\chi_i)\}^2+\{\chi_i\cosh(\alpha\chi_i)+q\sinh(\alpha\chi_i)\}^2} \frac{\sin(u\tau)}{u} \\
& - \int_r^1 du e^{(s-u^2/4\pi\lambda^2)} \frac{(r^4\chi_r'^2+q^2)\sinh(\alpha\chi_i)\sinh\{(s-\alpha)\chi_i\}}{\{r^2\chi_r'\sinh(\alpha\chi_i)\}^2+\{\chi_i\cosh(\alpha\chi_i)+q\sinh(\alpha\chi_i)\}^2} \frac{\sin(u\tau)}{u} \\
& - \int_r^1 du e^{(s-u^2/4\pi\lambda^2)} \frac{r^2\chi_i\chi_r'\sinh(s\chi_i)}{\{r^2\chi_r'\sinh(\alpha\chi_i)\}^2+\{\chi_i\cosh(\alpha\chi_i)+q\sinh(\alpha\chi_i)\}^2} \frac{\cos(u\tau)}{u} \\
& + \int_1^\infty du e^{(s-u^2/4\pi\lambda^2)} \frac{\chi_r q \sin\{(2\alpha-s)\chi_r\} + \chi_r^2\cos(\alpha\chi_r)\cos\{(s-\alpha)\chi_r\}}{r^4\chi_r'^2\sin^2(\alpha\chi_r)+\{\chi_r\cos(\alpha\chi_r)+q\sin(\alpha\chi_r)\}^2} \frac{\sin(u\tau)}{u} \\
& - \int_1^\infty du e^{(s-u^2/4\pi\lambda^2)} \frac{(r^4\chi_r'^2+q^2)\sin(\alpha\chi_r)\sin\{(s-\alpha)\chi_r\}}{r^4\chi_r'^2\sin^2(\alpha\chi_r)+\{\chi_r\cos(\alpha\chi_r)+q\sin(\alpha\chi_r)\}^2} \frac{\sin(u\tau)}{u} \\
& - \int_1^\infty du e^{(s-u^2/4\pi\lambda^2)} \frac{r^2\chi_r\chi_r'\sin(s\chi_r)}{r^4\chi_r'^2\sin^2(\alpha\chi_r)+\{\chi_r\cos(\alpha\chi_r)+q\sin(\alpha\chi_r)\}^2} \frac{\cos(u\tau)}{u}\Bigg] \quad , \qquad \text{(A1)}
\end{aligned}$$

$$\begin{aligned}
\xi_2(s,\tau) = \quad & \frac{L}{\pi}\Bigg[\int_0^r du e^{(\alpha+y-y\chi_i'-u^2/4\pi\lambda^2)} \frac{\chi_i}{\chi_i\cosh(\alpha\chi_i)+(r^2\chi_i'+q)\sinh(\alpha\chi_i)} \frac{\sin(u\tau)}{u} \\
& + \int_r^1 du e^{(\alpha+y-u^2/4\pi\lambda^2)} \frac{\chi_i\{\chi_i\cosh(\alpha\chi_i)+q\sinh(\alpha\chi_i)\}}{r^4\chi_r'^2\sinh^2(\alpha\chi_i)+\{\chi_i\cosh(\alpha\chi_i)+q\sinh(\alpha\chi_i)\}^2} \frac{\sin(u\tau-y\chi_r')}{u} \\
& - \int_r^1 du e^{(\alpha+y-u^2/4\pi\lambda^2)} \frac{r^2\chi_i\chi_r'\sinh(\alpha\chi_i)}{r^4\chi_r'^2\sinh^2(\alpha\chi_i)+\{\chi_i\cosh(\alpha\chi_i)+q\sinh(\alpha\chi_i)\}^2} \frac{\cos(u\tau-y\chi_r')}{u} \\
& + \int_1^\infty du e^{(\alpha+y-u^2/4\pi\lambda^2)} \frac{\chi_r\{\chi_r\cos(\alpha\chi_r)+q\sin(\alpha\chi_r)\}}{r^4\chi_r'^2\sin^2(\alpha\chi_r)+\{\chi_r\cos(\alpha\chi_r)+q\sin(\alpha\chi_r)\}^2} \frac{\sin(u\tau-y\chi_r')}{u}
\end{aligned}$$

$$- \int_1^{\infty} du e^{(\alpha+y-u^2/4\pi\lambda^2)} \frac{r^2\chi_r\chi_r' \sin(\alpha\chi_r)}{r^4\chi_r'^2 \sin^2(\alpha\chi_r)+\{\chi_r\cos(\alpha\chi_r)+q\sin(\alpha\chi_r)\}^2} \frac{\cos(u\tau-y\chi_r')}{u} \Bigg] \quad ,(A2)$$

where

$$\chi_i = \sqrt{1-u^2} \quad , \tag{A3}$$

$$\chi_i' = \sqrt{1-u^2/r^2} \quad , \tag{A4}$$

$$\chi_r = \sqrt{u^2-1} \quad , \tag{A5}$$

$$\chi_r' = \sqrt{u^2/r^2-1} \quad , \tag{A6}$$

$$y = r^2(s-\alpha) \quad , \tag{A7}$$

$$q = 1-r^2 \quad . \tag{A8}$$

Kinetic energy Density

To calculate the total kinetic energy density in the whole flux tube, we need to calculate the function $F(\lambda,\alpha,r,\tau)$, which is given by,

$$\begin{aligned}
F(\lambda,\alpha,r,\tau) &= \frac{1}{2\pi^2}\int_0^{\alpha} ds \Bigg[\int_0^{r} du e^{-u^2/4\pi\lambda^2}\cos(u\tau)\frac{\chi_i\cosh\{(s-\alpha)\chi_i\}}{\chi_i\cosh(\alpha\chi_i)+(r^2\chi_i'+q)\sinh(\alpha\chi_i)} \\
&- \int_0^{r} du e^{-u^2/4\pi\lambda^2}\cos(u\tau)\frac{(r^2\chi_i'+q)\sinh\{(s-\alpha)\chi_i\}}{\chi_i\cosh(\alpha\chi_i)+(r^2\chi_i'+q)\sinh(\alpha\chi_i)} \\
&+ \int_r^{1} du e^{-u^2/4\pi\lambda^2}\cos(u\tau)\frac{\chi_i q\sinh\{(2\alpha-s)\chi_i\}-\chi_i^2\cosh(\alpha\chi_i)\cosh\{(s-\alpha)\chi_i\}}{\{\chi_i\cosh\alpha\chi_i+q\sinh\alpha\chi_i\}^2+r^4\chi_r'^2\sinh^2(\alpha\chi_i)} \\
&- \int_r^{1} du e^{-u^2/4\pi\lambda^2}\cos(u\tau)\frac{(r^4\chi_r'^2+q^2)\sinh(\alpha\chi_i)\sinh\{(s-\alpha)\chi_i\}}{\{\chi_i\cosh(\alpha\chi_i)+q\sinh(\alpha\chi_i)\}^2+\{r^2\chi_r'\sinh(\alpha\chi_i)\}^2} \\
&+ \int_r^{1} du e^{-u^2/4\pi\lambda^2}\sin(u\tau)\frac{r^2\chi_i\chi_r'\sinh(s\chi_i)}{\{\chi_i\cosh(\alpha\chi_i)+q\sinh(\alpha\chi_i)\}^2+\{r^2\chi_r'\sinh(\alpha\chi_i)\}^2} \\
&+ \int_1^{\infty} du e^{-u^2/4\pi\lambda^2}\cos(u\tau)\frac{[\chi_r q\sin\{(s-2\alpha)\chi_r\}+\chi_r^2\cos(\alpha\chi_r)\cos\{(s-\alpha)\chi_r\}}{r^4\chi_r'^2\sin^2(\alpha\chi_r)+\{\chi_r\cos(\alpha\chi_r)+q\sin(\alpha\chi_r)\}^2} \\
&- \int_1^{\infty} du e^{-u^2/4\pi\lambda^2}\cos(u\tau)\frac{(r^4\chi_r'^2+q^2)\sin(\alpha\chi_r)\sin\{(s-\alpha)\chi_r\}}{\{\chi_r\cos(\alpha\chi_r)+q\sin(\alpha\chi_r)\}^2+\{r^2\chi_r'\sin(\alpha\chi_r)\}^2} \\
&+ \int_1^{+\infty} du e^{-u^2/4\pi\lambda^2}\sin(u\tau)\frac{r^2\chi_r\chi_r'\sin(s\chi_r)}{r^4\chi_r'^2\sin^2(\alpha\chi_r)+\{\chi_r\cos(\alpha\chi_r)+q\sin(\alpha\chi_r)\}^2}\Bigg]^2
\end{aligned}$$

$$
\begin{aligned}
&+ \frac{1}{2\pi^2}\int_{\alpha}^{\infty} ds \left[\int_{0}^{r} du \frac{e^{(-y\chi_i' - u^2/4\pi\lambda^2)}\chi_i \cos(u\tau)}{\chi_i \cosh(\alpha\chi_i) + (r^2\chi_i' + q)\sinh(\alpha\chi_i)}\right.\\
&+ \int_{r}^{1} du e^{-u^2/4\pi\lambda^2} \frac{\chi_i\{\chi_i \cosh(\alpha\chi_i) + q\sinh(\alpha\chi_i)\}\cos(u\tau - y\chi_r')}{r^4\chi_r'^2 \sinh^2(\alpha\chi_i) + \{\chi_i \cosh(\alpha\chi_i) + q\sinh(\alpha\chi_i)\}^2}\\
&+ \int_{r}^{1} du e^{-u^2/4\pi\lambda^2} \frac{r^2\chi_i\chi_r' \sinh(\alpha\chi_i)\sin(u\tau - y\chi_r')}{r^4\chi_r'^2 \sinh^2(\alpha\chi_i) + \{\chi_i \cosh(\alpha\chi_i) + q\sinh(\alpha\chi_i)\}^2}\\
&+ \int_{1}^{+\infty} du e^{-u^2/4\pi\lambda^2} \frac{\chi_r\{\chi_r \cos(\alpha\chi_r) + q\sin(\alpha\chi_r)\}\cos(u\tau - y\chi_r')}{r^4\chi_r'^2 \sin^2(\alpha\chi_r) + \{\chi_r \cos(\alpha\chi_r) + q\sin(\alpha\chi_r)\}^2}\\
&\left.+ \int_{1}^{\infty} du e^{-u^2/4\pi\lambda^2} \frac{r^2\chi_r\chi_r' \sin(\alpha\chi_r)\sin(u\tau - y\chi_r')}{r^4\chi_r'^2 \sin^2(\alpha\chi_r) + \{\chi_r \cos(\alpha\chi_r) + q\sin(\alpha\chi_r)\}^2}\right]^2 . \qquad \text{(A9)}
\end{aligned}
$$

Appendix B

Solution of equation (2.23)

Here we present the asymptotic properties of the solution of the wave equations in a uniform vertical magnetic field. It was shown by Zhugzhda and Dzhalilov (1982; ZD) that the general solution to equation (2.23) can be expressed in terms of Meijer functions as follows

$$\xi_x^{(h)} = G^{12}_{2,4}\left(\mu_h, \begin{matrix} a_1 & , & a_2 \\ \mu_1, \ \cdots, & \mu_i, & \cdots, \ \mu_4 \end{matrix} \Big| \theta^2\right) \qquad (i,h = 1,\ldots,4;\ i \neq h)\,, \quad \text{(B1)}$$

where

$$\mu_{1,2} = \frac{(1 \pm \mathrm{i}\alpha)}{2}, \qquad \mu_{3,4} = \pm K\,, \quad \text{(B2)}$$

$$a_{1,2} = \frac{(1 \pm \phi)}{2}\,, \quad \text{(B3)}$$

$$\alpha = \sqrt{4\Omega^2 - 1}\,, \quad \text{(B4)}$$

$$\phi = \sqrt{-\alpha^2 + 4K^2(1 - \Omega_{\rm BV}^2/\Omega^2)}\,, \quad \text{(B5)}$$

and $\Omega_{\rm BV}^2 = (\gamma - 1)/\gamma^2$ is the Brunt-Väisälä frequency (in dimensionless units).

Once $\xi_x^{(h)}$ is known, it is fairly straightforward to determine the corresponding solutions $\xi_z^{(h)}$ from either of equations (2.16) or (2.17). The complete solutions satisfying the required boundary conditions can be built up as linear combinations of $\xi_x^{(h)}$ and $\xi_z^{(h)}$.

Weak-Field Solution

We now focus our attention on the limit of a weak field, for which $c_S/v_A \gg 1$ and $\theta \gg 1$. This corresponds to the limit of small ϵ, with

$$\epsilon \equiv \frac{v_{A,0}}{c_S}\,. \quad \text{(B6)}$$

However, in addition we must require that the vertical extension d of the layer is not too large (*cf.* eq. [2.22]) (for $d > 0$). Since the density increases for negative z, the above restriction, of course, does not apply if d lies below the plane $z = 0$.

When $\theta \gg 1$, the Meijer function in equation (B1) has the following asymptotic expansion (ZD):

$$G^{12}_{2,4}(\mu_h|\theta^2) = \frac{1}{2\sqrt{\pi\theta}}\left[e^{i(2\theta-\delta_h)}(1+i\frac{M}{\theta}-\frac{M_1}{\theta^2})+e^{-i(2\theta-\delta_h)}(1-i\frac{M}{\theta}-\frac{M_1}{\theta^2})\right]$$
$$+ \frac{1}{\theta}[S_h(1+\frac{L_1^+}{\theta^2})\theta^{2iK_z}+T_h(1+\frac{L_1^-}{\theta^2})\theta^{-2iK_z}]+O(\frac{1}{\theta^3}), \tag{B7}$$

$$K_z^2 = \Omega^2 - K^2(1-\frac{\Omega_{BV}^2}{\Omega^2})-\frac{1}{4}=\frac{\phi}{2i}, \tag{B8}$$

$$\delta_h = \pi(1/4+\mu_h), \tag{B9}$$

$$M = K^2\frac{\Omega_{BV}^2}{\Omega^2}-\frac{1}{16}, \tag{B10}$$

$$M_1 = \frac{K^2}{2}-\frac{1}{32}+\frac{M}{4}(2M-3), \tag{B11}$$

$$L_1^{\pm} = -\frac{[w_\pm(w_\pm+1)+\Omega^2](w_\pm^2-K^2)}{2w_\pm}, \tag{B12}$$

$$w_\pm = \frac{1}{2}\mp iK_z = a_{2,1}, \tag{B13}$$

$$S_h = \frac{\Gamma(\phi)\,\Gamma(1+\mu_h-a_1)}{\prod_{j=1,j\neq h}^4\Gamma(a_1-\mu_j)}, \tag{B14}$$

$$T_h = \frac{\Gamma(-\phi)\,\Gamma(1+\mu_h-a_2)}{\prod_{j=1,j\neq h}^4\Gamma(a_2-\mu_j)}. \tag{B15}$$

It should be borne in mind that the expansion for the Meijer function given by equation (B7) is valid as long as $M/\theta \ll 1$, which restricts K to values such that $K^2 \ll \Omega^3\, v_A/c_s$. Thus, for $K \sim 1$, we have the condition $v_A/c_s \ll \Omega^3$, which places a more severe restriction on the permitted field strengths than the condition $\theta \gg 1$.

Using the expansion given by equation (B7), we find that $\xi_x^{(h)}$ can be expressed in a compact form as follows

$$\xi_x^{(h)} = \frac{1}{\theta}\sum_{j=1}^{2}C_j^{(h)}f_j(\theta)+\frac{1}{\sqrt{\theta}}\sum_{j=3}^{4}C_j^{(h)}f_j(\theta), \tag{B16}$$

where

$$C_1^{(h)} = T_h+S_h, \quad C_2^{(h)} = T_h - iS_h, \tag{B17}$$

$$C_3^{(h)} = \frac{1}{\sqrt{\pi}} \sin\delta_h, \quad C_4^{(h)} = \frac{1}{\sqrt{\pi}} \cos\delta_h. \tag{B18}$$

The function f_j are

$$f_1 = (q_1 + \frac{q_1'}{\theta^2})\cos K_x Z - (q_2 + \frac{q_2'}{\theta^2})\sin K_x Z + O(\frac{1}{\theta^3}), \tag{B19}$$

$$f_2 = (q_1 + \frac{q_1'}{\theta^2})\sin K_x Z + (q_2 + \frac{q_2'}{\theta^2})\cos K_x Z + O(\frac{1}{\theta^3}), \tag{B20}$$

$$f_3 = \left(1 - \frac{M_1}{\theta^2}\right)\cos 2\theta - \frac{M}{\theta}\sin 2\theta + O(\frac{1}{\theta^3}), \tag{B21}$$

$$f_4 = \left(1 - \frac{M_1}{\theta^2}\right)\sin 2\theta + \frac{M}{\theta}\cos 2\theta + O(\frac{1}{\theta^3}), \tag{B22}$$

where $Z = z/H$ and

$$q_1 = \frac{1}{2}\left[\left(\frac{\Omega}{\epsilon}\right)^{-2iK_x} + \left(\frac{\Omega}{\epsilon}\right)^{2iK_x}\right], \tag{B23}$$

$$q_2 = \frac{1}{2i}\left[\left(\frac{\Omega}{\epsilon}\right)^{-2iK_x} - \left(\frac{\Omega}{\epsilon}\right)^{2iK_x}\right], \tag{B24}$$

$$q_1' = \frac{1}{2}\left[L_1^- \left(\frac{\Omega}{\epsilon}\right)^{-2iK_x} + L_1^+ \left(\frac{\Omega}{\epsilon}\right)^{2iK_x}\right], \tag{B25}$$

$$q_2' = \frac{1}{2i}\left[L_1^- \left(\frac{\Omega}{\epsilon}\right)^{-2iK_x} - L_1^+ \left(\frac{\Omega}{\epsilon}\right)^{2iK_x}\right]. \tag{B26}$$

It follows that to this asymptotic order the general solution ξ_x, which is a linear combination of the $\xi_x^{(h)}$, may equally well be expressed as a linear combination of the functions f_j $(j = 1, \ldots, 4)$. Physically, $f_{1,2}$ and $f_{3,4}$ correspond to the non-magnetic and magnetic contributions to the solution, respectively. In order to calculate $\xi_x^{(h)}$, we assume a series expansion in ascending powers of $1/\theta$, similar to $\xi_x^{(h)}$ but with different coefficients. It turns out that $\xi_x^{(h)}$ can be expressed as

$$i\xi_x^{(h)} = \frac{1}{\theta}\sum_{j=1}^{2} C_j^{(h)} g_j(\theta) + \frac{1}{\theta^{3/2}}\sum_{j=3}^{4} C_j^{(h)} g_j(\theta), \tag{B27}$$

The coefficients $g_{3,4}$ and $g_{1,2}$ in equation (B27) are the corresponding magnetic and non-magnetic contributions to ξ_x respectively. These can be determined from equations (2.16) and (2.17) respectively, rewritten as

$$[4(\Omega^2 - K^2)\theta^2 - 4\Omega^2K^2 + \Omega^2\theta\frac{d}{d\theta} + \Omega^2\theta^2\frac{d^2}{d\theta^2}]\xi_x = -4iK\theta^2(\frac{1}{\gamma} + \frac{\theta}{2}\frac{d}{d\theta})\xi_x, \tag{B28}$$

$$[\Omega^2 + \frac{3}{4}\theta\frac{d}{d\theta} + \frac{\theta^2}{4}\frac{d^2}{d\theta^2}]\xi_x = -iK(\frac{\gamma - 1}{\gamma} + \frac{\theta}{2}\frac{d}{d\theta})\xi_x. \tag{B29}$$

The functions g_j, $(g_j = 1, \ldots, 4)$ are

$$g_1 = (p_1 + \frac{p_1'}{\theta^2}) \cos K_x Z - (p_2 + \frac{p_2'}{\theta^2}) \sin K_x Z + O(\frac{1}{\theta^3}), \tag{B30}$$

$$g_2 = (p_1 + \frac{p_1'}{\theta^2}) \sin K_x Z + (p_2 + \frac{p_2'}{\theta^2}) \cos K_x Z + O(\frac{1}{\theta^3}), \tag{B31}$$

$$g_3 = K(\sin 2\theta + \frac{N}{\theta} \cos 2\theta) + O(\frac{1}{\theta^2}), \tag{B32}$$

$$g_4 = K(-\cos 2\theta + \frac{N}{\theta} \sin 2\theta) + O(\frac{1}{\theta^2}) \,. \tag{B33}$$

Here

$$p_1 = \frac{K}{2} \left[Q_0^- \left(\frac{\Omega}{\epsilon}\right)^{-2iK_x} + Q_0^+ \left(\frac{\Omega}{\epsilon}\right)^{2iK_x} \right], \tag{B34}$$

$$p_2 = \frac{K}{2i} \left[Q_0^- \left(\frac{\Omega}{\epsilon}\right)^{-2iK_x} - Q_0^+ \left(\frac{\Omega}{\epsilon}\right)^{2iK_x} \right], \tag{B35}$$

$$p_1' = \frac{K}{2} \left[Q_1^- \left(\frac{\Omega}{\epsilon}\right)^{-2iK_x} + Q_1^+ \left(\frac{\Omega}{\epsilon}\right)^{2iK_x} \right], \tag{B36}$$

$$p_2' = \frac{K}{2i} \left[Q_1^+ \left(\frac{\Omega}{\epsilon}\right)^{-2iK_x} - Q_1^- \left(\frac{\Omega}{\epsilon}\right)^{2iK_x} \right], \tag{B37}$$

where

$$N = M + \frac{1}{\gamma} + \frac{1}{4} - \frac{\Omega^2}{K^2}, \tag{B38}$$

$$Q_0^{\pm} = -\frac{i}{r} t_{\pm}, \tag{B39}$$

$$t_{\pm} = \pm K_x + i(\frac{1}{\gamma} - \frac{1}{2}), \tag{B40}$$

$$Q_1^{\pm} = \frac{(w_{\pm} + 1/\gamma)(w_{\pm}^2 - K^2)}{2w_{\pm}}, \tag{B41}$$

$$r = K^2(1 - \frac{\Omega_{BV}^2}{\Omega^2}). \tag{B42}$$

$$u_{\pm} = \frac{1}{2}(t_- Q_1^+ \pm t_+ Q_1^-). \tag{B43}$$

It follows that the gradients can be expressed as

$$\frac{d\xi_x^{(h)}}{dz} = \frac{1}{\theta} \sum_{j=1}^{2} C_j^{(h)} \left[\frac{f_j(\theta)}{2H} + \frac{df_j(\theta)}{dz} \right] + \frac{1}{\sqrt{\theta}} \sum_{j=3}^{4} C_j^{(h)} \left[\frac{f_j(\theta)}{4H} + \frac{df_j(\theta)}{dz} \right], \tag{B44}$$

$$i\frac{d\xi_x^{(h)}}{dz} = \frac{1}{\theta} \sum_{j=1}^{2} C_j^{(h)} \left[\frac{g_j(\theta)}{2H} + \frac{dg_j(\theta)}{dz} \right] + \frac{1}{\theta^{3/2}} \sum_{j=3}^{4} C_j^{(h)} \left[\frac{3g_j(\theta)}{4H} + \frac{dg_j(\theta)}{dz} \right]. \tag{B45}$$

To derive the dispersion relation we now apply the boundary conditions given by equations (2.29) to equations (B44) and (B45). We get a set of four equations which can be written as

$$AX = 0\,, \tag{B46}$$

where

$$X^T = (C_1 \quad C_2 \quad C_3 \quad C_4)\,, \tag{B47}$$

and

$$A = \begin{pmatrix} \dfrac{f_1}{2H} + \dfrac{\mathrm{d}f_1}{\mathrm{d}z}\Big|_0 & \dfrac{f_2}{2H} + \dfrac{\mathrm{d}f_2}{\mathrm{d}z}\Big|_0 & \dfrac{f_3}{4H} + \dfrac{\mathrm{d}f_3}{\mathrm{d}z}\Big|_0 & \dfrac{f_4}{4H} + \dfrac{\mathrm{d}f_4}{\mathrm{d}z}\Big|_0 \\ \theta_0 & \theta_0 & \theta_0 & \theta_0 \\ \dfrac{f_1}{2H} + \dfrac{\mathrm{d}f_1}{\mathrm{d}z}\Big|_D & \dfrac{f_2}{2H} + \dfrac{\mathrm{d}f_2}{\mathrm{d}z}\Big|_D & \dfrac{f_3}{4H} + \dfrac{\mathrm{d}f_3}{\mathrm{d}z}\Big|_D & \dfrac{f_4}{4H} + \dfrac{\mathrm{d}f_4}{\mathrm{d}z}\Big|_D \\ \theta_D & \theta_D & \theta_D & \theta_D \\ \dfrac{g_1}{2H} + \dfrac{\mathrm{d}g_1}{\mathrm{d}z}\Big|_0 & \dfrac{g_2}{2H} + \dfrac{\mathrm{d}g_2}{\mathrm{d}z}\Big|_0 & \dfrac{3g_3}{4H} + \dfrac{\mathrm{d}g_3}{\mathrm{d}z}\Big|_0 & \dfrac{3g_4}{4H} + \dfrac{\mathrm{d}g_4}{\mathrm{d}z}\Big|_0 \\ \theta_0 & \theta_0 & \theta_0 & \theta_0 \\ \dfrac{g_1}{2H} + \dfrac{\mathrm{d}g_1}{\mathrm{d}z}\Big|_D & \dfrac{g_2}{2H} + \dfrac{\mathrm{d}g_2}{\mathrm{d}z}\Big|_D & \dfrac{3g_3}{4H} + \dfrac{\mathrm{d}g_3}{\mathrm{d}z}\Big|_D & \dfrac{3g_4}{4H} + \dfrac{\mathrm{d}g_4}{\mathrm{d}z}\Big|_D \\ \theta_D & \theta_D & \theta_D & \theta_D \end{pmatrix}. \tag{B48}$$

Here $\theta_0 = \theta(0)$ and $\theta_D = \theta(D)$. The condition for equation (B46) to have a non-trivial solution is

$$\det[A] = 0\,. \tag{B49}$$

Expanding equation (B49) and substituting for f_j and g_j $(j = 1, \ldots, 4)$ we obtain

$$\begin{aligned}
&(\tfrac{1}{4} + K_x^2)(\Omega^2 - K^2)\sin\tilde{\theta}\sin(K_x D) = \\
&= 2\tfrac{\epsilon}{\Omega}\mathrm{e}^{D/4}(\tfrac{1}{4} + K_x^2)\Big\{K_x K^3[\cosh(D/4)\cos\tilde{\theta}\cos(K_x D) - \cosh(D/2)] \\
&+ \sinh(D/4)\cos\tilde{\theta}\sin(K_x D)[(M + \tfrac{1}{4})(\Omega^2 - K^2) - K^3(\tfrac{1}{\gamma} - \tfrac{1}{2})]\Big\} \\
&+ \tfrac{\epsilon^2}{\Omega^2}\mathrm{e}^{D/2}\sin\tilde{\theta}(\tfrac{1}{4} + K_x^2)\Big\{[M(M+2)(K^2 - \Omega^2) + 2MK^3(\tfrac{1}{\gamma} - \tfrac{1}{2}) - rK^4]\sin(K_x D) \\
&+ 2K^2(u_- + (NK + \tfrac{3}{4})K_x)\sinh(D/2)\,\cos(K_x D) + 2[(M_1 + \tfrac{3}{4})(\Omega^2 - K^2) \\
&+ K^2\{\tfrac{u_+}{i} + (\tfrac{1}{\gamma} - \tfrac{1}{2})(\tfrac{3}{4} + KN)\}]\cosh(D/2)\,\sin(K_x D)\Big\} + O(\tfrac{\epsilon^3}{\Omega^3})\,.
\end{aligned} \tag{B50}$$

which is the dispersion relation accurate to second order in ϵ. Here $\tilde{\theta} = \theta_D - \theta_0$, and M, M_1, N, r, K_z and $u_\pm$ are defined in equations (B10), (B11), (B38), (B42), (B8), (B43) respectively.

Bibliography

[] Abdelatif, T. E. 1986, *Astrophys. J.*, **311**, 1015.

[] Abdelatif, T. E. 1990, *Solar Phys.*, **129**, 201.

[] Alisandrakis, C. E., Georgakilas, A. A. and Dialetis, D. 1992, *Solar Phys.*, **138**, 93.

[] Alfvén, H. 1950, in *Cosmical Electrodynamics*, (Oxford University Press:London).

[] Berger, T. E. and Title, A. M. 1996, *Astrophys. J.*, **463**, 49.

[] Beckers, J. M. and Schulz, R.B. 1972, *Solar Phys.*, **27**, 61.

[] Bhatnagar, A., Livingston, W. C. and Harvey, J. W. 1972, *Solar Phys.*, **27**, 80.

[] Bogdan, T. J. and Zweibel, E. G. 1985, *Astrophys. J.*, **298**, 867.

[] Bogdan, T. J. and Cattaneo, F. 1989, *Astrophys. J.*, **342**, 545.

[] Bogdan, T. J. and Knölker, M. 1989, *Astrophys. J.*, **339**, 579.

[] Bray, R. J. and Loughhead, R. E. 1974, in *The Solar Chromosphere*, (Chapman & Hall: London).

[] Bünte, M. and Bogdan, T. J. 1994, *Astron. Astrophys.* **283**, 642.

[] Cairns, R. A. and Lashmore-Davies, C. N. 1983, *Phys. Fluids*, **23**, 1268.

[] Cally, P. S. and Bogdan, T. J. 1993, *Astrophys. J.*, **402**, 721.

[] Cally, P. S., Bogdan, T. J. and Zweibel, E. G. 1994, *Astrophys. J.*, **437**, 505.

[] Cash, J. R. Moore, D. R. 1980. *BIT*, **20**, 44.

[] Cattaneo, F., Brummell, N. H., Toomre, J., Malagoli, A., and Hulbnet, N. E. 1991, *Astrophys. J.*, **370**, 282.

[] Choudhuri, A. R., Auffret, H., and Priest, E. R. 1993, *Solar Phys.*, **143**, 49 (CAP).

[] Christensen-Dalsgaard, J. 1981. *Mon. Not. R. astr. Soc.*, **194**, 229.

[] Cowling, T. G. 1957, in *Magnetohydrodynamics*, (Interscience Publishers:New York).

[] Craik, A. D. D. 1988, in *Wave interactions and fluid flows*, (Cambridge University Press).

[] Defouw, R. J. 1976, *Astrophys. J.*, **209**, 266.

[] Deubner, F. L. 1967, *Solar Phys.*, **2**, 133.

[] Deubner, F. L., Waldschik, Th. and Steffens, S. 1996, *Astron. Astrophys.*, **307**, 936.

[] Dzhalilov, N. S. and Staude, J. 1995, *Astron. Astrophys.*, **303**, 561.

[] Ferraro, V. C. and Plumpton, C. 1958, *Astrophys. J.*, **127**, 459.

[] Fontenla, J. M., Avrett, E. H., and Loeser, R. 1990, *Astrophys. J.*, **355**, 700.

[] Friedrich, H. and Wintgen, D. 1989, *Phys. Rep* **183**, 37.

[] Giovanelli, R. G. 1975, *Solar Phys.*, **44**, 289.

[] Giovanelli, R. G., Harvey, J. W. and Livingston, W. C. 1978, *Solar Phys.*, **59**, 40.

[] Gurman, J. B. and Leibacher, J. W. 1984, *Astrophys. J.*, **283**, 859.

[] Gurman, J. B. 1987, *Solar Phys.*, **108**, 61.

[] Hasan, S. S. and Abdelatif, T., 1990, in *Physics of Magnetic Flux Ropes*, eds. C. T. Russell, E. R. Priest and L. C. Lee, (AGU Monograph), p. 93.

[] Hasan, S. S. 1991, *Astrophys. J.*, **366**, 328.

[] Hasan, S. S. and Christensen-Dalsgaard, J. 1992, *Astrophys. J.*, **396**, 311 (HC).

[] Hollweg, J. V. 1981, *Solar Phys.*, **70**, 25.

[] Hollweg, J. V. 1982, *Astrophys. J.*, **257**, 345.

[] Hollweg, J. V. 1984, *Astrophys. J.*, **277**, 392.

[] Hollweg, J. V. 1990a, *Computer Phys.Rep.*, **122**, 205.

[] Hollweg, J. V. 1990b, in *Physics of Magnetic Flux Ropes*, eds. C.T. Russell, E. R. Priest and L. C. Lee, (AGU Monograph), p. 23.

[] Huang, P., Musielak. Z. E., and Ulmscneider, P. *Astron. Astrophys.*, **297**, 579.

[] Keller, C. U., Deubner, F. L., Egger, U., Fleck, B., and Povel, M. P. 1994, *Astron. Astrophys.* **286**, 626.

[] Kenitscher, T. J and Mattig, W. 1995, *Astron. Astrophys.*, **300**, 539.

[] Lamb, H. 1932, in *Hydrodynamics*, Cambridge University Press, Cambridge

[] Lee, U. and Saio, H. 1990, *Astrophys. J.*, **360**, 590.

[] Leibacher, J. W. and Stein, R. F. 1981 in *The Sun as a star*, (NASA), 263.

[] Leighton, R. B., Noyes, R. W. and Simon, G. W. 1962, *Astrophys. J.*, **135**, 474

[] Lites, B. W. 1984, *Astrophys. J.*, **277**, 874.

[] Lites, B. W. and Thomas, J. H. 1985, *Astrophys. J.*, **294**, 682.

[] Lites, B. W. 1992, in *Sunspots: Theory and observations*, eds. J. H. Thomas and N. O. Weiss (Dordrecht:kluwer),261.

[] McLellan, A. and Winterberg, F. 1968, *Solar Phys.*, **4**, 401.

[] Mihalas, D. and Mihalas, B. W. 1984, in *Foundations of Radiation Hydrodynamics*, (Oxford University Press, New York).

[] Moore, R. L. and Rabin, D. 1985, *Ann. Rev. Astron. Astrophys.*, **23**, 239.

[] Moreno-Insertis, F. and Spruit, H. 1989, *Astrophys. J.*, **342**, 1158.

[] Muller, R., Vigneau, J., Roudier, T., and Auffret, H. 1994, *Astron. Astrophys.*, **283**, 232.

[] Nagakawa, Y., Priest, E. R. and Wellck, R. E. 1973, *Astrophys. J.*, **184**, 931.

[] Narain, U., and Ulmschneider, P. 1991, *Space Sci. Rev.*, **54**, 377.

[] Narain, U., and Ulmschneider, P. 1996, *Space Sci. Rev.*, **75**, 453.

[] Norduland, A., and Dravins, D. 1990, *Astron. Astrophys.*, **238**, 155.

[] Noyes, R. W., and Leighton, R. B. 1963, *Astrophys. J.*, **138**, 631.

[] Parker, E. N. 1986, in *Coronal and Prominence Plasmas*, ed. A. I. Poland, (NASA Conf.Publ. **2442**), 9.

[] Priest, E. R. 1982, in *Solar Magnetohydrodynamics*, D. Reidel, Dordrecht

[] Rae, I. C., and Roberts, B. 1982, *Astrophys. J.*, **256**, 761.

[] Roberts, B. 1985, in *Solar System Magnetic Fields*, ed. E. R. Priest (Dordrecht: D.Reidel), 37.

[] Roberts, B. 1990, in *Physics of Magnetic Flux Ropes*, eds. C.T. Russell, E.R. Priest and L.C. Lee, (AGU Monograph), p. 113.

[] Schatzman, E. and Souffrin, P. 1967,*Ann. Rev.Astron. Astrophys.* , **5**, 67.

[] Scheuer, M.D. and Thomas, J.H. 1981, *Solar Phys.*, **71**, 21.

[] Souffrin, P. 1972, *Astron. Astrophys.*, **17**, 458.

[] Spiegel, E. A. 1957, *Astrophys. J.* **126**, 202.

[] Spruit, H. C. 1981, *Astron. Astrophys.*, **98**, 155.

[] Spruit, H. C. 1982, *Solar Phys.*, **75**, 3.

[] Spruit, H. C. 1984, in *Small Scale Dynamical Processes in Quiet Stellar Atmosphere*, ed. S. L. Keil (National Solar Observatory, Sunspot N. M.), 249

[] Spruit, H. C. and Bogdan, T. J. 1992, *Astrophys. J. Letters*, **391L**, 109

[] Steffen, M., Freytag, B., and Holweger, H. 1994, in *Solar magnetic fields.* eds. M. Schussler & W. Schmidth (Cambridge University press), 298.

[] Stenflo, J. O. 1989, *Astron. Astrophys. Rev.*, **1**, 3.

[] Stix, M. 1970, *Astron. Astrophys.*, **4**, 189.

[] Sutmann, G. and Ulmscneider, P. 1995, *Astron. Astrophys.*, **294**, 232.

[] Thomas, J. H. 1982, *Astrophys. J.*, **262**, 760.

[] Thomas, J. H. and Scheuer, M. A. 1982, *Solar Phys.*, **79**, 19.

[] Thomas, J. H., Cram, L. E. and Nye, A. H. 1984, *Astrophys. J.*, **285**, 368.

[] Thomas, J. H., Lites, B. W., Gurman, J. B. and Ladd, E. F. 1987, *Astrophys. J.*, **312**, 457.

[] Thomas, J. H. 1990, in *Physics of Magnetic Flux Ropes*, eds. C. T.Russell, E. R. Priest and L.C. Lee, (AGU Monograph), p. 133.

[] Thomas, J. H. and Weiss, N. O. 1992, in Sunspots: Theory and observations, eds. J. H. Thomas and N. O. Weiss (Dordrecht:kluwer),3.

[] Uchida, Y. and Sakurai, T. 1975, *PASJ*, **27**, 259.

[] Ulmschneider, P. , Priest, E. R., and Rosner, R. 1991, in *Mechanisms of Chromospheric and Coronal Heating*, Springer-verlag, Berlin

[] Ulmschneider, P., Zähringer, K., and Musielak, Z. E. 1991, *Astron. Astrophys.*, **241**, 625.

[] Vernazza, J. E., Avrett, E. H., and Loeser, R. 1981, *Astrophys. J. Suppl.*, **45**, 635.

[] Wood, W. P. 1990, *Mon. Not. R. astr. Soc.*, **251**, 427.

[] Worral, G. 1991, *Solar Phys.*, **128**, 353.

[] Zhugzhda, Yu. D. 1979, *Soviet Astron.*, **23**, 42.

[] Zhugzhda, Yu. D. and Dzhalilov, N. S. 1982, *Astron. Astrophys.*, **112**, 16.

[] Zhugzhda, Yu. D. and Locans, V. 1982, *Solar Phys.*, **76**, 77.

[] Zhugzhda, Yu. D., Locans, V. and Staude, J. 1983, *Solar Phys.*, **82**, 369.

[] Zhugzhda, Yu. D., Staude, J. and Locans, V. 1984, *Solar Phys.*, **91**, 219.

[] Zhugzhda, Yu. D. and Dzhalilov, N. S. 1984a, *Astron. Astrophys.*, **132**, 45.

[] Zhugzhda, Yu. D. and Dzhalilov, N. S. 1984b, *Astron. Astrophys.*, **132**, 52.

[] Zirin, H. 1987, *Solar Phys.* **110**, 101.

[] Zirker, J. B. 1964, *Ann. Astrophys.* **27**, 429.

[] Zweibel, E. G. and Bogdan, T. J. 1986, *Astrophys. J.*, **308**, 401.

List of Publications

Refereed Journals

1) **Banerjee, D.**, Hasan, S. S. and Dalsgaard, J. C. *Effect of Newtonian cooling on waves in a magnetized isothermal atmosphere Solar Phy.*, 1997, **(in press)**

2) **Banerjee, D.**, Hasan, S. S. and Dalsgaard, J. C. *The influence of vertical magnetic field on oscillations in an stratified solar atmosphere. ApJ*, 1995, **451**, 825-842.

3) Choudhuri, A. R.,Dikpati, M. and **Banerjee, D.** *Energy transport to the Solar corona by magnetic kink waves. ApJ*, 1993, **413**, 811-825.

Proceedings

1) **Banerjee, D.**, Hasan, S. S. and Dalsgaard, J. C. *The influence of magnetic field on oscillations in an isothermal radiative atmosphere.* In: *Proc. SCORE'96 workshop: Convection,* eds J. C. Dalsgaard & F. P. Pijpers., Kluwer, (in press).

2) **Banerjee, D.**, Hasan, S. S. and Dalsgaard, J. C. *Wave leakage in a magnetized isothermal atmosphere.* In: Proc. of the international conference on "Windows on the Sun's Interior". Bull. Astro. Soc. India. 1996, **24**, 325

In Preparation

1) **Banerjee, D.**, Hasan, S. S. and Dalsgaard, J. C. *On the propagation of magnetoatmospheric waves in a radiating magnetized atmosphere.*

2) **Banerjee, D.**, Hasan, S. S. and Dalsgaard, J. C. *Wave leakage in a magnetized isothermal atmosphere II.*